UNIVERSITY OF CALIFORNIA,
IRVINE

Laser Speckle Imaging of Blood Flow Beneath Static Scattering Media

DISSERTATION

submitted in partial satisfaction of the requirements
for the degree of

DOCTOR OF PHILOSOPHY

in Biomedical Engineering

by

Caitlin Anderson Regan

Dissertation Committee:
Associate Professor Bernard Choi, Chair
Associate Professor Elliot Botvinick
Professor Vasan Venugopalan

2017

DEDICATION

To John, for inspiring my passion for science.

TABLE OF CONTENTS

LIST OF FIGURES

LIST OF TABLES

ACKNOWLEDGMENTS

I would like to thank my family, especially my parents John and Marla, and my sister Anik, for their love, encouragement, and support throughout the years. I would also like to thank my friends for keeping me sane, in particular Eva, who has put up with me forever and constantly inspires me to do better.

I will always be grateful for my advisor, Dr Bernard Choi, who took a chance on me. Bernard is the most positive, supportive mentor I could imagine. He allowed me both the freedom to pursue my research ideas independently, while providing invaluable guidance and support. Bernard's excitement and dedication to both his research and students is inspiring.

To my first mentor in the optics and biophotonics field, Dr Julio Ramierz-San-Juan: muchas gracias por todo que me han enseñado. Julio took me under his wing during my first few months in the lab and provided me a solid foundation in speckle theory and practice that guided all of my future work.

The research I have done would not have been possible without the Virtual Photonics Initiative, and in particular Dr Carole Hayakawa. Thank you Carole for your clear explanations of complicated programming concepts and your dedication to growing the software to incorporate any modification I could dream up.

Finally, I would like to thank all of my colleagues at the Beckman Laser Institute and the MTI Lab for creating a wonderful work environment. In particular, thank you to Christian, for challenging me to think through my ideas and to Sean and Bruce for knowing everything.

I also thank the Society of Photo Optical Instrumentation Engineers, John Wiley & Sons Inc, and the Optical Society of America for permission to include portions of Chapters 1, 2, and 3 of my dissertation, which were originally published in The Journal of Biomedical Optics, Lasers in Surgery and Medicine, and Optics Letters. Financial support was provided by the University of California, Irvine, a NSF BEST IGERT Traineeship (DGE-1144901), a student research grant from the American Society for Lasers in Medicine and Surgery, a fellowship from the ARCS/Roche Foundation, the NIH Laser Microbeam and Medical Program (P41 EB015890), the Arnold and Mabel Beckman Foundation, and CONACYT (CB-2010-156876-F).

CURRICULUM VITAE

Caitlin Anderson Regan

2012 B.S. in Bioengineering (Mechanics), California Institute of Technology

2014 M.S. in Biomedical Engineering, University of California, Irvine

2017 Ph.D. in Biomedical Engineering, University of California, Irvine

PUBLICATIONS

C. Regan, C.K. Hayakawa, B. Choi, "Momentum Transfer Monte Carlo for the Simulation of Laser Speckle Contrast Imaging and its Application in the Skin" *in preparation*, (2017).

C. Regan, S.M. White, B.Y. Yang, T. Takesh, J. Ho, C. Wink, P. Wilder-Smith, B. Choi, "Design and Evaluation of a Miniature Laser Speckle Imaging Device to Assess Gingival Health," Journal of Biomedical Optics, Vol. 21, No. 10, art. 104002 (2016).

C. Regan, B. Choi, "Laser Speckle Imaging Based on Photothermal Convection," Journal of Biomedical Optics, Vol. 21, No. 2, art. 026011 (2016).

C. Regan, B.Y. Yang, K.C. Mayzel, J.C. Ramirez-San-Juan, P. Wilder-Smith, B. Choi, "Fiber-based laser speckle imaging for the detection of pulsatile flow," Lasers in Surgery and Medicine, Vol. 47, No. 6, pp. 520-525 (2015).

J.C. Ramirez-San-Juan, C. Regan, B. Coyotl-Ocelotl, B. Choi, "Spatial versus temporal laser speckle contrast analyses in the presence of static optical scatterers," Journal of Biomedical Optics, Vol. 19, No. 10, art. 106009 (2014).

C. Regan, J.C. Ramirez-San-Juan, B. Choi, "Photothermal Laser Speckle Imaging," Optics Letters, Vol. 39, No. 17, pp. 5006-5009 (2014).

PATENTS

C. Regan, S.M. White, B.Y. Yang, P. Wilder-Smith, B. Choi, "Methods and apparatus for the assessment of gingival blood flow," Provisional Patent No: 62/345,653.

CONFERENCE PRESENTATIONS

C. Regan, S.M. White, B.Y. Yang, T. Takesh, J. Ho, C. Wink, P. Wilder-Smith, B. Choi, **"**Design and Evaluation of a Miniature Laser Speckle Imaging Device to Assess Gingival Health," SPIE Photonics West, oral presentation. San Francisco, California (January 2017).

C. Regan, C.K. Hayakawa, B. Choi, "Modeling Laser Speckle Imaging of Perfusion in the Skin," BMES Annual Meeting, oral presentation. Minneapolis, Minnesota (October 2016).

C. Regan, C.K. Hayakawa, B. Choi, "Momentum Transfer Monte Carlo to Simulate Laser Speckle Contrast," Gordon Research Conference: Lasers in Medicine and Biology, poster presentation. Mt. Snow, Vermont (July 2016).

C. Regan, C.K. Hayakawa, B. Choi, "Modeling Laser Speckle Imaging of Perfusion in the Skin," SPIE Photonics West, oral presentation. San Francisco, California (February 2016).

C. Regan, C.K. Hayakawa, B. Choi, "Momentum Transfer Monte Carlo for the Simulation of Laser Speckle Contrast Imaging," SPIE Photonics West, oral presentation. San Francisco, California (February 2016).

C. Regan, "Recent Advances in Laser Speckle Imaging," Busan National University, invited talk. Busan, South Korea (August 2015).

C. Regan, "Biomedical Applications of Laser Speckle Imaging," Dankook University, invited talk. Cheonan, South Korea (July 2015).

C. Regan, J.C. Ramirez-San-Juan, B. Choi, "Photothermal Laser Speckle Imaging," Engineering Conference International, poster presentation. Vail, Colorado (June 2015).

C. Regan, J.C. Ramirez-San-Juan, B. Choi, "Photothermal Laser Speckle Imaging," 7th International Graduate Summer School: Biophotonics, poster presentation. Ven, Sweden (June 2015).

C. Regan, S.M. White, B.Y. Yang, P. Wilder-Smith, B. Choi, "Measurement of Pulsatile Flow in the Teeth Using Laser Speckle Imaging," ASLMS Annual Conference, oral presentation. Kissimmee, Florida (April 2015).

C. Regan, J.C. Ramirez-San-Juan, B. Choi, "Photothermal Laser Speckle Imaging," Beckman Laser Institute Korea Symposium, oral presentation. Irvine, California (February 2015).

C. Regan, B.Y. Yang, K.C. Mayzel, J.C. Ramirez-San-Juan, P. Wilder-Smith, B. Choi, "Laser Speckle Imaging to Detect Pulsatile Flow in the Teeth," BMES Annual Conference, oral presentation. San Antonio, Texas (October 2014).

C. Regan, J.C. Ramirez-San-Juan, B. Choi, "Characterization of Subsurface Blood Flow Using Laser Speckle Imaging," ASLMS Annual Conference, oral presentation. Phoenix, Arizona (April 2014).

C. Regan, J.C. Ramirez-San-Juan, B. Choi, "Photothermal Laser Speckle Imaging," SPIE Photonics West, oral presentation. San Francisco, California (February 2014).

ABSTRACT OF THE DISSERTATION

Laser Speckle Imaging of Blood Flow Beneath Static Scattering Media

By

Caitlin Anderson Regan

Doctor of Philosophy in Biomedical Engineering

University of California, Irvine, 2017

Professor Bernard Choi, Chair

Laser speckle imaging (LSI) is a wide-field optical imaging technique that provides information about the movement of scattering particles in biological samples. LSI is used to create maps of relative blood flow and perfusion in samples such as the skin, brain, teeth, gingiva, and other biological tissues. The presence of static, or non-moving, optical scatterers affects the ability of LSI to provide true quantitative and spatially resolved measurements of blood flow. With *in vitro* experiments using tissue-simulating phantoms, we determined that temporal analysis of raw speckle image sequences improved the quantitative accuracy of LSI to measure flow beneath a static scattering layer. We then applied the temporal algorithm to assess the potential of LSI to monitor oral health. We designed and tested two generations of miniature LSI devices to measure flow in the pulpal chamber of teeth and in the gingiva. Our preliminary clinical pilot data indicated that speckle contrast may correlate with gingival health.

To improve visualization of subsurface blood vessels, we developed a technique called photothermal LSI. We applied a short pulse of laser energy to selectively perturb the motion of red blood cells, increasing the signal from vasculature relative to the

surroundings. To study the spectral and depth dependence of laser speckle contrast, we developed a Monte Carlo model of light and momentum transport to simulate speckle contrast. With an increase in the thickness of the overlying static-scattering layer, we observed a quadratic decrease in the quantity of dynamically scattered light collected by the detector. We next applied the model to study multi-exposure speckle imaging (MESI), a method that purportedly improves quantitative accuracy of subsurface blood flow measurements. We unexpectedly determined that MESI faced similar depth limitations as conventional LSI, findings that were supported by *in vitro* experimental data. Finally, we used the model to study the effects of epidermal melanin absorption on LSI, and demonstrated that speckle contrast is less sensitive to varying melanin content than reflectance. We then proposed a two-wavelength measurement protocol that may enable melanin-independent LSI measurements of blood flow in patients with varying skin types. In conclusion, through *in vitro* and *in silico* experiments, we were able to further the understanding of the depth dependent origins of laser speckle contrast as well as the inherent limitations of this technology.

INTRODUCTION

Laser speckle imaging (LSI) is a wide-field technique that relies on interference patterns of coherent light to give us information about the movement of scattering particles, typically red blood cells[1]. LSI has been used to generate maps of relative blood flow and perfusion of surface level microvasculature in the skin, brain, and retina[2,3,4]. However, a key limitation of LSI is that it has poor depth penetration. Signal from the vasculature is obscured due to optical scatterers in the dermis and epidermis above the blood vessels, which cause blurring of the image by scattering the interrogating light[5,6].

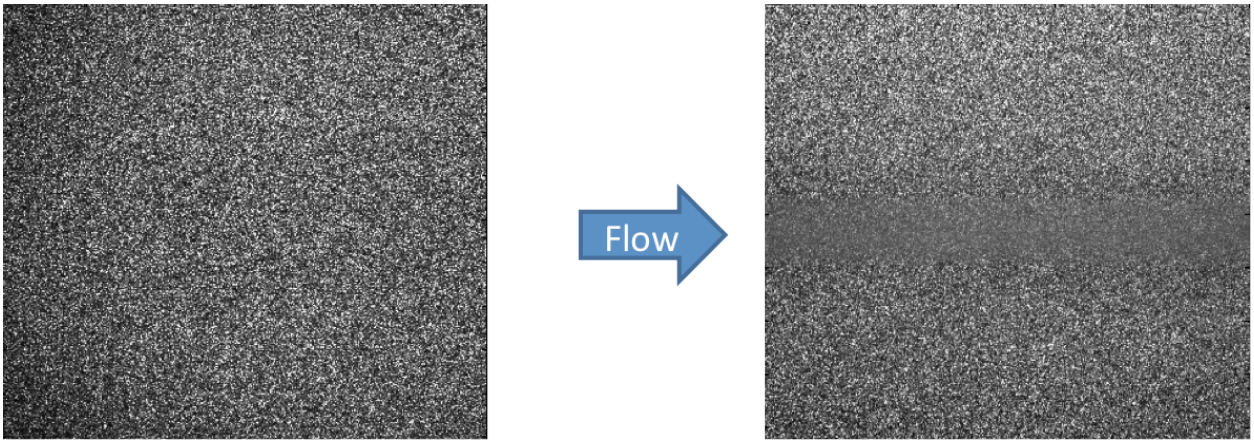

Figure 0.1: Raw speckle image of a static block (left) shows the interference pattern of coherent light in scattering media. When flow is introduced (right) the image becomes blurred due to fluctuations in the speckle pattern.

LSI relies on the constructive and destructive interference of coherent laser light to provide information about the motion of scattering particles in a sample[1,4,7,8]. When coherent light is incident on a scattering surface, it creates a pattern of slowly fluctuating light and dark speckles. The faster the illuminated scatterers are moving, the faster the speckles fluctuate in time. If the fluctuation of the speckle pattern is faster than the exposure time of the camera, the image will appear blurry. This blurring is quantified by a

metric known as speckle contrast, $K = \sigma / \langle I \rangle$, where K is the contrast value, and σ and $\langle I \rangle$ are the standard deviation and mean intensity in a small sub-region of the image. Therefore, as the motion of the scattering particles increases, for example, due to blood flowing faster, the value of K will decrease correspondingly (Fig 0.1).

Laser speckle contrast imaging is an extremely useful technique for generating wide-field image maps of relative blood flow and perfusion[7,8,1]. These maps are used in a variety of applications, from imaging vessels in the retina[4] or the brain[3], to observing perfusion in the liver during surgery[9], or the skin during treatment of port-wine stain birthmarks[10]. LSI is also used as a monitoring technique in many preclinical studies for treatment of vascular malformations, including pulsed dye laser therapy[11] and photodynamic therapy[12]. LSI has also been implemented in *in vivo* clinical studies of the brain[13]. While LSI works adequately for these applications, it is very limited in the ability to resolve vessels below the surface of static scattering layers such as the skin or the skull. Light is quickly scattered by these structures, obscuring the vessels. Perfusion information can be obtained up to few hundred microns depending on the optical properties of the surface layer, but to image clearly resolved microvasculature, the epidermis must be removed to expose vessels present in the dermis[14]. Removing the epidermis or the skull for imaging disturbs the physiology of the system, and cannot be done in human patients. Hence, improving this non-contact technique to allow enhanced subsurface vascular visualization is desirable.

Can we use image processing algorithms to improve the quantification of speckle contrast for flow below a static scattering layer (Chapter 1)?

There is a substantial collection of literature to support the use of traditional LSI as a visualization technique for microvasculature[1,2,3,4,5,6,7,8,9,10,11,12,13]. Various groups have different techniques for attempting to visualize deeper below the surface of a scattering layer, including alternative processing algorithms[5,15,16] and introducing exogenous contrast agents[17]. One common technique currently used to attempt to image deeper below a static scattering layer is modifying the speckle contrast processing algorithm. It has been suggested that measuring temporal contrast rather than spatial contrast allows more accurate values[18] and better visualization[5] of flow beneath a static scattering layer due to the fact that it is less sensitive to contributions from static scatterers[19]. Other processing schemes, such as the spatiotemporal contrast algorithm[15] or the motion-contrast algorithm[16] have also been demonstrated to improve visualization beneath a static scattering layer such as the skull.

Previous methods for improving the depth penetration of LSI involve the use of alternative processing schemes such as the motion contrast algorithm. We have implemented these algorithms with varying degrees of success, as they do not appear to work under many conditions. Based on previously published reports that the temporal processing algorithm may have a reduced sensitivity to static scattering, we investigated the quantitative accuracy of the standard spatial algorithm compared to temporal processing.

Can the temporal processing algorithm provide measurements of flow through static scattering in the teeth and gingiva to assess oral health (Chapter 2)?

One application space where improvements in quantitative accuracy of perfusion within thick scattering tissues may be valuable is monitoring health in the oral cavity[20]. The teeth consist of an array of highly scattering dentine tubules that radiate outwards from the pulpal chamber to the enamel[21]. To perform trans-illumination imaging of perfusion in the dental pulp, the laser light must pass through this thick region of static scattering[22]. The teeth also have variable thickness between people; therefore, to accurately quantify dynamic speckle contrast information through a variable range of static scattering requires the temporal processing algorithm[6]. Obtaining accurate information about pulpal perfusion is a key aspect of potentially assessing pulpal vitality[23,24]. In addition to the teeth, trans-illumination imaging of the gingiva is another area of interest for monitoring gingival health that faces similar challenges. The light must pass through static scattering structures such as the roots of the teeth, and the bone of the mandible and maxilla.

Can we externally modulate blood flow to improve the visualization of vascular structures below a static scattering layer (Chapter 3)?

In addition to modifying the processing algorithms for computing speckle contrast, experimental methods such as magnetomotive LSI have also been used to amplify the relative contrast between a channel and its surroundings[17]. This technique involves the injection of super paramagnetic iron oxide particles into the channel. Upon application of an alternating magnetic field, the particles move as they align back and forth in the AC field, resulting in an artificial change in contrast beyond what is seen due to regular flow.

However, the downside of this technique is that it requires introduction of an exogenous particle; furthermore, the set-up required to create an alternating magnetic field is not particularly adaptable beyond small *in vitro* experiments.

The notion of selectively inducing more motion to change contrast in a particular region, namely the blood vessels, has been proven to work as demonstrated by magnetomotive LSI[17]. Furthermore, the concept of causing targeted heating of vessels using a sub-therapeutic laser pulse at a wavelength specific to hemoglobin absorption is frequently used in PPTR[25,26,27,28,29,30]. Therefore, we expected that combining these two ideas in photothermal LSI will cause targeted heating in the red blood cells, which will induce a localized temperature dependent change in contrast. By selectively targeting absorption by hemoglobin molecules in red blood cells with the use of a photothermal excitation pulse, our goal was to enhance the contrast signal in the vascular network relative to the surrounding tissue using purely endogenous contrast agents. We were able to show this concept worked in both *in vitro* and *in vivo* experiments[31].

Absorption of 595nm light by hemoglobin causes a rapid spike in temperature of the red blood cells. When the sample absorbs the photothermal energy and converts it to heat, the resulting temperature rise causes an increase in motion of the scattering particles imaged by LSI. Rapidly changing the temperature of a liquid has a number of known effects including increasing the diffusive motion, volume expansion, the photoacoustic effect[32], changing the viscosity, and potentially altering the structure[33] and optical properties[34] of particles in the sample such as hemoglobin or red blood cells. Through a series of controlled *in vitro* experiments, we isolated which of these effects caused the increase in motion detected by our photothermal LSI technique[35].

Can we use Monte Carlo modeling to explain the depth limitations faced by LSI and explore the effects of factors such as optical properties, imaging configuration, blood volumes, and epidermal melanin on speckle contrast (Chapters 4 and 5)?

To further study the depth limitations apparent in visualizing vascular structures, we developed a Monte Carlo model of LSI. There are a number of published algorithms for Monte Carlo simulations of light transport through biological tissue[36,37]. A Monte Carlo simulation is a stochastic model that aggregates a large number of statistically related events to predict an outcome. In the case of light transport, the Monte Carlo approach involves propagating a large number of 'virtual photons' into the 'virtual tissue domain'. Each photon takes a step of a specified length and direction, and is potentially scattered or absorbed. Each step is calculated using a random number generator and the probability of an event occurring. The virtual photon is tracked throughout the course of travel through the tissue until it is terminated either by an absorption event or it crosses the upper or lower boundary of the virtual tissue domain, in which case it is considered reflected or transmitted respectively. The probability of scattering or absorption events occurring, and the direction in which the virtual photons are scattered is determined by the optical properties of the tissue, namely the scattering coefficient (μ_s), absorption coefficient (μ_a), and anisotropy factor (g) respectively. The output of standard light transport Monte Carlo models is a map of the fluence, or number of virtual photons that pass through a unit area, as well as the absorbance, reflectance, and transmittance of the virtual tissue.

In addition to published descriptions of light transport Monte Carlo algorithms, open access software is available from various sources[38]. For example, there is an interactive 'Virtual Photonics' software initiative that aims to provide open access to a

Virtual Tissue Simulator GUI for optical tissue irradiation[39,40]. However, at the present time, they do not have a published simulation of laser speckle contrast available to the public. In order to use Monte Carlo to predict speckle contrast, the momentum transfer, which is proportional to the number and direction of the total scattering events, must also be tabulated. While there are existing Monte Carlo models of light transport in tissue, few of them address speckle contrast[41].

A simulation of speckle contrast in the spatial frequency domain was modeled and tested by Rice et al[42]. Using principles from dynamic light scattering theory, the momentum transfer occurring during the virtual photon path through tissue can be tracked and converted into an electric field autocorrelation function[43]. This in turn is used to calculate speckle contrast using the Siegert relation to map the electric field autocorrelation function to intensity-based statistics, which is what is actually measured with speckle imaging. Spatial frequency domain imaging was used to measure the samples, and they were able to relatively accurately predict contrast values at different spatial frequencies for different wavelengths of light and different optical properties. They were also able to fit multi-frequency data with the model to estimate the diffusion coefficient of various samples.

This frequency domain simulation was also extended to a two-layer model that incorporated mixed static and dynamic scattering layers[44]. This situation is more complex because momentum transfer is now tracked by fraction of time in spent each layer, and the conversion to electric field autocorrelation function becomes a function of these conditional probability distributions. Rice et al used this model in conjunction with multi-exposure spatial frequency domain imaging to fit for a variety of variables including directed versus diffusive flow, the speed or diffusion coefficient, and the depth of the

second layer. We aimed to take the principles presented in these two studies for obtaining contrast from a momentum transfer probability distribution and apply it to our spatial domain forward simulation of speckle contrast. In addition to predicting a contrast value, in order to understand the depth limitations of LSI we also used the Monte Carlo model to quantify where the dynamic momentum transfer that contributes to the photon decorrelation took place.

Many factors affect speckle contrast values, including optical properties, laser wavelength, flow speed, fraction of dynamic scatterers, imaging configuration, and detector exposure time. For example, the main absorber in the skin is melanin, a pigment produced by melanocytes in the basal layer of the epidermis[45]. Melanin, especially brown and black eumelanin, strongly absorbs light in the ultraviolet, and visible wavelength range to protect DNA from photodamage[46]. The concentration of these pigments ranges from ~3%-30% in human skin[47]. Skin can be categorized by the Fitzpatrick Skin Type scale, which ranges from Types I to VI according to how sensitive the skin is to ultraviolet light (generally Type I is extremely fair skin, whereas Type VI is very dark skin). This presents challenges for many clinical optical imaging modalities[48,49], where patients have varying skin types and hence different concentrations of epidermal melanin, however the effects on LSI have not been quantified. The Monte Carlo model of speckle contrast allows systematic and controlled variation of these parameters that is not always possible with experimental LSI. Therefore, the effects and limitations of these parameters can be measured.

CHAPTER 1: Spatial versus temporal laser speckle contrast analysis in the presence of static optical scatterers

This work was originally published in the Journal of Biomedical Optics [6].

1.1 Abstract

Previously published data demonstrate that the temporal processing algorithm for laser speckle contrast imaging (LSCI) can improve the visibility of deep blood vessels, and is less susceptible to static speckle artifacts when compared with the spatial algorithm. To the best of my knowledge, the extent to which the temporal algorithm can accurately predict the speckle contrast associated with flow in deep blood vessels has not been quantified. Here, I employed two phantom systems and imaging setups (epi- and trans-illumination) to study the contrast predicted by the spatial and temporal algorithms in subsurface capillary tubes as a function of the camera exposure time and the actual flow speed. My data with both imaging setups suggest that the contrast predicted by the temporal algorithm, and therefore the relative flow speed, is nearly independent of the degree of static optical scattering that contributes to the overall measured speckle pattern. Collectively, these results strongly suggest the potential of temporal LSCI at a single exposure time to assess accurately changes in blood flow even in the presence of substantial static optical scattering.

1.2 Introduction

Laser Speckle Contrast Imaging (LSCI) is an optical technique based on calculating the contrast of an integrated speckle pattern, which allows us to analyze the dynamics of blood flow[4]. LSCI has attracted attention because it is able to image blood flow in skin[50], retina[51] and brain[3] at relatively high spatial and temporal resolution and without the need

for scanning of the region of interest. Additionally, it is simple and inexpensive relative to similar laser Doppler-based techniques[52,53]. During the last decade, the theoretical model behind LSCI has evolved to include modifications to the original Fercher and Briers model[54], including taking into account the effects of static optical scatterers[19,1], as well as the ratio of pixel and speckle sizes[55,56,18,57], resulting in the following speckle imaging equation:

$$K_{i,j} = \alpha^{1/2}\left[\sqrt{\tfrac{1}{M}}erf\left(\sqrt{\pi M}\right) - \left(\frac{1}{\pi M}\right)\left(1 - e^{-\pi M}\right)\right] \times \left[\rho_{i,j}^2 \frac{e^{-2x_{i,j}} - 1 + 2x_{i,j}}{2x_{i,j}^2} + 4\rho_{i,j}\left(1-\rho_{i,j}\right)\frac{e^{-x_{i,j}} - 1 + x_{i,j}}{x_{i,j}^2} + \left(1-\rho_{i,j}\right)^2\right]^{1/2} + K_{noise} \quad (1.1)$$

where $K_{i,j}$ is the local contrast of the raw speckle image at the pixel (i,j); α is a normalization parameter; M is the area of the pixel divided by the diffraction-limited area of the minimally-resolvable speckle; $\rho_{i,j}$ is the fraction of light reaching the pixel (i,j) that interacts with moving optical scatterers; and $x_{i,j} = T/\tau_C$ where T is the exposure time of the CCD camera and τ_C is the correlation time of the light intensity.

Research groups proposed various approaches to calculate speckle contrast from a raw speckle image or set of images[58]. Spatial analysis[59], probably the most common approach, implements a sliding, square structuring element of 5x5 or 7x7 pixels to calculate the local speckle contrast K as the standard deviation of pixel intensities (σ) divided by the mean intensity (I) within the element boundaries. Ideally, the speckle area should be at least twice the pixel area[55] to minimize detrimental effects due to spatial

integration of the speckle pattern[56], otherwise a correction factor should be applied to the measured speckle contrast[57]. The spatial algorithm requires only one raw speckle image to compute a contrast image, and therefore offers high temporal resolution at the expense of spatial resolution due to the use of the structuring element. To circumvent the reduction in spatial resolution, Cheng et al[60] proposed a temporal algorithm that calculates a speckle contrast image by computing K for each pixel across a sequence of images. This approach requires a minimum of 15 statistically independent images[60] and is associated with better spatial resolution at the expense of temporal resolution.

Recent studies describe results that support use of the temporal algorithm to analyze raw speckle images. We discovered that the temporal algorithm is more accurate than the spatial algorithm at assessing the relative change in flow speed[18]. This improved accuracy appears to be due to the reduction in sensitivity of temporal analysis to the presence of static optical scatterers[19,1,61]. Li et al[5] reported that the temporal algorithm enabled visualization of subsurface (> 1mm) blood vessels through the intact rat skull; these vessels were not visible in spatial speckle contrast images. Here, I report on *in-vitro* experiments that extend upon our understanding of temporal speckle contrast analysis. Specifically, I focused on the quantitation of speckle contrast and the impact of depth of fluid flow on speckle contrast values. I studied these effects using two clinically-relevant imaging geometries: epi-illumination and trans-illumination.

1.3 Materials and Methods

I used two separate phantom setups for the experiments described in this paper: 1) an epi-illuminated skin-simulating phantom (Fig 1.1), and 2) a trans-illuminated excised human tooth (Fig 1.2).

1.3.1 Skin-simulating phantom

I constructed the skin-simulating phantom using a silicone block containing appropriate concentrations of TiO_2 to mimic the reduced scattering coefficient ($1mm^{-1}$) of biological tissue at visible and near-infrared wavelengths. We embedded a glass capillary tube, with an inner diameter of 550μm, at the surface of the block. I placed a second thin silicone skin-simulating phantom of varying thickness (190μm -1000μm) on top of the block to mimic overlying tissue. I fabricated the thin phantoms using TiO_2 powder and coffee to simulate the optical scattering and absorption coefficients, respectively, of the epidermis[62]. By using different thicknesses of the overlying layer, I effectively modulated ρ.

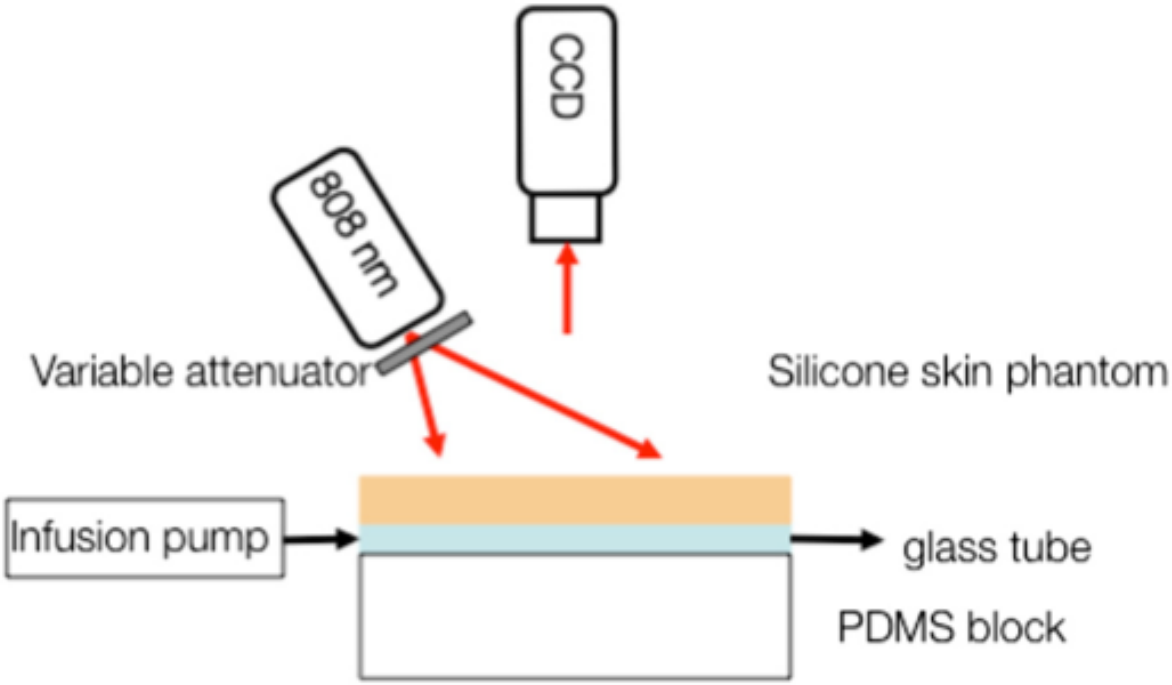

Figure 1.1: Experimental setup used for epi-illumination experiments. We infused 5% Intralipid into a glass capillary tube embedded at different depths from the surface of a two-layer silicone phantom geometry. We used epi-illumination with an 808nm laser and collected raw speckle images with a cooled CCD camera.

For LSI with epi-illumination, I used an 808nm laser (Ondax, Monrovia, CA) as the excitation source, with a variable attenuator to adjust the intensity of illumination and ground-glass diffuser to expand and homogenize the incident laser light (spot illumination: 5mm diameter). A Retiga EXi FAST cooled CCD camera (QImaging, Surrey, BC, Canada) collected the raw speckle images at 20 fps. The camera was equipped with a macro lens (Nikon, Melville, NY), with an aperture setting of f/4. I acquired images using Q-Capture Pro v5.1 software and selected the exposure time using the autoexpose function. I collected images of the phantom at exposure times ranging between 66μs to 43ms, by using the variable attenuator to change the irradiance of the excitation light. I collected data from the phantom with the following configurations: no top layer present (i.e.: microchannel at surface of phantom), and with overlying top-layer thicknesses (TLTs) of 190μm, 310μm, 510μm, and 1000μm. I used a syringe pump (Harvard Apparatus, Holliston, MA) to infuse 5% Intralipid solution as a blood surrogate (Baxter Healthcare, Deerfield, IL) into the channel at speeds of 0 to 18mm/s.

1.3.2 Tooth-simulating phantom

I also simulated trans-illumination LSI conditions, recently proposed by Stoianovici et al[20] for study of pulpal blood flow in teeth. Teeth are well suited for trans-illumination LSI due to the highly forward scattering feature of interior dentine tubules[22]. I used an excised human adult molar as a phantom. I drilled a small hole from the middle of the occlusal surface of the tooth to the bottom of the tooth between the roots. I inserted a Tygon tube with an inner diameter of 250μm into the hole and connected it to a syringe pump.

My experimental setup consisted of a configuration currently under investigation for study of pulpal blood flow. I illuminated the tooth on one side with a fiber-coupled 632.8nm HeNe laser (JDSU, Milpitas, CA). On the opposite side of the tooth, I positioned a leached fiber bundle (Schott, Southbridge, MA)[63] with a drum lens to focus the image on to a CCD camera (Flea3, Point Gray, Richmond, BC, Canada). I acquired images with FlyCap software (Point Gray, Richmond, BC, Canada) at a fixed exposure time of 10ms and a gain of 24dB. For this experiment, I calculated spatial and temporal contrast in two regions of interest, one on the left side of the tooth and one on the right. The tooth was approximately 300μm thicker on the right side than the left, effectively resulting in different ρ at the two interrogated regions.

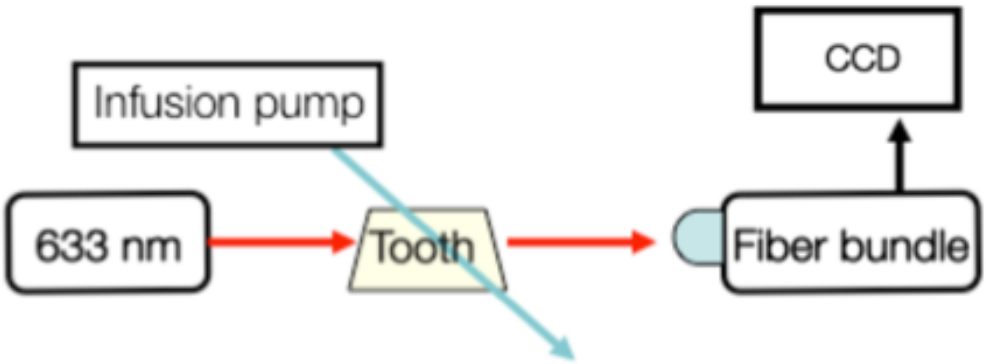

Figure 1.2: Experimental setup used for trans-illumination experiments. We infused Intralipid through Tygon tubing threaded through the tooth model. We trans-illuminated the tooth with a 632.8nm laser and collected images with a CCD camera via a fiber bundle.

With both experimental setups, I collected a sequence of 30 images per experimental condition and processed with both spatial and temporal speckle imaging algorithms. With the spatial algorithm, I used a sliding 7x7 pixel structuring element to calculate maps of speckle contrast from each acquired raw speckle image, and obtained a final contrast image

by averaging the 30 contrast images[59]. I calculated temporal contrast on a pixel-by-pixel basis, across all 30 images in the sequence[60]. All values shown in the data figures (Figs 1.3-1.6) represent the average contrast in a region of interest (20 x 100 pixels) positioned over the center of the tube.

1.4 Results and Discussion

1.4.1 Skin-Simulating Phantom

Similar to previously published data[19], for a given TLT, I observed that spatial speckle contrast decreased with an increase in T (Fig 1.3.a). For a given T, with an increase in TLT, the contrast increased due to a decrease in ρ. For a given flow speed, the contrast increased with an increase in TLT (Fig 1.3.b). Collectively, these data demonstrate that, for flow in a subsurface tube, spatial speckle contrast analysis is incapable of enabling unambiguous assessment of flow speed within the tube.

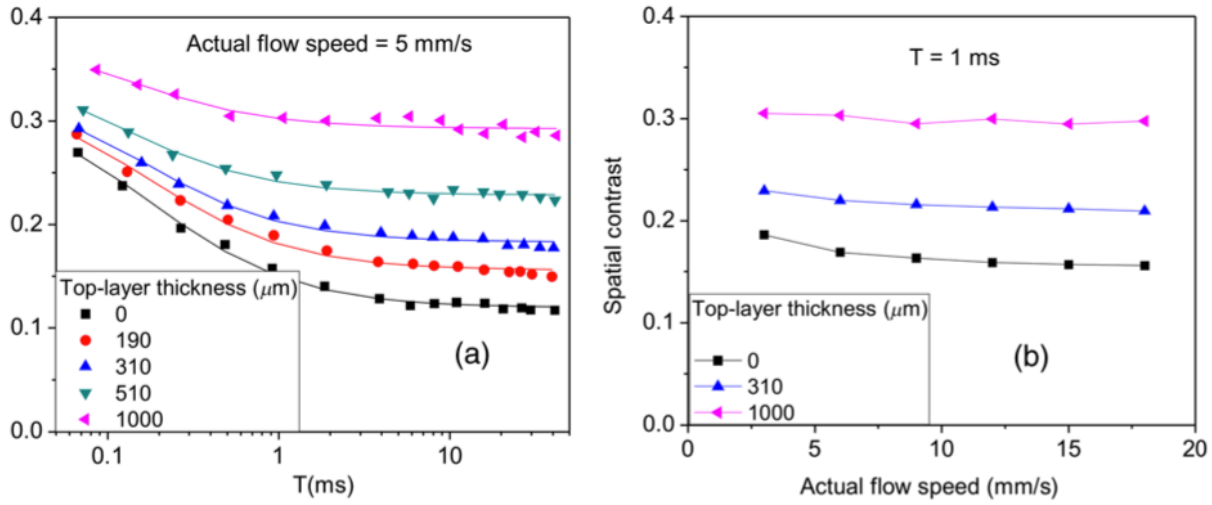

Figure 1.3: (a) Spatial speckle contrast increased with increasing top-layer thickness (TLT) at a given exposure time (T). The symbols represent experimental data and the continuous lines data fits using Eq. (1). (b) At T = 1ms, for a given actual flow speed value, spatial speckle contrast increased with increasing TLT.

For a given TLT (Fig 1.3.a), the spatial speckle contrast was maximum (K_M) at the shortest T, and then asymptotically decayed to a minimum (K_m). For a given T, the dynamic range of spatial speckle contrast (i.e., $\Delta K = K_M - K_m$) decreased with increasing TLT, due to a corresponding decrease in ρ. I fit Eq. (1.1) to the experimental data in Figure 1.3.a to estimate τ_c, ρ and K_m. From the fitting results, the mean value of τ_c was 61.0 ± 5.9 μs, which is similar to the values reported by Parthasarathy et al[19] for similar flow speed. ρ and K_m are plotted versus TLT in Figure 1.4. For a given actual flow speed, we observe an exponential decay of ρ with an increase in TLT (Fig 1.4.a), which we postulate is associated with the exponential behavior of light attenuation described by Beer's law. Due to the asymptotic behavior of K_m with increasing T (and hence increasing *x*), we determine K_m as:

$$K_m = \lim_{x\to\infty} K = \alpha^{1/2}\left[\sqrt{\tfrac{1}{M}}erf\left(\sqrt{\pi M}\right) - \left(\frac{1}{\pi M}\right)\left(1-e^{-\pi M}\right)\right](1-\rho) + K_{noise} \qquad (1.2)$$

where ρ ϵ [0,1]. From Eq. (1.2), we see that K_m decreases in a linear fashion with a decrease in TLT (Fig 1.4.a). From the first derivative of Eq. (1.1), we see that the sensitivity of spatial speckle contrast (dK/dT) decreases with an increase in TLT (Fig 1.4.b). Collectively, our experimental data and analysis using Eq. (1.1) demonstrate that spatial speckle contrast has a strong dependence on the fraction of nonmoving optical scatterers (i.e.: 1-ρ), which in turn depends on the TLT. Hence, spatial speckle contrast analysis is incapable of accurate quantitation of subsurface flow dynamics due to the impact of TLT on K.

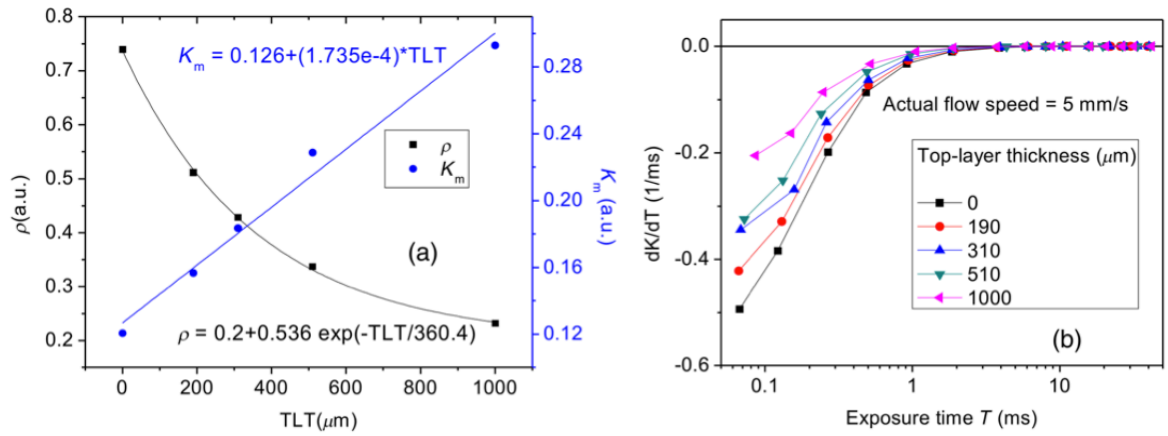

Figure 1.4: Spatial speckle contrast depends strongly on the fraction of nonmoving optical scatterers (e.g., 1-ρ) and hence on the TLT. (a) ρ decreases in exponential fashion with TLT, and K_m increases in linear fashion with TLT. Solid points represent experimental data, and lines represent fits to the data. (b) The sensitivity of K to exposure time T depends strongly on TLT, for short T (< 1 ms) the sensitivity decreases for thicker TL and for T > 1 ms the expected value of the contrast is constant (see Fig. 3a) and therefore the sensitivity approaches to zero.

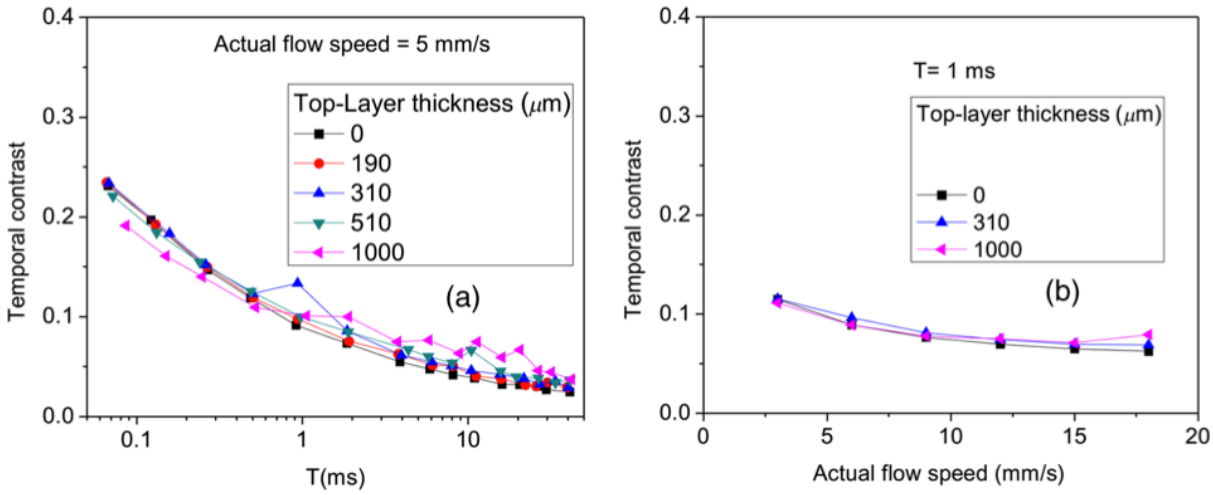

Figure 1.5: Temporal contrast vs. T (a) and vs. actual flow speed (b) with different TLT. The temporal processing scheme gives a more consistent measurement of contrast regardless of the presence of a static scattering layer.

Previous reports[19,18,5] present data that strongly suggest that temporal speckle contrast is altered primarily by temporal variations in light remitted from the sample and considerably less sensitive to static optical scatterers. I set out to determine the degree to

which temporal contrast depends on specific independent variables. I found that temporal contrast decreases with increasing T (Fig 1.5.a) and increasing flow speed (Fig 1.5.b), but I also observed that the contrast is relatively independent of TLT for a wide range of values (0 to 1000μm) (Fig 1.5).

1.4.2 Tooth-simulating phantom

I also studied this relationship using a trans-illumination LSI configuration, a setup previously proposed for study of teeth[20] and joints[64] and used routinely by our group to assess blood flow in the rodent dorsal window chamber model[14]. I used a tooth model in which the thickness of the right side of the tooth was approximately 300μm thicker than the left side, resulting in a higher proportion of static scatterers (i.e.: lower ρ). Similar to the data collected with the epi-illumination setup, I observed that spatial contrast depends on TLT (Fig 1.6.a) and temporal contrast is independent of TLT (Fig 1.6.b).

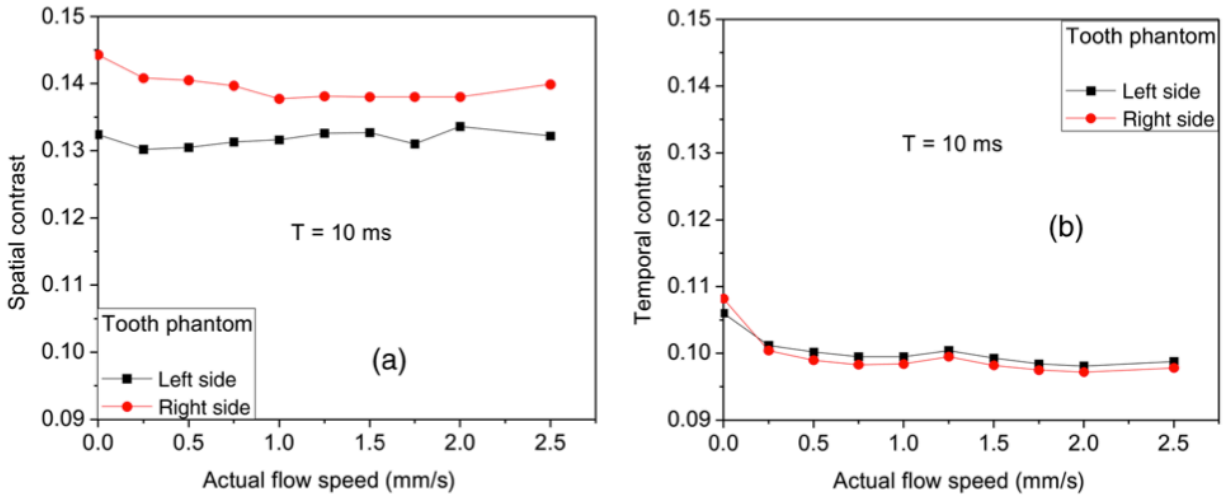

Figure 1.6: Spatial (a) vs temporal (b) contrast in different regions of interest on a tooth (different thickness) as a function of flow speed.

1.5 Conclusions

In this work, I studied the impact of overlying optical scatterers on measurements of speckle contrast. I used two different imaging setups and both spatial and temporal contrast analysis. With spatial analysis and epi-illumination, I determined that the speckle contrast offset K_m increases in a linear fashion with TLT (Fig 1.4.a) and the sensitivity of speckle contrast decreased with an increase in TLT (Fig 1.4.b). With temporal speckle contrast analysis (Fig 1.5), speckle contrast measurements were remarkably independent of TLT, presumably due to the relative immunity of temporal contrast to contributions from static optical scatterers[60,61,5]. My data demonstrate that temporal contrast analysis can characterize accurately speckle contrast due to subsurface moving scatterers for TLT as thick as 1mm, and for a wide range of T and flow speeds. I observed similar results with a trans-illumination geometry. Collectively, these results strongly suggest the potential of temporal LSI at a single exposure time to assess changes in blood flow even in the presence of substantial static optical scattering, which ultimately can be combined with methods to improve localization of speckle contrast, such as spatial frequency domain[65,44] or magnetomotive techniques[17].

1.6 Acknowledgements

This research was funded in part by CONACYT (CB-2010-156876-F), the Arnold and Mabel Beckman Foundation, and the National Institutes of Health (P41 EB015890, R01 DE022831, R01 HD065536).

CHAPTER 2: Clinical use of temporal laser speckle contrast analysis in the presence of static optical scatterers to oral health applications

In Chapter 1, I demonstrated that using the temporal algorithm to compute laser speckle contrast values provided more accurate quantification of relative flow than the spatial algorithm. Here, I applied the temporal algorithm in a trans-illumination geometry to quantify flow in the oral cavity for the purpose of studying oral health, in particular, the assessment of pulpal vitality and the diagnosis of gingivitis.

2.1 Fiber based laser speckle imaging for the detection of pulsatile flow

This work was originally published in Lasers in Surgery and Medicine[66].

2.1.1 Abstract

2.1.1.1 Background and Objective

In endodontics, a major diagnostic challenge is the accurate assessment of pulp status. In this study I designed and characterized a fiber-based laser speckle imaging system to study pulsatile blood flow in the tooth.

2.1.1.2 Study Design / Materials and Methods

To take trans-illuminated laser speckle images of the teeth, I built a custom fiber-based probe. To assess our ability to detect changes in pulsatile flow, I performed *in vitro* and preliminary *in vivo* tests on tissue-simulating phantoms and human teeth. I imaged flow of Intralipid in a glass microchannel at simulated heart rates ranging from 40 beats per minute (bpm) to 120bpm (0.67-2.00 Hz). I also collected *in vivo* data from the upper front incisors of healthy subjects. From the measured raw speckle data, I calculated temporal speckle contrast versus time. With frequency-domain analysis, I identified the frequency components of the contrast waveforms.

2.1.1.3 Results

With my approach, I observed *in vitro* the presence of pulsatile flow at different simulated heart rates. I characterized simulated heart rate with an accuracy of >98%. In the *in-vivo* proof-of-principle experiment, I measured heart rates of 69bpm, 90bpm, and 57bpm, which agreed with measurements of subject heart rate taken with a wearable, commercial pulse oximeter.

2.1.1.4 Conclusions

I designed, built, and tested the performance of a dental imaging probe. Data from *in vitro* and *in vivo* tests strongly suggest that this probe can detect the presence of pulsatile flow. LSI may enable endodontists to noninvasively assess pulpal vitality via direct measurement of blood flow.

2.1.2 Introduction

Tooth viability critically depends on blood flow within the dental pulp. Maxillofacial injuries or dental caries may induce a loss in pulpal blood flow, resulting in loss of viability and the need for root canal surgery[23,24]. To assess tooth vitality, clinicians currently use liquid CO_2 or electrical pulp testing to test the innervation of the tooth. The accuracy of these sensibility tests depends on the cooperation of the patient, and the tests themselves can be painful[24,67]. These tests have low sensitivity values, because they rely on the clinician's interpretation of a patient response. In particular, cold testing, heat testing, and electric pulp testing have sensitivities of 0.83, 0.86, and 0.72 respectively[67]. Therefore, these tests are associated with a high rate of false negatives, which leads to unnecessary root-canal treatment procedures[67].

A critical need exists for a pulpal vitality test with improved sensitivity and specificity. Assessment of blood flow is expected to better reflect the health status of a tooth[68]. To monitor blood flow, research groups previously studied use of optical methods such as laser Doppler flowmetry[69] and photoplethysmography[70]. Unfortunately, these methods suffer from key limitations that preclude them from routine clinical use. To maximize signal integrity, custom molds are required for each interrogated tooth[71]. Each mold requires considerable time and patient cooperation. The process of mold construction may prove to be difficult with patients who have a sensitive pharyngeal reflex[72].

We previously reported on the use of laser speckle imaging (LSI) to measure flow in excised human teeth[20]. Specifically, we demonstrated that trans-illumination LSI enables determination of flow. We based this trans-illumination approach on the previous observation that dentin tubules effectively act as light-guiding conduits that direct light primarily in the original propagation direction[21,22].

My overall objective was the development of a fiber-based LSI probe that enables measurements of pulsatile blood flow. Nadkarni et al.[63] described the use of leached fiber bundles for LSI of atherosclerotic plaques. They reported minimal leakage of light among the individual fibers, a characteristic that decreases the severity of artifacts induced by motion of the bundle itself. Based on this report, I designed and built a leached fiber-based imaging probe and compared its performance to an established open-air LSI system[10]. I developed an image analysis method based on temporal speckle contrast[61] and frequency-domain processing, and assessed the *in vitro* accuracy of our probe to simulated changes in heart rate. I finally report on an *in vivo* proof-of-principle validation of the performance of

the probe.

2.1.3 Materials and Methods

2.1.3.1 Imaging system

I developed a LSI probe (Fig 2.1.a) based on a 1mm diameter leached fiber bundle (Schott, Elmsford NY) coupled to a CCD camera (Flea3, Point Grey, Richmond, BC) (15). I used a custom-machined adjustable lens holder consisting of a hollowed out 5/16 hex bolt and a threaded plastic cap (Fig 2.1.b). The cap contained a 2mm diameter drum lens ~5mm past the threads. The leached fiber bundle was fixed in the bolt, which was threaded through the plastic cap. The cap was rotated to adjust the distance between the tip of the fiber and the drum lens to enable control of the fine focus of the imaging probe on the tooth. I used a 4x objective (Olympus, Center Valley, PA) and a mirror to image the fiber bundle on the camera sensor[73]. I used FlyCap software to collect all image sequences at 15 frames per second, using an exposure time of 10ms, and 24dB gain.

2.1.3.2 Fiber-bundle vs. open-air LSI

To characterize the ability of LSI through an imaging fiber bundle to measure flow, I first collected data from an *in vitro* flow phantom consisting of a glass microcapillary tube (inner diameter ~0.65mm). I embedded the tube at the surface of a silicone block containing TiO_2 to mimic the optical scattering ($\mu_s' = 1mm^{-1}$) of soft tissue[74]. I used a syringe pump (Harvard Apparatus, Holliston, MA) to infuse a solution of 5% Intralipid (Baxter, Deerfield, IL) through the tube at speeds ranging from 0 to 2mm/s, which spans the range from no-flow to an estimated average speed of blood in the tooth[75]. For these measurements, I used an epi-illumination configuration, in which light from a 632.8nm HeNe laser irradiated the phantom and the imaging fiber bundle was placed on the same

side of the phantom. I compared these measurements with data collected using a standard open-air LSI system[10] employing a scientific-grade, thermoelectrically-cooled CCD camera (Retiga EXi, QImaging, Surrey, BC).

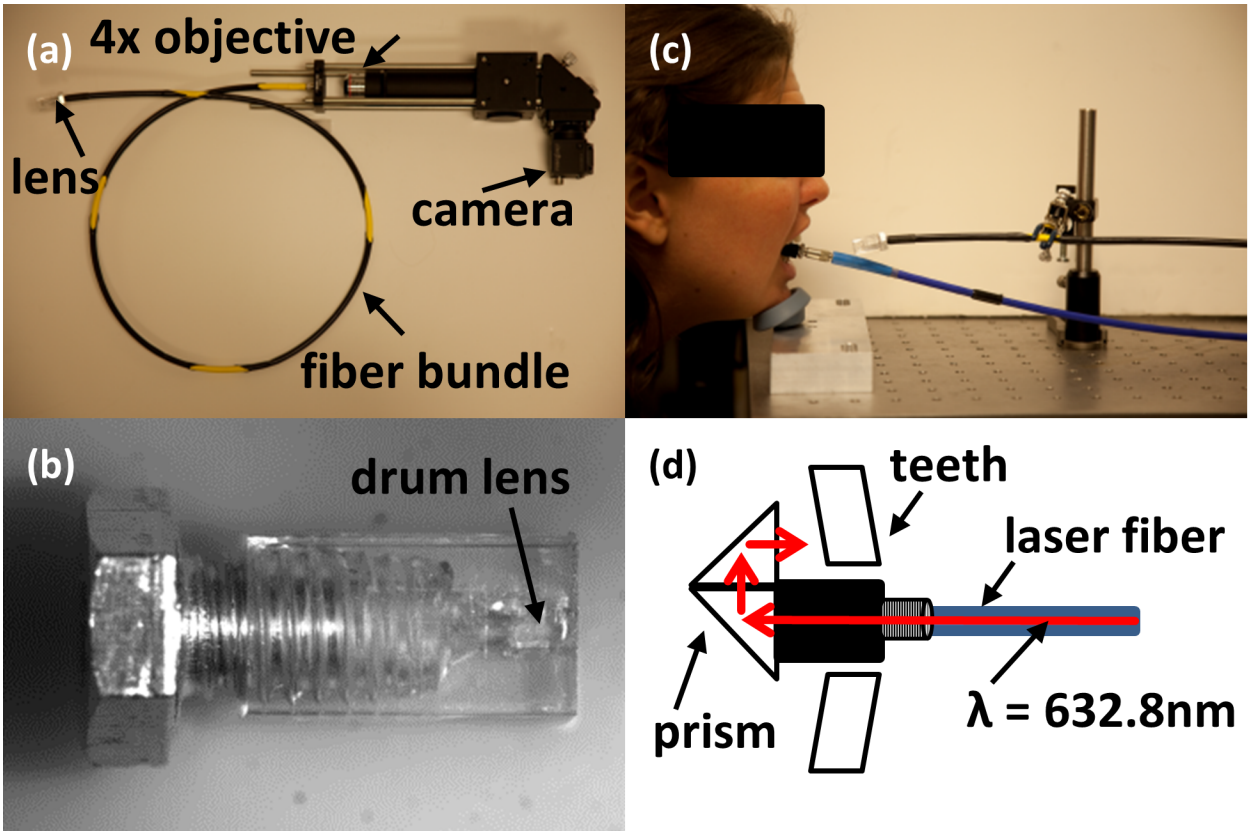

Figure 2.1: Design of fiber-based LSI probe. (a) The fiber-based LSI probe is composed of a leached fiber bundle with a lens at one end. The fiber bundle directs light through a 4x objective to the camera sensor. (b) A custom-built adjustable lens holder contains a 2mm drum lens. The imaging fiber fits through a hole down the center of the metal and plastic pieces. The plastic end rotates to allow for fine focusing by adjusting the distance between the end of the fiber bundle and the drum lens. (c) The imaging fiber bundle (black) is placed ~50mm from the subject. The laser fiber (blue) transmits laser light into the mouth, to the lingual side of the tooth. (d) The laser fiber (blue) is coupled with an SMA adapter to the retroreflector (black). This component contains two right-angle prisms (white) to redirect the light towards the lingual side of the tooth hence towards the imaging fiber bundle.

2.1.3.3 In vitro evaluation of LSI probe

To assess the performance of LSI with an imaging fiber bundle to characterize pulsatile flow, I collected additional *in vitro* image sequences of the flow phantom described above. I used a custom-built pulsatile pump to infuse 5% Intralipid with a pulse

rate varying from 0.67 to 2.00Hz, which corresponds to the range for physiological human heart rates[76].

2.1.3.4 In vivo evaluation of LSI probe

For *in vivo* transillumination LSI of a tooth, I first developed an optical delivery device suitable for use in the mouth (Fig 2.1.c). I coupled coherent light from a 632.8nm HeNe laser into a 1mm diameter optical fiber (Ocean Optics, Dunedin, FL). The fiber transmitted light into a custom 3D-printed plastic retroreflector containing two right-angle prisms (Fig 2.1.d). I coupled this device to the laser fiber via a SMA adapter. I designed the retroreflector to re-direct the light by 180^{o} to irradiate the lingual side of the tooth (Fig 2.1.d). As a first demonstration, with the fiber-bundle LSI probe, I collected *in vivo* image sequences from the buccal side of the upper front incisors of three healthy subjects. The subject bit down on the plastic piece to hold it steady behind the tooth of interest (Fig 2.1.c-2.1.d). I collected the data as part of a study approved by the Institutional Review Board at the University of California, Irvine.

2.1.3.5 Data Analysis

I used both spatial and temporal speckle analysis approaches, all written in MATLAB (The Mathworks Inc., Natick, MA), to analyze the image sequences. I computed spatial speckle contrast maps with the use of a standard 7x7 sliding window algorithm[1]; I then calculated an average spatial speckle contrast map as the average of 30 individual speckle contrast maps. I also used a standard temporal contrast algorithm[61] to compute temporal speckle contrast values across the same 30-frame sequence. To compute pulsatile speckle contrast waveforms, I used a rolling temporal algorithm. I computed the temporal contrast from the first five frames of the sequence (n=1-5), then for frames n=2-6, etc., for the entire

sequence. I linearly detrended the resultant contrast waveform to remove DC noise and applied a Fast Fourier Transform (FFT) to the signal. I analyzed the frequency-domain representation of the pulsatile waveform.

2.1.4 Results

2.1.4.1 Fiber-bundle vs. open-air LSI

Figure 2.2.a shows a brightfield image taken with the fiber-based LSI probe. The honeycomb pattern apparent in the image (and shown magnified in the inset) represents the individual 8.5µm diameter fibers that comprise the leached fiber bundle. With the lens placed ~50mm away from the subject, the standard usable field-of-view of the probe is ~14mm in diameter (Fig 2.2.a).

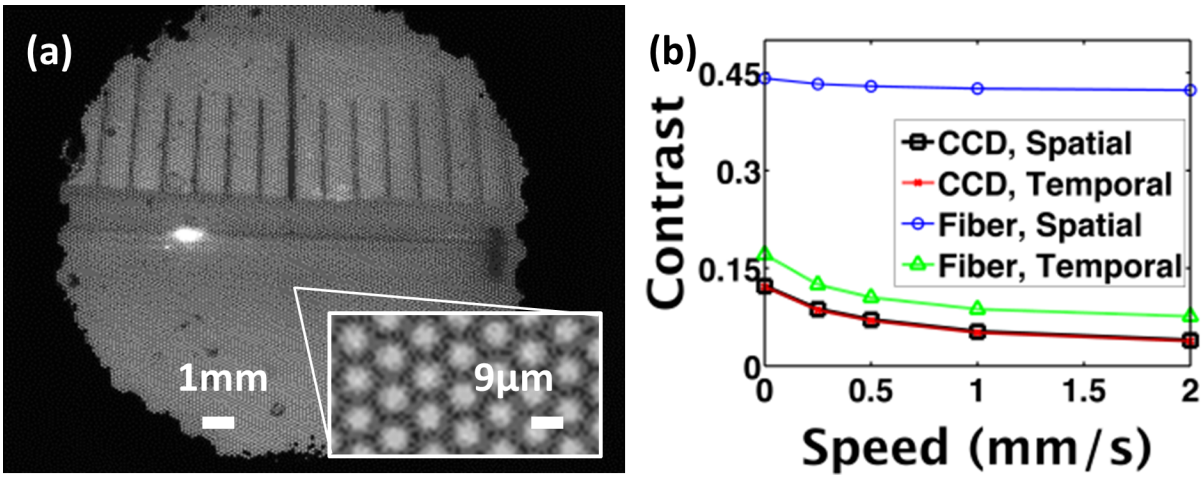

Figure 2.2: (a) Representative broadband image of a millimeter ruler through the fiber bundle. The inset shows the honeycomb pattern formed by the individual fibers (8.5µm diameter) comprising the bundle. (b) Comparison of contrast versus flow speed in the fiber-based system and the conventional open-air CCD-based system using spatial and temporal processing methods [with the CCD system, the spatial (black) and temporal (red) curves directly overlap]. With the spatial algorithm, the fiber-based system is less sensitive to changes in flow speed. However, the temporal contrast curve for the fiber-based probe has the same contrast response to flow speed as the CCD-based system.

I compared the contrast at different flow speeds using the fiber-based LSI probe and the open-air LSI system describe above. I calculated contrast using both spatial and temporal processing algorithms to assess the effects of the honeycomb artifact on contrast values. Spatial and temporal contrast values with the standard open-air system are identical, and decreased as expected when flow speed increased (Fig 2.2.b). The temporal contrast values were slightly higher using the fiber-based system, but they follow the same trend and have a similar slope as those measured with the open-air system. However, the spatial contrast values using the fiber-based LSI probe are significantly higher and do not demonstrate the same dynamic range as the temporal algorithm or the scientific CCD camera-based system. Using the CCD system as the gold-standard for LSI measurements, if we compare the slopes between each subsequent measurement for the fiber-based spatial contrast curve relative to the scientific system, the fiber-based system slopes are associated with an error greater than 75%.

2.1.4.2 Evaluation of fiber-based LSI to characterize in vitro and in vivo pulsatile flow

The combination of my fiber-based LSI probe and rolling temporal processing algorithm enables *in vitro* identification of the presence of pulsatile flow at different frequencies (Fig 2.3). Figure 2.3 shows results from my *in vitro* pulsatile pump tests at frequencies ranging from 40bpm to 120bpm (0.67-2.00 Hz), to span the physiological range of human heart rates[76]. Based on qualitative analysis of the *in vitro* contrast waveform, I observed a pulsatile component. The corresponding frequency domain analysis (Fig 2.3) confirmed the presence of the expected frequencies. With stationary Intralipid, the signal strength is predominantly at DC (0Hz). The power of the FFT peak

decreased as the frequency of the signal increased; however, at all frequencies it is clearly distinguishable from the no-flow signal at 0Hz, and the peak is present at the expected frequency with an accuracy of ≥98% (Fig 2.3).

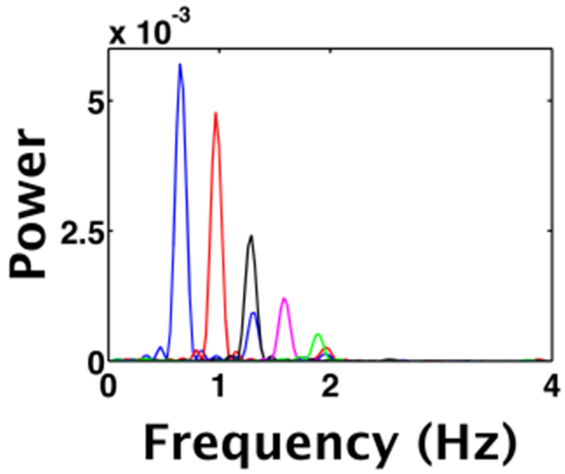

Frequency	Error
40 bpm	1.39%
60 bpm	0.42%
80 bpm	0.54%
100 bpm	0.33%
120 bpm	0.62%

Figure 2.3: (a) Frequency analysis of *in-vitro* contrast waveforms resulting from use of the rolling temporal algorithm. We can clearly identify each of the different pulsatile frequencies [0.66 Hz (40bpm) – 2.00Hz (120bpm)] of the pump. The error between the detected peak frequency and the actual frequency is less that 1.4% for all the measured frequencies.

I also collected measurements from the upper incisors of three subjects with healthy teeth (Fig 2.4). In the first subject, the main frequency signal detected was slightly above 1 Hz, at a frequency of 69bpm (Fig 2.4.a), which matched the recorded heart rate measured with a wearable commercial pulse oximeter. The second subject had a higher recorded heart rate, and I detected the main frequency signal at 90bpm (Fig 2.4.b). I detected the main frequency peak in the physiological range to be 57bpm for subject three (Fig 2.4.c), which also matched their measured heart rate.

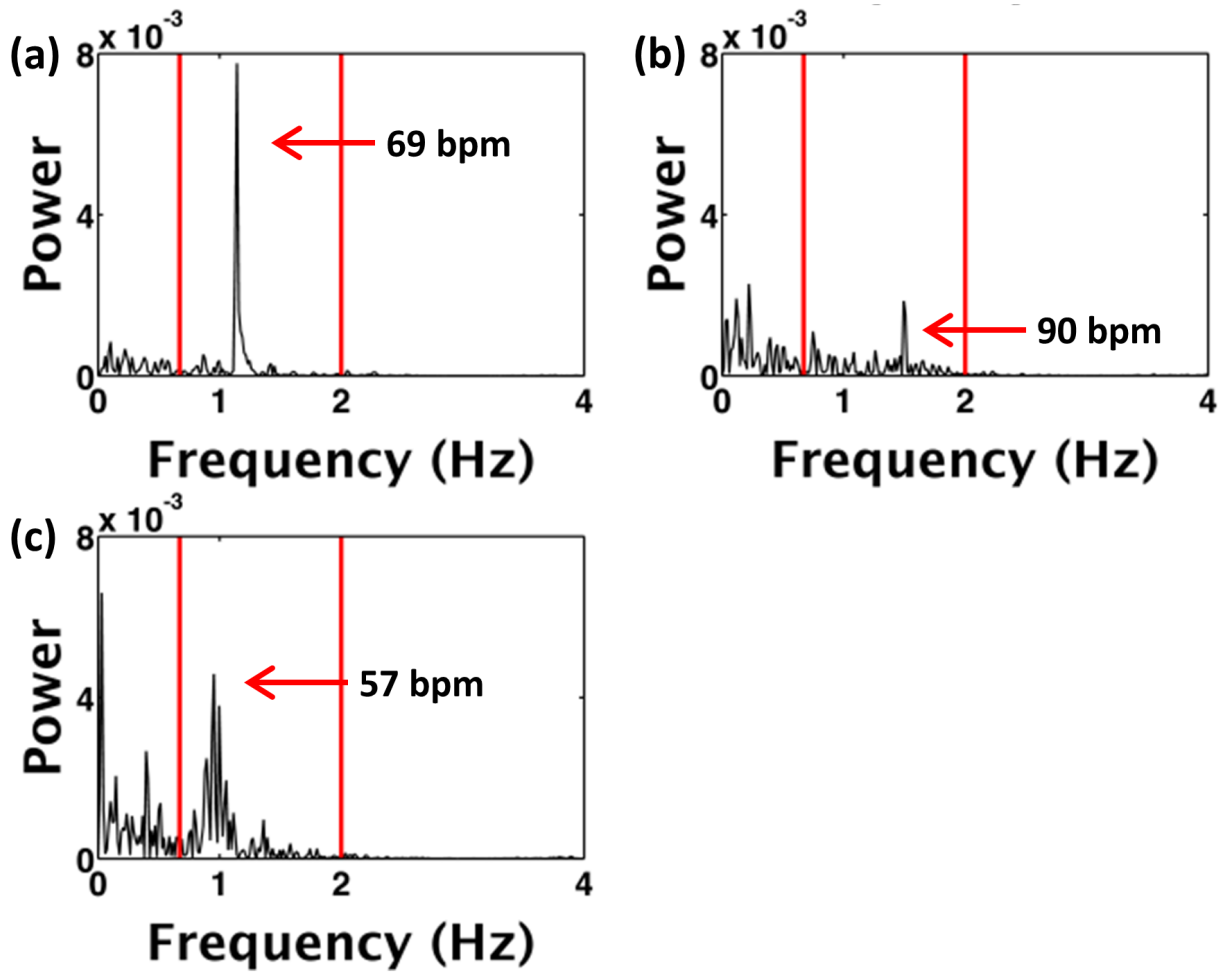

Figure 2.4: Frequency analysis of signal from the healthy upper incisor of three subjects. The range of physiological heart rate frequencies (0.67-2.00Hz) is bounded by the red lines. (a) There is a peak just above 1 Hz (at 69bpm) that corresponds to the measured heart rate of the subject. (b) This subject had a higher resting heart rate, and the peak in the physiological range is present at 1.5Hz (90bpm). (c) This subject has a heart rate peak present near 1Hz (at 57bpm). There is some low frequency noise present in the signal, below the physiological range, which is probably due to motion artifacts.

2.1.5 Discussion

I built and validated a fiber-based LSI probe, to detect pulsatile flow (Fig 2.1). I compared two different processing algorithms to compute speckle contrast from the raw image data (Fig 2.2). I demonstrated the ability of the probe to characterize pulsatile flow in both an *in vitro* system (Fig 2.3) and *in vivo* in human subjects (Fig 2.4). Collectively, my

findings demonstrate the ability of the LSI methodology to assess the presence of pulsatile blood flow.

Current methods for diagnosing pulpal vitality are called sensibility tests. These tests involve the application of a stimulus, usually either heat, cold, or an electric pulse, to the tooth and rely on an assessment of the patient's response by the clinician[23,24,67]. These tests can be painful, and are a subjective measure of innervation rather than blood flow. Additionally, primary and immature teeth lack the neurons that respond to thermal and electrical tests, making these tests inaccurate in children and teenagers[77]. These tests have low reported sensitivity values: 0.86, 0.83, and 0.72 for heat, cold, and electric pulp testing respectively[67]. Therefore, there is a high rate of false negatives, meaning root canal treatments are performed on teeth that still had blood flow and were viable. My results suggest that LSI can detect pulsatile flow in teeth, which I postulate will lead to a painless, quantitative, objective assessment of pulpal vitality.

Temporal speckle contrast was more sensitive to changes in flow than the spatial contrast (Fig 2.2.b). I believe this effect is due to the honeycomb pattern associated with the individual fibers of the leached fiber bundle (Fig 2.2.a). This pattern artificially introduces zero intensity values into the image, which increases the standard deviation of intensity values in the sliding window, while simultaneously decreasing the mean intensity in the same region. This has the effect of increasing contrast values, and decreasing the influence of the desired blood-flow component of the signal. However, with the temporal algorithm, the honeycomb pattern is fixed in space, mitigating its effect on subsequent analysis of the signal of interest (Fig 2.2.a).

I processed the raw speckle data with both the spatial and temporal algorithms to assess if I could use a single deterministic value to threshold between "flow" and "no-flow" conditions. This approach previously was proposed as a potential method for measuring pulpal vitality[20]. Here, I found a slightly higher sensitivity to changes between "no-flow" (0.0 mm/sec) and "flow" (0.25-2.0 mm/sec) conditions when I used the temporal algorithm as compared to the spatial algorithm (27% relative change vs 2% relative change, respectively), further confirming that temporal processing was more suitable for LSI with a fiber bundle. This maximum difference in "flow" and "no-flow" contrast values is small, even under ideal, controlled conditions. I observed that the change in average *in vivo* contrast values from the upper incisors of a single subject collected during separate imaging sessions, consistently differ (>50% of the time) by more than the contrast value change measured *in vitro* between simulated no-flow and flow conditions (Fig 2.2.b).

Hence, my data suggests that the use of a single contrast value to diagnose pulpal vitality is flawed. As an interferometric technique, LSI is extremely sensitive to motion. Since LSI typically measures relative changes in motion rather than absolute values, I determined that using a single threshold speckle contrast value, as proposed previously[20], is not feasible *in vivo*. Any external movement or vibrations of the fiber probe lead to changes in the absolute contrast values. Changes in the orientation of the device relative to the tooth, or the uniformity of the laser illumination may also cause a change in the measured contrast. I also previously demonstrated that speckle contrast values may even vary intra-tooth due to local variations in tooth thickness[6].

Due to this result, I instead investigated the ability of frequency-domain analysis of speckle contrast data to assess pulpal blood flow. With my probe and analysis method, I

accurately characterized the pulsatile flow both with an *in vitro* flow system (Fig 2.3) and *in vivo* in three human subjects (Fig 2.4). I distinguished between the presence and absence of a pulsatile signal in the *in vitro* system by analyzing the contrast waveform in the frequency domain. By taking data from healthy human incisors, I demonstrated that my system is also capable of detecting pulsatile flow *in vivo* (Fig 2.4). Figure 2.4.a shows a clear-cut result from a subject with a high signal to noise waveform, and the peak at 69bpm is clearly visible. The subject measured in Figure 2.4.b had a higher resting heart rate of 90bpm, which demonstrates that the technique is sensitive to different frequencies. There is more low frequency noise present in Figures 2.4.b and 2.4.c, which I believe is due to motion artifacts such as motion of the subject's head relative to the imaging fiber bundle, or incidental movement of the laser fiber. However, these additional frequency spikes lay outside of the physiological heart rate range, indicated by the red lines[76], and could potentially be removed with more advanced signal processing methods. Another potential source of noise is demonstrated in Figure 2.4.c. There is a clear peak at 57bpm, however other frequencies surrounding this peak in the FFT spectrum exist and may be due to the fact that heart rate *in vivo* is not perfectly constant, and fluctuates during the measurement period by a few beats per minute. I postulate that endodontists can use such frequency-based information to assess the presence of blood flow in a tooth, making this a critical step in achieving a clinic-ready solution to this diagnostic challenge.

Although the current fiber-based probe enables flow characterization in teeth, I propose that design improvements will make the probe more robust. Since LSI is inherently sensitive to motion artifacts, further efforts should involve improvement on the fiber design, removal of the honeycomb artifact, or perhaps avoid use of fibers altogether

for this specific application. With continued progress made in consumer-grade optical and electronic components, miniaturization of the probe is a desired outcome, and is the subject of future work. For example, a miniaturized probe that clips onto a tooth or fits into a dental mouthguard may help reduce motion artifacts as well as improve our access to other teeth such as the molars.

In conclusion, here I describe a first-generation LSI probe that enables characterization of pulsatile flow. I proposed the use of frequency-domain analysis of temporal speckle contrast waveforms to assess the pulsatile frequency of blood flow, both *in vitro* and *in vivo.* My data demonstrate the potential of LSI as a simple pulpal vitality test that avoids noxious stimuli and directly assesses blood flow as opposed to pulpal innervation.

2.1.6 Acknowledgements

This research was funded in part by CONACYT (CB-2010-156876-F), the American Society for Laser Medicine and Surgery, the Arnold and Mabel Beckman Foundation, the National Institute of Health (R01 DE022831), the National Institute of Health Laser Microbeam and Medical Program (P41 EB015890) and the NSF BEST IGERT program (DGE-1144901). I would like to thank Kevin Dilger and Ted Chang (UC-Irvine) for design of the custom pulsatile flow pump. I would also like to thank Jan O'Dell (DDS) for her insightful clinical perspective.

2.1.7. Limitations and Future Work

As noted in the discussion above (2.1.5), the fiber-bundle based LSI device had significant issues with motion artifact, which led to the development of a more stable, miniaturized LSI system described in Chapter 2.2. However, another potential problem that

was eventually discovered with attempts to measure blood flow from the pulpal chamber is the potential for contamination of the speckle contrast signal with signal from blood flow in the gingiva. The contamination is likely due to the highly scattering nature of light in the tooth structure, as well as the fact that the gingival blood volume is orders of magnitude higher than the blood volume of the pulpal chamber. Additionally, the pulpal chamber may be closer to the root of the tooth rather than the crown, and hence not directly in the path of our trans-illuminated light.

I initially believed this signal contamination would not occur to due simulations of light transport presented by Kakino et al[22]. However, after further consideration of the data, I believe that signal from blood flow in the gingiva may be contributing to the *in vivo* pulsatile signal I detected.

This hypothesis is difficult to test due to the inability to isolate an *in vivo* tooth from the gingiva. One potential method of testing my system's vulnerability to signal contamination is by taking LSI measurements of patients who have had root canal therapy. These patients should not present any pulsatile signal because there is no longer blood flow in their teeth.

To determine if there is future potential for LSI to assess pulpal vitality the following factors should be taken into consideration. First, a better understanding of the nature of flow in the pulpal chamber is necessary to understand the precise location of the pulp as well as if the flow present in this region is even pulsatile. This information should be used to perform computational modeling of light transport and scattering in the teeth and gingiva using the techniques described in Chapter 5. This will allow a more informed decision about the ability to detect and isolate signal from the pulp chamber. Second, the

imaging set-up must be more stable. Efforts to accomplish this are described below in Chapter 2.2. Third, hardware improvements are necessary to improve the LSI signal obtained. The camera used in the study below has inherent limitations, which impede the ability to detect the extremely small changes in speckle contrast signal that may be associated with pulpal blood flow. More advanced signal processing algorithms to differentiate pulsatile signal from noise may also be necessary. Finally, based on the results of light transport simulations, measuring LSI with different orientations of the laser and the camera, for example arranging them perpendicularly, may be required to maximize signal coming from the pulpal chamber.

In addition to attempting to isolate blood flow in the dental pulp, I decided to intentionally measure gingival perfusion. The process to improve my oral LSI device and explore applications for quantifying gingival perfusion are described below in Chapter 2.2.

2.2 Design and evaluation of a miniature laser speckle imaging device to assess gingival health

This work was originally published in the Journal of Biomedical Optics[78].

2.2.1 Abstract

Current methods used to assess gingivitis are qualitative and subjective. I hypothesized that gingival perfusion measurements could provide a quantitative metric of disease severity. I constructed a compact laser speckle imaging (LSI) system that could be mounted in custom-made oral molds. Rigid fixation of the LSI system in the oral cavity enabled measurement of blood flow in the gingiva. *In vitro* validation performed in controlled flow phantoms demonstrated that the compact LSI system had comparable accuracy and linearity compared to a conventional bench-top LSI setup. *In vivo* validation demonstrated that the compact LSI system was capable of measuring expected blood flow dynamics during a standard post-occlusive reactive hyperemia and that the compact LSI system could be used to measure gingival blood flow repeatedly without significant variation in measured blood flow values ($p<0.05$). Finally, compact LSI system measurements were collected from the interdental papilla of nine subjects and compared to a clinical assessment of gingival bleeding on probing. A statistically significant correlation ($\rho=0.53$; $p<0.005$) was found between these variables, indicating that quantitative gingival perfusion measurements performed using this system may aid in the diagnosis and prognosis of periodontal disease.

2.2.2 Introduction

Gingivitis is a disease caused by a buildup of dental plaque, a bacterial biofilm, on the teeth and in the gingival sulcus. Symptoms of gingivitis include inflammation of the

gingiva, which can result in redness, tenderness, and swelling of the gums, as well as bleeding during brushing or flossing[79,80,81]. Current methods to diagnose gingivitis include visual inspection and mechanical probing of the gingiva by a dentist who scores gingival health on a 0-3 scale, where 0 corresponds to healthy gingiva and a 3 indicates severe inflammation and bleeding[82,83]. However, the results of this assessment technique are qualitative and subjective[83]. Alternatively, enzymatic biomarkers in the saliva and crevicular fluid can be used for diagnosis, but such tests are time consuming and expensive[84,85]. I hypothesize that there are associated changes in gingival perfusion that accompany gingivitis[81], and that laser speckle imaging (LSI) can be used to quantitatively measure those changes, potentially providing a simple method for objective diagnosis of periodontal disease and evaluation of treatment approaches.

LSI is a widefield technique used to visualize and quantify blood flow. It was developed in 1981 by Fercher and Briers to image vasculature in the retina[4], and has since been employed to monitor flow in the brain, skin, and other organs[3,2,9]. LSI utilizes image processing techniques to quantify flow with a value known as speckle contrast, which is inversely proportional to the speed and quantity of red blood cells moving through the imaging volume[1].

A wide variety of LSI system embodiments exist, including clinical systems, benchtop laboratory systems, and microscopy-based systems[4,3,2,9,1,86,66,87]. Such embodiments can range in size from handheld to larger cart-based or tabletop instruments. To enable LSI measurements of the gingiva, the imaging system used must be miniaturized such that it can be easily positioned and stabilized in the oral cavity. Further, to facilitate clinical integration, the system must also be simple to use and perform measurements

relatively quickly. My goal was therefore to design a miniature dental LSI probe with the following features: 1) small enough to be securely positioned in the mouth, 2) simple to use, 3) capable of producing accurate blood flow measurements, 4) sufficiently rapid to collect data within five minutes per measurement, and 5) able to provide a quantitative metric correlated to disease.

A number of challenges exist that are associated with creating a compact LSI system for use in the oral cavity. First, each component must be small enough to fit relatively comfortably in the mouth. Furthermore, all electrical components must be housed to keep them dry and free of saliva. Additionally, they must be able to withstand sterilization between subject measurements. Finally, without affixing the imaging components to the teeth or gingiva, significant motion artifact may be introduced, making handheld systems or external imaging systems potentially untenable. I previously published on the ability to measure pulsatile blood flow in the teeth using a fiber bundle-based LSI device that required each subject to hold their head steady while biting down on a laser fiber[66]. However, this system was difficult or uncomfortable for some subjects and hence may not be suitable for widespread clinical use.

Here we describe a LSI system that uses components small enough to be mounted completely within the oral cavity. This was accomplished by using a miniature CMOS camera (volume of approximately $2mm^3$) and a compact laser diode package that could be fixed in place within the mouth using custom molds fabricated from dental impression putty. Using these molds, the laser diode and camera could be mounted on the buccal and lingual side of the gingiva and be used to perform LSI in a trans-illumination geometry[66,20]. Using this system, I performed *in vitro* experiments to assess the stability, precision, and

repeatability of the device to collect speckle contrast data. I additionally performed an *in vivo* pilot study using my system to measure perfusion in the gingiva above the upper incisors in subjects diagnosed with mild to severe gingivitis, and correlated the measured speckle contrast values with clinical assessments.

2.2.3 Materials and Methods

2.2.3.1 Use of human subjects

All subject measurements were approved by the Institutional Review Board of the University of California, Irvine.

2.2.3.2 Device design

The compact camera used in the LSI system is an Awaiba NanEye CMOS camera (CMOSIS, Raleigh, NC). It is equipped with a f/# 2.7 lens, which has an 8-75mm depth of focus and utilizes a rolling shutter during image acquisition. The entire package (camera and lens) measures 1.0x1.0x1.7mm, which allows for comfortable intraoral use. The NanEye has a 4-pin connection to a USB2 evaluation board that connects to a PC running provided software (Awaiba Viewer v2.15.2.1). To protect the camera and camera wiring, it was secured in a 3D-printed casing using hot melt adhesive. The case also provided additional material with which to stabilize the camera during use. I calculated a ratio of ~1.93 speckles/pixel with this current configuration, which is very close to the Nyquist criteria for speckle sampling[55,18]. A 90mW, 785nm, single longitudinal mode, 5.6mm diameter TO can package laser diode (Roithner LaserTechnik GmbH, Vienna, Austria) was used as the coherent light source. The laser diode was powered by the LDC500 laser diode controller (ThorLabs Inc, Newton, NJ). The diode was housed within a custom machined cylindrical casing fabricated from delrin. The casing also contained an aluminum heat sink

to aid in diode stabilization.

2.2.3.3 Image Processing

During data collection, "color reconstruction" and "reduce processing" options in the Awaiba Viewer software were turned off and on, respectively, to ensure raw data was collected. The proprietary Awaiba Viewer software saved data as AVI files, which were converted to a TIFF image sequence using ImageJ software (NIH), followed by computing speckle contrast maps from each image using MATLAB (MathWorks, Natick, MA). Temporal speckle contrast was calculated as the standard deviation over the mean intensity in each pixel across a series of images[61]. I used a rolling temporal contrast value calculated by computing temporal contrast across each pixel of subsequent four-frame sequences[66] (ie: frames 1:4, 2:5, 3:6, etc). I then averaged the contrast within a user-selectable region of interest (ROI) pertaining to the gingival tissue of interest.

2.2.3.4 Static in vitro device validation

To test the stability of the NanEye camera and the laser diode to be used during *in vivo* data collection, I measured a 1% Intralipid solution (Baxter Healthcare, Deerfield, IL) over a period of three minutes using the NanEye camera to quantify the changes in speckle contrast not resulting from direct movement or flow. Image sequences were collected at 30 frames per second (fps) with an exposure time of 5ms. A 70x70 pixel ROI was chosen to compute the temporal speckle contrast. This measurement was performed at several different intensities (9-155 counts) resulting from different currents applied to the laser diode, spanning the dynamic range of the NanEye camera to determine the dependence of illumination intensity on measured speckle contrast. I computed the coefficient of variation

(CV, equal to standard deviation / mean) across the three-minute data sets to assess the stability of the system.

2.2.3.5 Dynamic in vitro device validation

I performed *in vitro* experiments to validate the NanEye camera for use in LSI. A flow phantom was fabricated using polydimethylsiloxane (PDMS) with titanium dioxide added to give a reduced scattering coefficient of $1mm^{-1}$, which is typical of tissue[74]. A glass microchannel with diameter 650μm was embedded in the surface of the PDMS, and 1% Intralipid was infused at different speeds (0.25mm/s, 0.5mm/s, and 1.0-5.0mm/s in 1mm/s increments) using a syringe pump (Harvard Apparatus, Holliston, MA).

I performed the *in vitro* validation imaging by comparing the NanEye camera and a monochrome Chameleon3 camera (Point Grey, Richmond, BC, Canada), a research grade CCD camera equipped with a 60mm Nikkor Micro Lens (Nikon, Melville, NY) with f/# 2.8. I coupled the diode from the device to a beam expander and a ground glass diffuser to diffusely illuminate the flow phantom, and collected sequences of reflectance speckle images with the NanEye and Chameleon3 cameras. Images were collected using an exposure time of 5ms, and a frame rate of 30fps. Temporal speckle contrast was computed in a 7x66 pixel region within the center of the microchannel for ~200 frames, and then averaged to improve the signal to noise ratio.

2.2.3.6 In vivo data collection setup

Prior to the imaging of each subject, I created a custom-fit impression mold of the upper anterior teeth and gingiva. All measurements were taken from the gingiva above the upper incisors. The molds were made with ~50g of Zetalabor C-silicone (Hard 85 Shore A) polysiloxane dental impression material (Zhermack Inc, River Edge, NJ) combined with

~1g of Indurent gel catalyst (Zhermack Inc, River Edge, NJ). The dental putty and catalyst were mixed by hand for ~60s and then formed into a rectangular block of approximately 2x2x6cm. I created an impression of the subject's teeth within a block of dental putty, while pressing firmly to create a close fit around the teeth and gingiva. The putty was held in place until it hardened (~60s).

To enable mounting of the encased camera and laser diode, holes were drilled into the buccal and lingual sides of the mold such that a straight light path was created between the light source and the detector for maximum light throughput in a trans-illumination geometry. The camera and laser diode housings were inserted into the drilled holes and were held rigidly in place via friction. The total cost of each mold was less than $2, and required ~10 minutes to complete.

The encased camera and laser diode were wrapped with disposable Cover-All barrier film (Kerr TotalCare, Orange, CA) before use on each subject to prevent cross-contamination. Additionally, they were sanitized using sterile alcohol prep pads (Dynarex, Orangeburg, NY) between uses.

2.2.3.7 In vivo exposure time selection

To aid in the selection of an exposure time to be used during LSI that would maximize sensitivity to blood flow changes during the cardiac cycle, I used the setup described above to measure gingival blood flow while varying the NanEye exposure time from 2 to 23 ms (corresponding to exposure settings in Awaiba Viewer of 25 to 249 in 24 or 25 unit steps). Thirty seconds of data was collected at each exposure time with minimal perturbation introduced between measurements to minimize vasoconstriction or vasodilation mediated changes in blood flow during the measurement period. Temporal

speckle contrast was computed from each data set as described above and the average change in contrast between systole and diastole was computed. This metric was used to quantify the sensitivity of the imaging system to physiologically relevant changes in blood flow at various exposure times[88].

2.2.3.8 In vivo device validation

To ensure that I could detect physiological changes in perfusion, I measured the speckle contrast while artificially perturbing blood flow. I used the device to measure flow in the index finger, and performed an arterial occlusion using a pressure cuff. A 90s arterial occlusion was performed by inflating a pressure cuff to 220mmHg to stop blood flow to the finger, followed by a 90s recovery period.

I also measured baseline perfusion in three regions of the gingiva, moving progressively from the interdental papilla between the upper incisors to the marginal gingiva, to the attached gingiva to demonstrate changes in perfusion due to different gingival physiology.

2.2.3.9 In vivo device repeatability

To quantify the repeatability of the device to measure the same region each time the imaging system was inserted into the oral cavity, as well as to quantify the repeatability of the imaging system longitudinally, I acquired three measurements (three minutes each) on six subjects every day for five consecutive days. Between each measurement, I removed and reinserted the imaging device. Collected image sequences were used to compute temporal contrast within an ROI of 66x66 pixels corresponding to the interdental papilla above the upper incisors. I computed the average speckle contrast during each three-

minute data set, as well as the standard deviation of the contrast across the fifteen measurements collected throughout the week.

2.2.3.10 In vivo experimental measurements

I recruited 12 subjects at the Concorde Career College Dental Hygiene Clinic, and collected a set of three measurements for three minutes each at 30fps to ensure stability of the signal. Subject measurements were taken with an exposure time of 5ms. The average irradiance during patient measurements was 0.095W/cm^2 with a maximum of 0.24W/cm^2, which is less than the maximum permissible exposure for tissue[89] of 0.30W/cm^2. Before LSI data was collected, an examination was performed by a dentist to quantify each subject's bleeding on probing index for the marginal gingiva of the upper anterior teeth (6-11). I excluded three patients from the final study (n=2 had missing upper anterior teeth, n=1 had hardware malfunction during image collection) leaving nine subjects. The average temporal laser speckle contrast was calculated in a ROI corresponding to the interdental papilla for each measurement. I summed the bleeding on probing index for the upper anterior teeth to grade the overall gingival health of each subject. I computed the Spearman's rank correlation coefficient between the average temporal contrast value and the summed bleeding on probing index. I performed a hypothesis test on a linear fit to these data to test the significance of the slope.

2.2.4 Results

2.2.4.1 Device design

I built a device to acquire laser speckle images of the gingiva as shown in Figure 2.5. I collected a series of trans-illuminated images of the gingiva using a miniature camera (Fig 2.5.c) placed on the labial side of a custom-fit dental putty mold (Fig 2.5.a). I typically

collected images of the interdental papilla; however, I also measured perfusion in the attached and marginal gingiva (Fig 2.5.b). The speckle pattern is generated using a near-infrared laser diode (Fig 2.5.c) on the lingual surface of the mold, which has good depth penetration into perfused tissue[90]. The mold fits securely around the upper anterior teeth, which holds the camera and laser diode fixed relative to each other and in the same location every time the mold was inserted. I determined that an exposure time of 5ms maximized our temporal contrast sensitivity to physiological changes in flow due to the heartbeat, therefore this exposure time was chosen for all future measurements.

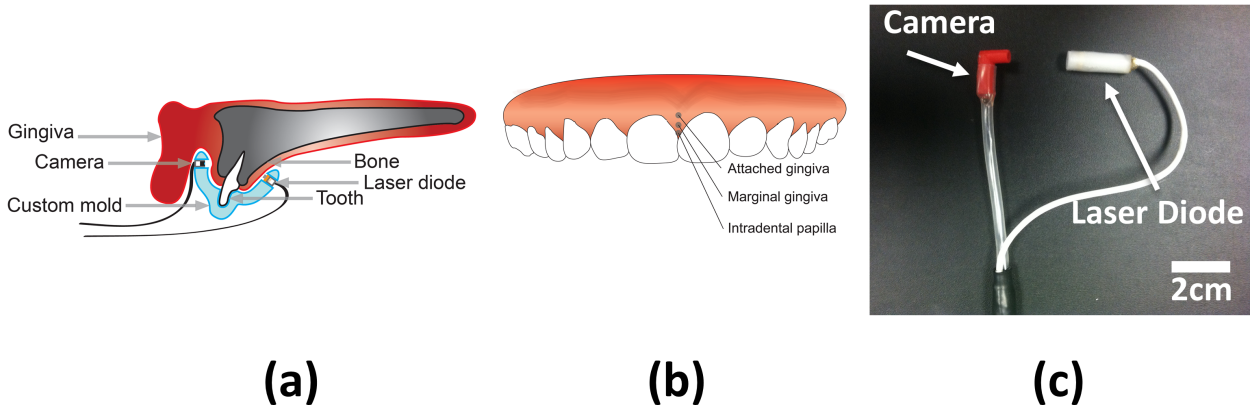

Figure 2.5: Design of miniature intraoral LSI device. (a) The NanEye camera and 785nm laser diode were placed in a custom-fit dental putty mold, which held them securely in place to acquire trans-illuminated images of the gingiva. (b) I primarily imaged the interdental papilla between the upper incisors. Images of the marginal and attached gingiva were also acquired to determine if the device was sensitive to spatial variations in gingival perfusion. Clinical assessments of bleeding on probing were acquired for the upper anterior teeth (incisors and canines, teeth 6-11). (c) The NanEye camera was housed in a 3D-printed case (red) and the laser diode mounted in a delrin case (white) that contained an aluminum heat-sink to ensure intensity stability.

2.2.4.2 Static in vitro device validation

To monitor the stability of the laser diode intensity, as well as the temporal contrast in images collected using the NanEye camera, I measured a non-flowing liquid phantom over three minutes. The CV of the intensity remained below 1% for intensities above ~20 counts. The CV of the temporal contrast was <1% at intensities between 20 and 140 counts.

2.2.4.3 Dynamic in vitro device validation

To ensure the miniature camera was capable of collecting data with sufficient dynamic range and spatial resolution, and with limited artifacts due to the built-in lens system, I compared *in vitro* flow phantom data collected with a research grade Chameleon3 CCD camera (Fig 2.6.a) to data collected with the NanEye camera (Fig 2.6.b). I measured the temporal contrast of flow in a glass microcapillary tube at speeds from 0.25-5.00mm/s (Fig 2.6.c). The image from the NanEye camera had lower resolution compared with the Chameleon3 (Fig 2.6.a vs. 2.6.b), which resulted in lower fidelity object boundaries and an overall grainer image. There was some barrel distortion present near the edges of the images taken with the NanEye camera, however this did not affect the device due to the fact that the camera is contained within a tube, which inherently reduces the available field of view to the center of the image (Fig 2.6.b).

I demonstrated that contrast decays exponentially with flow speed, as predicted by speckle theory[1] (Fig 2.6.c). The dynamic range for temporal contrast using the NanEye was ~0.08 over the flow speeds I tested and ~0.15 for the Chameleon3 (Fig 2.6.c). I observed a linear trend ($R^2 = 0.9992$) between contrast values at different flow speeds calculated from images taken with the NanEye versus the Chameleon3 (Fig 2.6.d). This demonstrated that even though the dynamic range was lower for the NanEye, it still maintained the same contrast response to flow speed as a research grade camera.

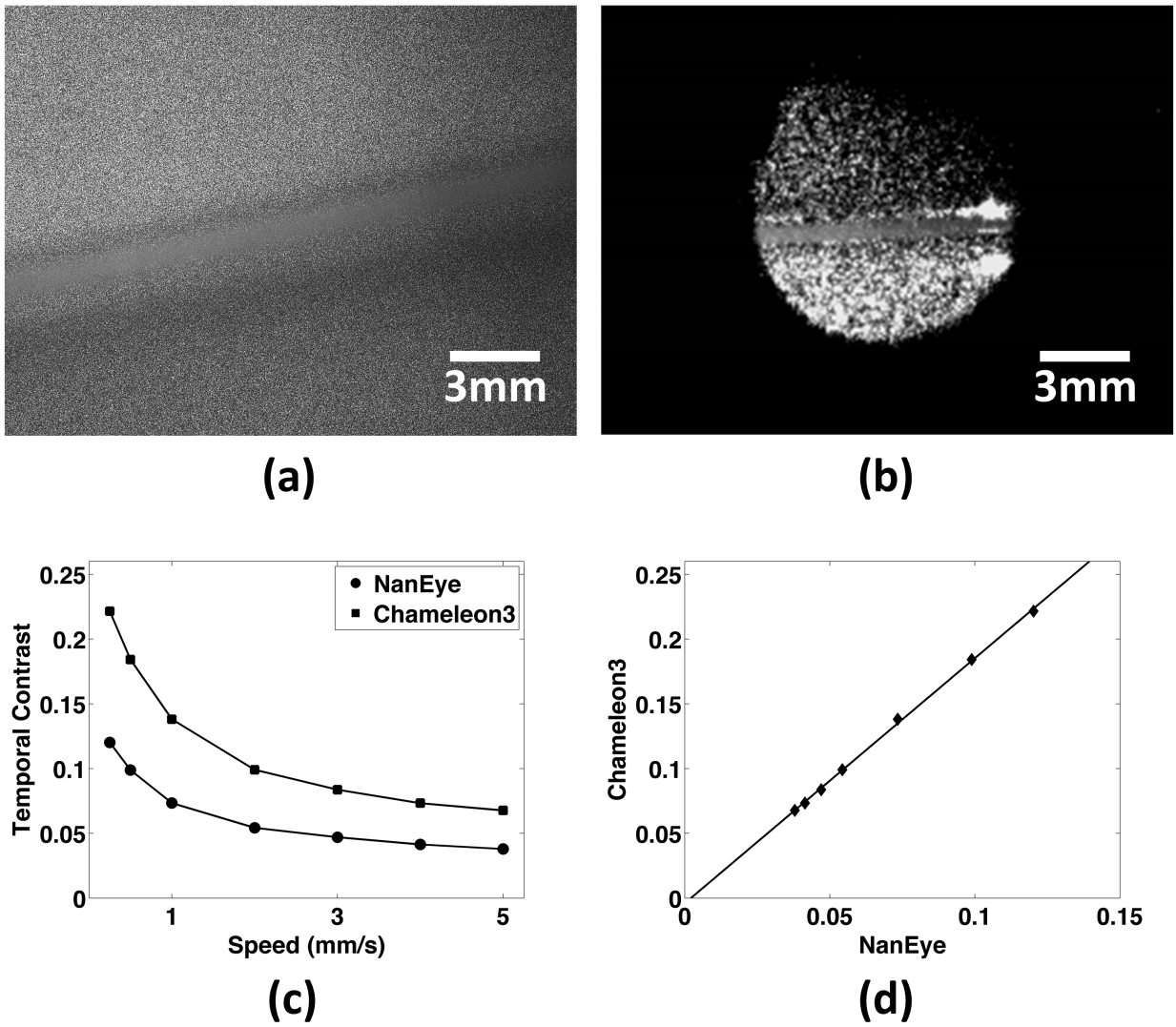

Figure 2.6: Dynamic *in vitro* device validation. (a) Sample raw speckle image of flow in a glass microchannel (blurred rectangular region) acquired with a research grade CCD camera (Chameleon3, Pt. Grey). (b) Sample raw speckle image of flow in a glass microchannel (blurred rectangular region) acquired with the NanEye camera. The field of view was limited because the camera was encased in a protective housing. (c) Temporal contrast measured simultaneously on flow at different speeds. The dynamic range of the Chameleon3 was greater than that of the NanEye (0.15 compared to 0.08). (d). Comparison of temporal contrast at different flow speeds for the Chameleon3 and NanEye cameras resulted in a linear relationship (R^2=0.9992), suggesting the ability of the NanEye to measure blood flow in a comparable manner to the Chameleon3.

To determine the range of intensities where the LSI system remained stable, I measured the temporal contrast as a function of intensity (Fig 2.7.a) in a non-moving liquid phantom. I observed inflection points in the contrast response at ~20 counts and ~140 counts. Therefore, I maintained the intensity within this range during *in vivo* clinical data collection.

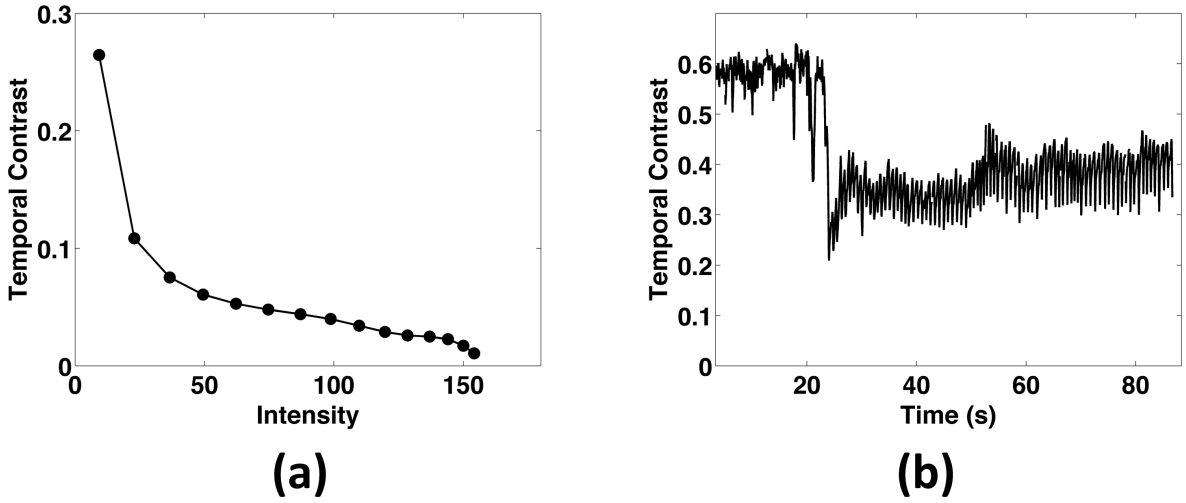

Figure 2.7: (a) I measured temporal contrast as a function of intensity to determine the range of stable contrast measurements. Due to the inflection points at ~20 and ~140 counts, I collected all further experimental data with intensities ranging between those values. The CV of the intensity and contrast data was <1% in this range. (b) Measurements of physiological changes in blood flow during an arterial occlusion. The flow was low (K = 0.57) until the occlusion was released at ~20s. A reactive hyperemia response occurred for ~5s and then flow stabilized to baseline (K=0.37).

2.2.4.4 In vivo device validation

To ensure the device could differentiate between induced changes in *in vivo* blood flow, I performed an arterial occlusion while collecting measurements in the index finger using the device (Fig 2.7.b). The occlusion was in place for the first ~20s of imaging, during which the average temporal contrast was 0.57. Once the occlusion was released (at ~20s), I observed a reactive hyperemia response for ~5s as flow rushed back into the digit causing

a marked decrease in contrast. The contrast then settled to a stable baseline of 0.37 for the remainder of the measurement as flow returned to baseline.

To determine the effects of spatial variations in sensor placement, I measured temporal speckle contrast in three locations of the gingiva between the upper incisors of a human subject: the interdental papilla, the marginal gingiva, and the attached gingiva (Fig 2.5.b). As I moved further away from the interdental papilla, the contrast decreased by 0.013 (Table 2.1).

Table 2.1: Speckle contrast in different spatial locations within the gingiva. Contrast decreased by 0.013 as the probe was moved from the interdental papilla to the attached gingiva.

Location	Temporal Contrast
Interdental Papilla	0.042
Marginal Gingiva	0.031
Attached Gingiva	0.029

2.2.4.5 In vivo device repeatability

To measure the stability of the system to obtain repeatable contrast values across multiple longitudinal measurements, I measured contrast in the interdental papilla region of the gingiva of six subjects over a period of five consecutive days. Additionally, I was concerned if significant physiological variations in flow occurred from day to day. I collected three data sets from each subject each day, and removed the device between each measurement to test the repeatability of the device between uses. I measured an average CV among the three daily measurements of 6.7%. To determine if daily variations in flow were a significant concern, I computed the standard deviation across the 15 total measurements for each subject (Table 2.2). One measurement was removed from Subjects 1 and 6, and two from Subject 5 due to the contrast value being a statistical outlier, which I postulate was due to a problem with the acquisition control software. I assumed that the

gingival health was constant in each of the six repeatability subjects over the course of the five daily measurements. I compared the measurements to the standard deviation of the 27 total measurements collected from subjects with varying degrees of gingival health (Concorde Clinic, $\sigma = 0.021$). There was a significant difference in the variance of the repeatability subjects compared to the variance of the group of clinical subjects with different stages of gingivitis ($p < 0.05$, Levene's test for equal variance) (Table 2.2). This analysis indicates that any variance that occurs from day to day due to the device or to physiological changes in flow are significantly less than the changes observed due to differences in gingival health and inflammation.

Table 2.2: Three data sets were acquired each day for five consecutive days from six subjects to determine the repeatability of the device; I assume the health of each subject remained constant across the week. The standard deviation of the 15 measurements for each subject is listed, as well as the standard deviation across all measurements taken from subjects with varying degrees of gingival health (Concorde Clinic). Levene's test for equal variance was applied to compare the variance of each subject to the collective data from Concorde Clinic, and the variances were significantly different ($p < 0.05$). This indicates that the variations in contrast due to daily changes in perfusion and instrument noise are significantly less than variations in flow due to different degrees of gingival health.

Subject	Standard Deviation (σ)	p-value of $\sigma_{repeatability}$ compared to $\sigma_{Concorde}$
Repeatability 1	0.008	0.008
Repeatability 2	0.007	0.004
Repeatability 3	0.014	0.048
Repeatability 4	0.011	0.015
Repeatability 5	0.008	0.009
Repeatability 6	0.011	0.021
Concorde Clinic	0.021	-

2.2.4.6 In vivo experimental measurements

Finally, to test the ability to correlate LSI data with gingival health, I took three three-minute measurements in nine subjects with mild to severe gingivitis. I computed a CV of less than 14% between the three measurements for each subject. The CV across all 27 clinical subject measurements was over 34%. I measured the Spearman correlation

between the sum of the bleeding on probing index across the frontal and lingual side of the upper anterior teeth and the measured temporal contrast value. I observed a decrease in contrast as the sum of the anterior bleeding on probing score increased (Fig 2.8), indicating an increase in flow with decreasing gingival health. The correlation had a Spearman coefficient (ρ) of -0.53 ($p<0.005$), and a linear hypothesis test indicated that the slope was significantly different from zero ($p<0.01$).

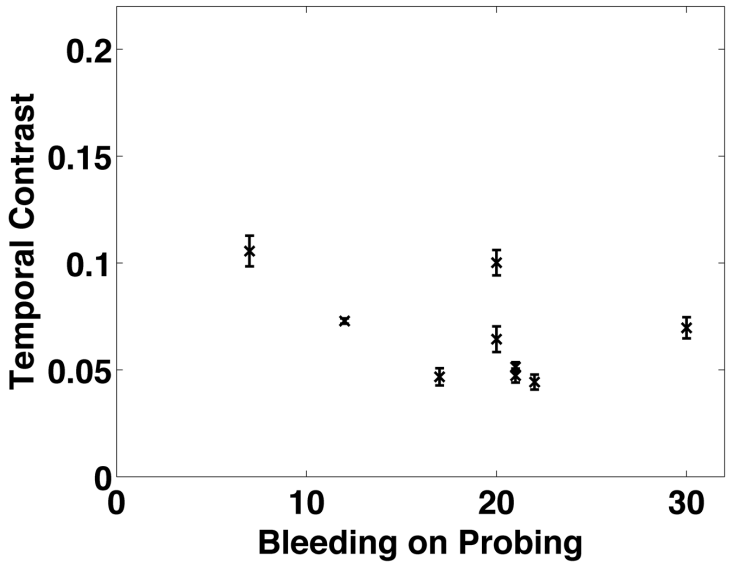

Figure 2.8: Three measurements were collected from nine subjects with varying degrees of gingival inflammation. The sum of the bleeding on probing scores (x-axis) for the anterior teeth was correlated to the measurements of temporal contrast (y-axis). I observed a significant increase in perfusion (decrease in contrast) with an increase in bleeding on probing (indicative of worse gingival health) ($\rho=-0.53$, $p<0.005$). The average temporal contrast with standard deviation is shown for each of the nine subjects.

2.2.5 Discussion

My experiments collectively demonstrate the feasibility and stability of a miniature LSI device designed for use in the mouth. I built a device that fit securely around a subject's teeth to hold a small camera and compact laser diode in place to trans-illuminate the gingiva (Fig 2.5). The impression mold held the imaging system securely in place, and

enabled repeated imaging of the same location within the gingiva. This was important to minimize motion artifacts, which hinder accurate clinical data collection in many LSI devices[66], as well as to ensure measurements were taken in the same location, which is important because blood flow in the oral cavity may have significant spatial variance due to physiology[91].

I computed temporal speckle contrast values to obtain an estimate of perfusion in the gingiva. I chose to use the temporal algorithm to compute speckle contrast rather than the spatial algorithm because the former has been shown to be more reliable when quantifying contrast in regions containing static scattering[6]. Since the detected light likely propagated through static scattering structures such as the roots of the teeth, or even bone, I chose to use the temporal algorithm to maximize our sensitivity to blood flow. This results in relatively low temporal contrast values (0.02-0.12) observed in *in vivo* gingiva (Table 2.1, Table 2.2, Fig 2.8), which is expected due to the high level of perfusion present in this tissue. We do not observe a significant correlation between speckle contrast computed with the spatial algorithm and bleeding on probing ($\rho = -0.19$, $p>0.35$), which supports the hypothesis that the temporal algorithm is required to reduce the effect of static scattering due to inter-patient physiological variability.

I performed several *in vitro* and *in vivo* experiments to test the stability and repeatability of the device. I monitored the stability of the laser diode intensity to ensure that fluctuations in intensity, as well as in temporal contrast, had a CV below 1%. These results indicate that the aluminum heat sink in the device was sufficient for thermal stabilization of the laser diode. I determined that the most stable contrast values were obtained when data were collected with intensity counts between 20 and 140 (Fig 2.7.a).

Additionally, I determined that 5ms was the optimal exposure time for the device to be sensitive to physiological changes in flow.

A comparison of the device and a laboratory grade LSI system demonstrated a linear relationship between contrast values from each system as a function of flow speed (Fig 2.6.d). I did observe a lower dynamic range with the miniature oral device (Fig 2.6.c), which is potentially due to the NanEye's comparatively smaller sensor dynamic range (72dB vs. 42dB) resulting from greater noise and reduced full well capacity.

I collected *in vivo* data that demonstrated the ability of the device to detect changes in perfusion. During an arterial occlusion, I detected a sharp increase in temporal speckle contrast (Fig 2.7.b), consistent with expectations of decreased flow during an occlusion. When the occlusion was released, I observed a characteristic decrease in contrast due to the reactive hyperemia response, before the flow returned to baseline. These data demonstrate that the imaging system was sensitive to induced physiological changes in perfusion.

I also observed a decrease in contrast as I changed the measurement location from the interdental papilla towards the marginal and attached gingiva (Table 2.1). I postulate that this is due to the corresponding increase in the thickness of the measured region, and hence an increase in the amount of perfusion, causing a decrease in contrast. This highlights the importance of maintaining a repeatable imaging location between measurements, which was facilitated with the mold design used in this study.

I performed *in vivo* measurements on six subjects to ensure that our device could obtain repeatable contrast values across multiple measurement sessions. The mold is capable of being repeatedly inserted and removed from the subject's mouth while

maintaining a similar imaging location for every measurement. Repeatability of imaging locations is critical for future longitudinal studies of gingival blood flow dynamics. My data demonstrate that the device can be removed and replaced while maintaining measurements of temporal contrast in the gingiva with an average CV of 6.7%. In comparison, the CV among measurements in multiple subjects with varying degrees of gingival inflammation is over 34%. Additionally, data collected longitudinally from six repeatability subjects showed significantly less variance ($p<0.05$) than the measurements collected from subjects in varying stages of gingival health (Table 2.2). This indicates that not only is the device capable of repeatedly measuring the same location in the gingiva, but that physiological changes in flow from day to day are less than the changes observed due to variations in gingival health. This result supports my hypothesis that LSI can be used as a diagnostic aid or a tool for the assessment of changes in gingival health over time.

Finally, I performed measurements in subjects that were evaluated for gingivitis symptoms. I acquired similar speckle contrast values in each of the three measurements collected per subject (CV <14%), which is consistent with the previous *in vivo* validation measurements. My data show that speckle contrast decreased as the bleeding on probing index for the upper anterior gingiva increased (Fig 2.8), which is indicative of more severe gingivitis. I postulate that the decrease in speckle contrast is due to an increase in blood flow, which may be due to increased inflammation in the gingiva, dilation of the microvasculature, or increased vascular density, all of which have been shown to increase perfusion[81].

In addition to gingivitis, there are other conditions that affect the oral mucosa. For example, LSI may be used to provide a quantitative assessment of oral mucositis, an

inflammatory condition causing painful ulcers in the mouth following chemotherapy and radiation treatments for cancer[92]. Furthermore, the question of assessing pulpal vitality by detecting blood flow in the pulpal chamber is still unresolved. The mouth-guard based device may provide a more stable method of collecting LSI data as compared to previous measurement systems[66], and for more specifically targeting locations on the tooth that correspond to the pulpal chamber to reduce contamination of the signal from gingival blood flow.

In conclusion, my *in vitro* and *in vivo* data collectively support my hypothesis that LSI can be used to quantitatively measure changes in perfusion associated with gingival health. With continued refinement and evaluation of this platform, I anticipate development of a simple method for objective diagnosis of periodontal disease and evaluation of treatment approaches for gingivitis and other oral microvascular diseases.

2.2.6 Acknowledgements

I would like to acknowledge support from the Arnold and Mabel Beckman Foundation, the National Institute of Health (R01 DE022831, R01 HD065536), the National Institute of Health Laser Microbeam and Medical Program (P41 EB015890), and the National Science Foundation BEST IGERT Program (DGE 1144901).

CHAPTER 3: Photothermal laser speckle imaging

3.1 Photothermal laser speckle imaging phenomena

This work was originally published in Optics Letters[31].

3.1.1 Abstract

The analysis of speckle contrast in a time-integrated speckle pattern enables visualization of superficial blood flow in exposed vasculature, a method called laser speckle imaging (LSI). With current methods, LSI does not enable visualization of subsurface or small vasculature, due to optical scattering by stationary structures. In this work I propose a new technique called photothermal LSI to improve visualization of blood vessels. A 595nm laser pulse was used to excite blood in both *in vitro* and *in vivo* samples. The high absorption coefficient of blood at this wavelength results in efficient conversion of optical energy to thermal energy, resulting in an increase in the local temperature and hence increased scatterer motion, and thus a transient decrease in speckle contrast. As a result, I found that photothermal LSI was able to visualize blood vessels that were hidden when imaged with a conventional LSI system.

3.1.2 Results and Discussion

In 1981, Fercher and Briers[4] first proposed the use of time-integrated laser speckle patterns to map blood flow in the retina. Dunn el al[3] demonstrated that this method enabled blood-flow mapping of the rodent brain, which led to a rapid increase in the use of laser speckle imaging (LSI) for a wide variety of biological and biomedical applications.

Typically, researchers use LSI to map and quantify relative changes in blood flow in response to an intervention. A related use of LSI is simply to enable visualization of perfused microvasculature[15]. However, scattering layers such as the skull or epidermis

obscure the microvascular architecture. A variety of post-processing methods were proposed to reduce this effect, including temporal processing[5] and motion contrast algorithms[16].

Here I propose a new method, which I call photothermal LSI, to noninvasively image subsurface blood vessels using selective optical excitation of absorbers within the vessels. Photothermal LSI is based on two techniques described previously in the literature: magnetomotive LSI[17] and pulsed photothermal radiometry (PPTR)[26,93]. Magnetomotive LSI involves the use of an alternating magnetic field to induce movement of superparamagnetic iron oxide nanoparticles that are introduced into the vasculature. The additional motion of the particles aligning back and forth with the alternating magnetic field causes a distinct increase in motion that the LSI method detects as a decrease in local speckle contrast.

PPTR involves application of a short pulse of laser light to the surface of a sample, resulting in selective absorption and subsequent heating of specific optical absorbers within the medium. Mid-infrared detectors are typically used to collect infrared emission at the sample surface that varies due to heat diffusion from the heated absorbers. Based on analysis of the transient change in infrared emission, specific parameters can be estimated, including tissue absorption coefficients[93] and depth of vasculature[26].

Photothermal LSI involves use of a short pulse of laser light (similar to PPTR) to heat subsurface blood vessels, which I propose leads to a transient decrease in speckle contrast due to photothermally-induced changes to intravascular optical scatterers. This is similar to magnetomotive LSI; however, I selectively target absorption by the hemoglobin molecules contained within the red blood cells, rather than modulate the movement of an exogenous particle. To achieve selective optical excitation, I induce transient heating of the

blood with a 595nm laser pulse. In this Chapter, I present data collected with *in vitro* and *in vivo* experimental setups, to demonstrate the ability of photothermal LSI to improve visualization of subsurface microvasculature via a targeted increase in the difference in contrast between the blood vessels and surrounding tissue.

For the *in vitro* experiments, I used two samples: a 1cm wide cuvette filled with porcine blood (Fig 3.1.a), to demonstrate the concept, and a microchannel-based skin phantom (Fig 3.2.a). To create the phantom, a slide with microchannels (thinXXSMicrotechnology AG, Germany) was placed above a silicone block containing TiO_2 powder to mimic the scattering properties of soft biological tissues. A second silicone layer (400μm thick), with TiO_2 powder to simulate epidermal scattering properties, was placed above the microchannel. An infusion pump was used to inject porcine blood (Sierra for Medical Science, Whittier, CA) into the microchannel, which had an inner diameter of 320μm. Tygon tubing was used to deliver the blood from the syringe pump to the channel inlet. The infusion pump was set to achieve a flow speed of 4 mm/s, representative of flow in arterioles and venules[94].

To image the dynamics of particle motion, I used a conventional LSI system consisting of a 632.8nm HeNe laser that uniformly illuminated either the blood-filled cuvette or the skin phantom (Figs 3.1.a and 3.2.a). The radiant exposure of this imaging laser is ~11mJ/s, or less than .0001% of the radiant exposure of the interrogating pulse, making its contribution to any photothermal changes in the sample negligible. All speckle images were acquired with a HotShot 1280 CCD camera (NAC Image Technology, Simi Valley, CA) equipped with a macro lens. To mitigate specular reflectance from the samples,

a polarizing filter was placed in front of the camera lens and perpendicularly oriented to the polarization of the incident light.

I used pulsed 595nm laser light (Vbeam, Candela, MA) to optically excite the samples. I selected 595nm due to the strong absorption of this wavelength by hemoglobin. For our experiments, I used a pulse duration of 3ms and radiant exposure of 4 J/cm^2, which is similar to radiant exposures used previously in PPTR studies[26]. I used a laser-linepass filter (ThorLabs, Newton, NJ) centered at 632.8nm (70% transmission) to prevent contamination of images by remitted 595nm laser light (less than .01% transmission).

I collected raw speckle images at 50 frames per second with an exposure time of 14ms, before, during, and after application of the pump 595nm light. I used the standard sliding-window algorithm (7x7 pixel dimension) to convert each raw speckle image to a speckle contrast image[95]. From each speckle contrast image, I calculated the mean speckle contrast within a 16x66 pixel region of interest. I then calculated maps of speckle flow index (SFI) using a simplified speckle imaging equation[95].

Upon photothermal excitation of a blood-filled cuvette, (Fig 3.1.a), I observed a transient reduction of speckle contrast (Fig 3.1.b). The contrast decreased abruptly by ~60%, suggesting an increase in motion of scattering particles within the blood. After ~0.6s, the contrast returned nearly to its baseline value, presumably due to a decrease in temperature of the excited sample.

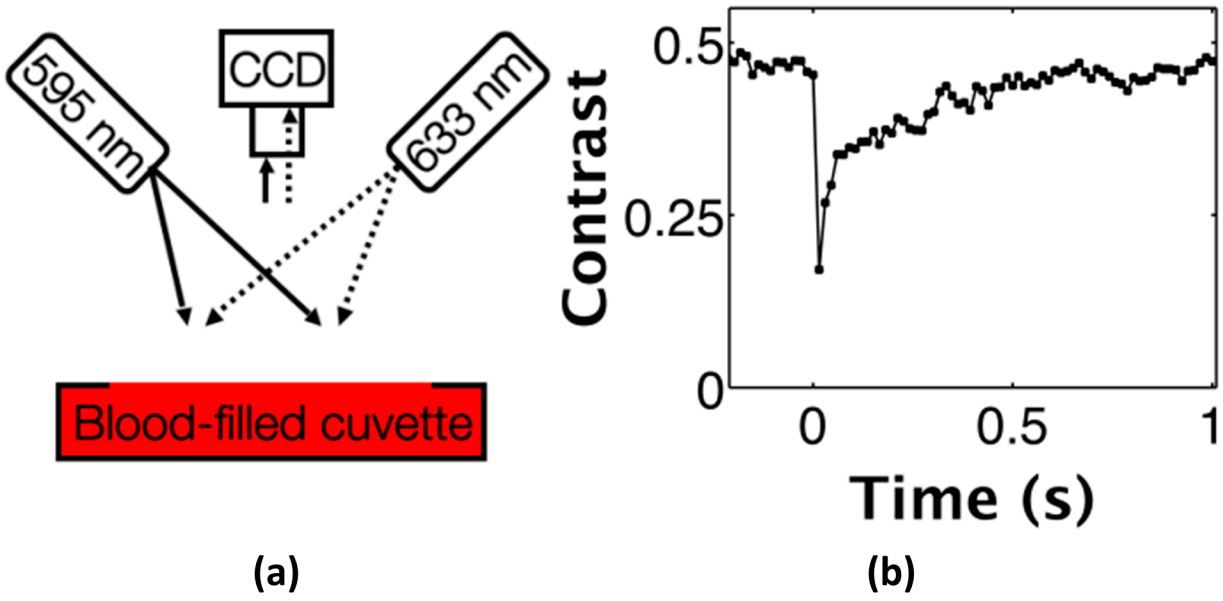

Figure 3.1: *In vitro* photothermal LSI of blood in a cuvette. (a) Photothermal LSI set-up with 633nm imaging laser light and 595nm pulsed dye laser to excite the blood. Images are captured with a cooled CCD camera with a laser-line bandpass filter to block extraneous light. (b) Speckle contrast versus time plot illustrates distinct drop in contrast corresponding to the photothermal excitation pulse at time 0s. The 60% decrease in contrast returns to baseline over about 0.6s as the blood returns to room temperature.

Similarly, with photothermal excitation of the microchannel-based skin phantom (Fig 3.2.a), I observed a transient reduction in speckle contrast (Fig 3.2.b). To simulate subsurface blood flow, I placed a skin-simulating phantom of 400μm thickness on top of the microchannel. In this specific case, to mimic *in vivo* conditions, the blood continuously flowed through the microchannel; therefore, the associated speckle contrast values at all time points were lower than those for the blood-filled cuvette.

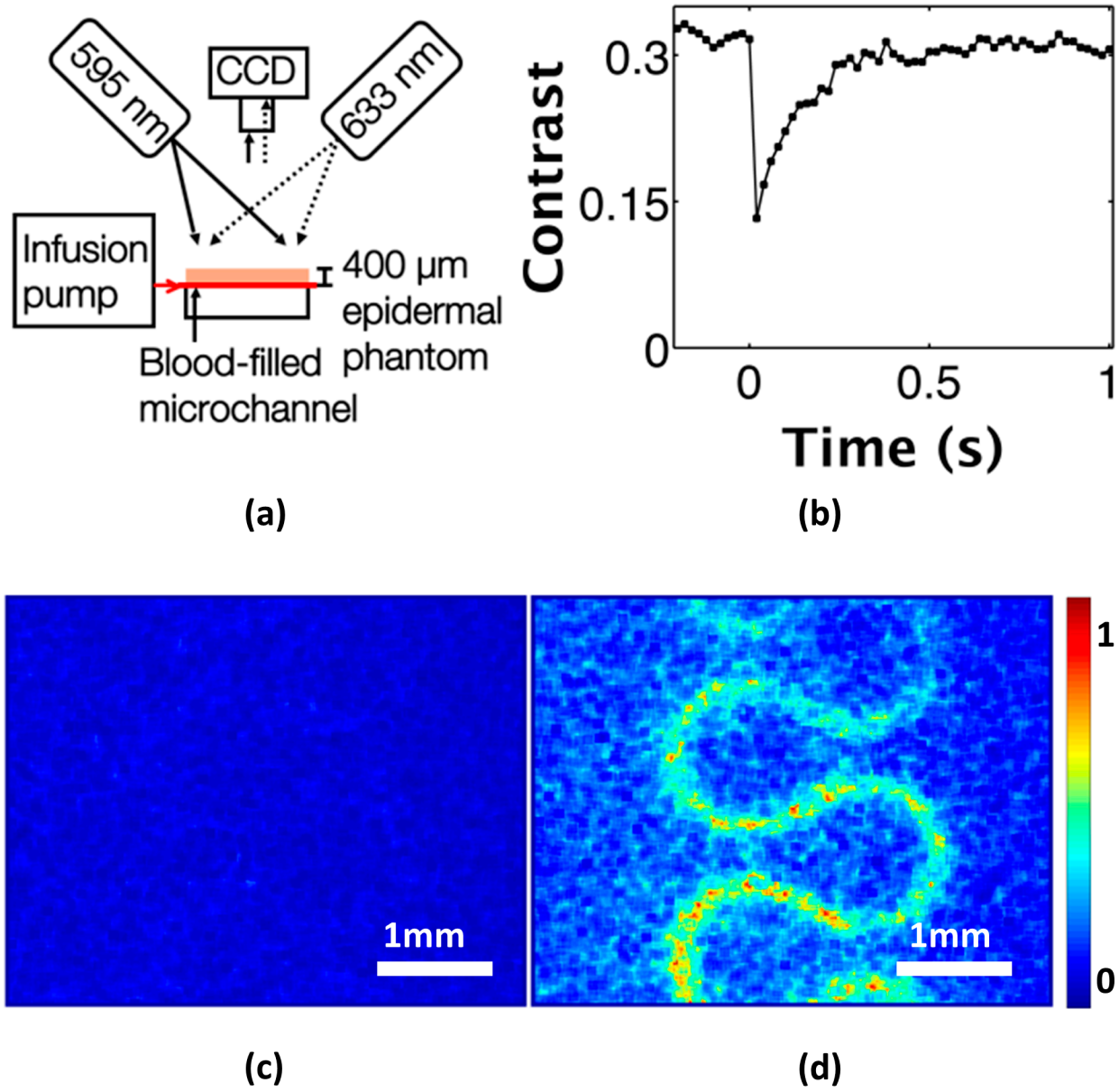

Figure 3.2: *In vitro* photothermal LSI of blood flowing through a microchannel. (a) Photothermal LSI set-up with blood infused into the system at 4mm/s and a 400μm epidermal phantom placed above the microchannel. (b) Speckle contrast versus time in a region of interest above the channel shows a 60% decrease in flow occurring after the excitation pulse at time 0s, and returning to baseline over the next ~0.4s. (c) Normalized speckle flow index (SFI) in microchannel before the photothermal excitation. (d) SFI image after the excitation pulse shows the blood flow in the channel clearly visible beneath the skin-simulating phantom.

I observed a ~60% decrease in the contrast following photothermal excitation, and a return to baseline contrast after ~0.4 s. Prior to photothermal excitation, it was not possible to visualize the microchannel through the overlying epidermal phantom (Fig 3.2.c). Immediately after photothermal excitation, the microchannel structure was clearly evident (Fig 3.2.d). I postulate that this is due to an increase in the temperature of the blood, creating more movement of scattering particles present in the blood in the microchannel. Figures 3.2.c and 3.2.d show SFI dynamics during photothermal excitation of the microchannel. In summary, the data shown in Figure 3.2 collectively supports the hypothesis that photothermal excitation of flowing blood in an *in vitro* system induces a brief decrease in speckle contrast that is observed even when the flowing blood is below a surface layer.

I next investigated how photothermal LSI performs with an *in vivo* animal model. To enable direct comparison of the imaged microvasculature with the actual microvascular architecture, I used a mouse dorsal window chamber model[14] as the test substrate (Fig 3.3.a). Briefly, the window chamber is a surgical preparation in which one full thickness of skin is suspended between titanium frames. A microvascular network is readily visible from the subdermal side of the chamber; the epidermis of the intact skin thickness is visible on the other side.

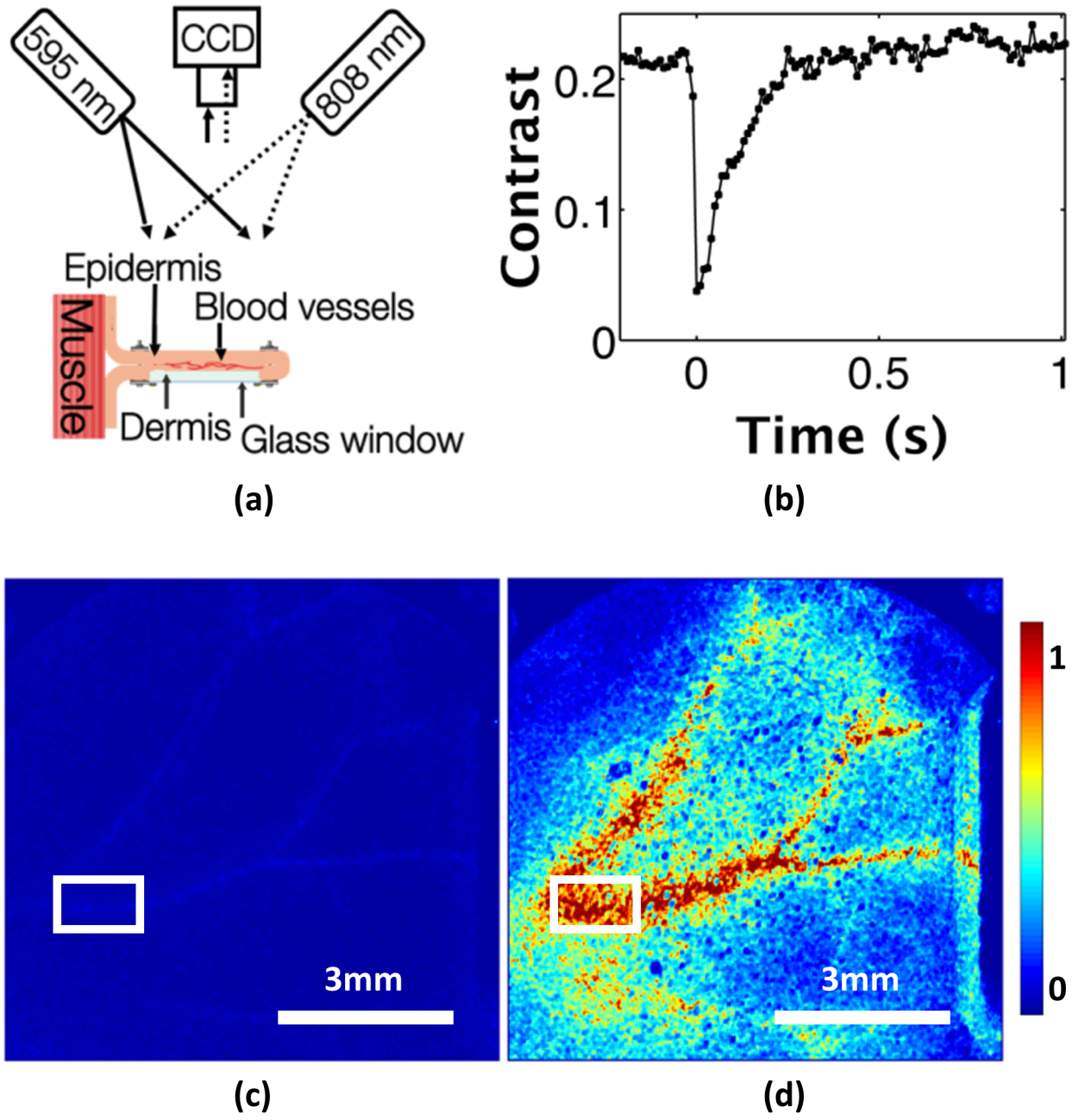

Figure 3.3: *In vivo* photothermal LSI in a mouse dorsal window chamber model. (a) Imaging set-up of the epi-illuminated reverse side of the window chamber. 808nm laser light is used to illuminate the epidermis for imaging, and an 800nm longpass filter is placed on the CCD camera to block stray 595nm excitation light. (b) Speckle contrast versus time in the region of interest highlighted in (c) and (d). The contrast drops by 80% when the excitation pulse is fired at time 0s, and quickly returns to baseline over ~0.3s. (c) Normalized SFI image before the excitation pulse. (d) SFI image after the photothermal excitation shows increased motion in the vessels. The perivascular increase in SFI is probably due to smaller vessels and capillaries that cannot be resolved with our current imaging system.

For LSI, I achieved wide-field coherent illumination of the epidermal side of the window chamber with the use of an 808nm laser diode (Ondax, Monrovia, CA) and engineered diffuser. To achieve photothermal excitation, I used the same pulsed-dye laser settings as in the *in vitro* experiments. I collected raw speckle images at 100fps with a 9ms exposure time. I used a longpass optical filter (ThorLabs, Newton, NJ) with an 800nm wavelength cutoff to block stray light associated with the excitation pulse. The filter allows for 85% transmission of 808nm light, and completely blocks 595nm light ($\sim 10^{-6}$ % transmission). I computed speckle contrast images using the spatial speckle-imaging algorithm with a 7x7 structuring element. From each contrast image, I selected a 16x66 pixel region of interest within one of the larger vessels (denoted by the rectangular region in Figs 3.3.c and 3.3.d).

Following the photothermal excitation, the speckle contrast decreased by ~80% (Fig 3.3.b). After ~0.3s, the speckle contrast in the region of interest returned to its baseline value, presumably due to a mix of heat diffusion from the irradiated site and advection via blood flow. From direct inspection of the SFI maps, the increase in visualization of the vasculature is apparent (Figs 3.3.c and 3.3.d). From a direct comparison of the SFI images from the *in vitro* (Fig 3.2.d) and *in vivo* (Fig 3.3.d) images, I observed *in vivo* a larger perivascular increase in SFI that is more diffuse in appearance. I hypothesize that this increase is due to a similar photothermal effect in blood vessels that are too small to resolve with the current experimental setup. This resolution issue can be overcome with a proper choice of higher-magnification camera optics.

Photothermal LSI relies on the concept of pulsed excitation of targeted absorbers, in my case red blood cells, to enhance the contrast of vasculature below a static scattering

layer. The exact mechanism for this change in contrast is currently unknown. Using the equation[96] $\Delta T = H \mu_a / \rho c$ where H is the radiant exposure ($4 J/cm^2$), μ_a is the absorption coefficient of blood at 595nm ($36 cm^{-1}$)[97], ρ is the density of whole blood ($1050 kg/m^3$) [14], and c is the mass specific heat capacity (3617J/kgC)[98], I calculated the estimated peak rise in temperature of the blood due to absorption at 595nm to be ~38°C, assuming there is no convective or diffusive losses during the pulse. I hypothesize that the increase in SFI is associated with rapid diffusion of this heat from the hemoglobin in red blood cells to nearby plasma proteins. I speculate that the change in motion due to this change in temperature may be caused by thermal expansion, changes in viscosity, or increases in diffusive motion, but further research will be needed to determine the mechanism (see Chapter 3.2). Future experiments will be also be performed to determine the lowest possible radiant exposure that will still produce this effect, in order to limit the potential for vascular damage during *in vivo* experiments. I also observe a similar transient change in speckle contrast when photothermal LSI is applied to a solution of India Ink and Intralipid (data not shown), demonstrating that this phenomenon is not only associated with whole blood.

In conclusion, photothermal LSI involves a transient, nondestructive increase in temperature in the vasculature, resulting in a decrease in speckle contrast and hence an increase in SFI. I propose that this method may enable improved three-dimensional localization of sources of speckle contrast – with accurate knowledge of the microvascular structure and local optical properties, researchers can use advanced tomography methods[44] to better define the speckle correlation time associated with subsurface blood vessels.

3.1.3 Acknowledgements

This research was funded in part by CONACYT (CB-2010-156876-F), the Arnold and Mabel Beckman Foundation, the Air Force Office of Scientific Research (FA9550-14-1-0034), the National Institute of Health (R01 DE022831, R01 HD065536), the National Institute of Health Laser Microbeam and Medical Program (P41 EB015890) and the NSF BEST IGERT program (DGE-1144901). I would also like to thank Chelsea Pittman (UC-Irvine) for performing the animal surgeries, and Andrew Weatherbee (University of Toronto), Dr. Boris Majaron (Institut Jožef Stefan, Slovenia), and Dr. Enrico Gratton (UC-Irvine) for insightful discussions into potential mechanisms related to photothermal LSI.

3.2 Laser speckle imaging based on photothermally driven convection

This work was originally published in The Journal of Biomedical Optics[35].

3.2.1 Abstract

Laser speckle imaging (LSI) is an interferometric technique that provides information about the relative speed of moving scatterers in a sample. Photothermal LSI overcomes limitations in depth resolution faced by conventional LSI by incorporating an excitation pulse to target absorption by hemoglobin within the vascular network. Here I present results from experiments designed to determine the mechanism by which photothermal LSI decreases speckle contrast. I measured the impact of mechanical properties on speckle contrast, as well as the spatiotemporal temperature dynamics and bulk convective motion occurring during photothermal LSI. My collective data strongly support the hypothesis that photothermal LSI achieves a transient reduction in speckle contrast due to bulk motion associated with thermally driven convection. The ability of photothermal LSI to image structures below a scattering medium may have important preclinical and clinical applications.

3.2.2 Introduction

Laser speckle imaging (LSI) is an interferometric technique that provides information about the motion of optical scatterers in a sample[4,1,50,14,3,5,99,100,9]. Fercher and Briers first applied LSI to visualize blood vessels in the retina[4]. Researchers have since reported on the use of LSI to map blood flow in many organs, including the brain[3,5], skin[99,100,10], and kidneys[9].

Conventional LSI has limited ability to quantify blood flow and resolve vasculature below a static scattering layer such as the epidermis or skull. Speckle contrast values

measured with LSI are associated with contributions from photons interacting with both static and dynamic scatterers[1]. Contributions from overlying static scatterers to the detected speckle pattern reduce the dynamic range of LSI and the overall visibility of subsurface microvasculature[19,6].

To overcome this limitation, I previously reported on the method of photothermal LSI[31]. With the application of a 3ms pulse of 595nm laser light, I observed a transient increase in the visibility of a subsurface microchannel containing flowing blood and of subsurface blood vessels in a mouse dorsal window chamber model. In Chapter 3.1, I postulated that selective photothermal excitation of hemoglobin molecules in the red blood cells resulted in an increase in motion of scattering particles within the vessels, leading to a simultaneous transient reduction in speckle contrast and hence increased visibility of subsurface microvasculature. This was based in part on published reports of photothermal optical coherence tomography[101], photoacoustic imaging[102], pulsed photothermal radiometry[26], and photothermal spectroscopy[103].

Here I describe experiments designed to identify the primary mechanism by which photothermal LSI decreases speckle contrast. I proposed the following three hypotheses:

1. A thermally induced pressure wave, similar to the photoacoustic effect, induces a bulk increase in motion throughout the sample.
2. An increase in temperature induces local effects such as changes in optical properties, viscosity of blood, Brownian motion, protein denaturation, and formation of methemoglobin[33,34].

3. Thermally-driven convection, a bulk movement of the liquid due to temperature gradients generated by the photothermal excitation, results in motion of the irradiated medium.

For hypothesis 1, I compared the photothermal excitation pulse duration τ_p (3ms) with the characteristic stress relaxation time of the sample τ_s. For efficient pressure-wave generation to occur, τ_p should be significantly shorter than $\tau_s = \delta/c_s$, where δ is the absorption length and c_s is the speed of sound in the medium[32]. For blood with 100% oxygen saturation, $\delta \sim 0.03$mm at 595nm excitation[97] and $c_s = 1.48 \times 10^6$mm/s[98], resulting in τ_s of 20ns. Hence, due to $\tau_p >> \tau_s$, I rejected hypothesis 1 as a primary mechanism. In this work, I present results from experiments designed to test hypotheses 2 and 3.

3.2.3 Materials and Methods

3.2.3.1 Liquid and solid phantoms

My liquid phantom consisted of 0.8mL of rabbit whole blood (~18°C) placed in a 35mm diameter petri dish, resulting in a layer thickness of 0.83mm. I also used a solid silicone phantom (35mm diameter, 10mm thick) fabricated using a polydimethylsiloxane (PDMS) base, with TiO_2 powder added to provide scattering and India ink to provide absorption[74].

3.2.3.2 Photothermal LSI setup and data analysis

My LSI setup (Fig 3.4.a) consisted of a HotShot 1280 CCD camera (NAC Image Technology, Simi Valley, CA) fitted with a macro lens. I used an exposure time of 9ms and a frame rate of 100fps. The speckle imaging laser was a diffused, long-coherence (~6m), 808nm laser diode (Ondax, Monrovia, CA), and the photothermal excitation laser was a

595nm pulsed dye laser (Vbeam, Candela, Wayland, MA) emitting a 3ms pulse (10mm diameter) at a radiant exposure of 4J/cm^2.

To study speckle contrast dynamics outside the directly irradiated spot, I increased the imaging field of view to extend laterally 12.5mm beyond the spot. I collected image sequences spanning the time before, during, and after the excitation pulse. I converted each raw speckle image to a spatial speckle contrast image using a conventional 7x7 sliding window algorithm[1]. I calculated the average speckle contrast of each image in a region of interest (ROI) selected within the directly irradiated spot (black) and ~10mm away from the edge of the irradiated spot (red) (Fig 3.5.a).

3.2.3.3 Infrared thermal imaging

To study heat diffusion dynamics, I used a mid-infrared focal plane array (FLIR Systems, Wilsonville, OR) to collect images of the whole blood phantom described above, at 271fps and with a 0.8ms exposure time per frame (Fig 3.4.b). I collected images over a period of 5s during photothermal excitation and used a blackbody source (OMEGA Engineering, Stamford, CT) to convert the infrared emission images to calibrated radiometric temperature maps.

3.2.3.4 Particle image velocimetry

To study convection dynamics, I distributed particles of TiO_2 powder on the surface of a layer of whole blood contained in a Petri dish. I collected high-speed (800fps) brightfield images of the entire blood sample (Fig 3.4.c, 3.7.a) over a period of 87.5ms during photothermal excitation. I used particle image velocimetry (PIV) methodology[104] to map vectors associated with the motion of the TiO_2 particles and processed the data using MatPIV software[104] developed in MATLAB (The Mathworks, Natick, MA).

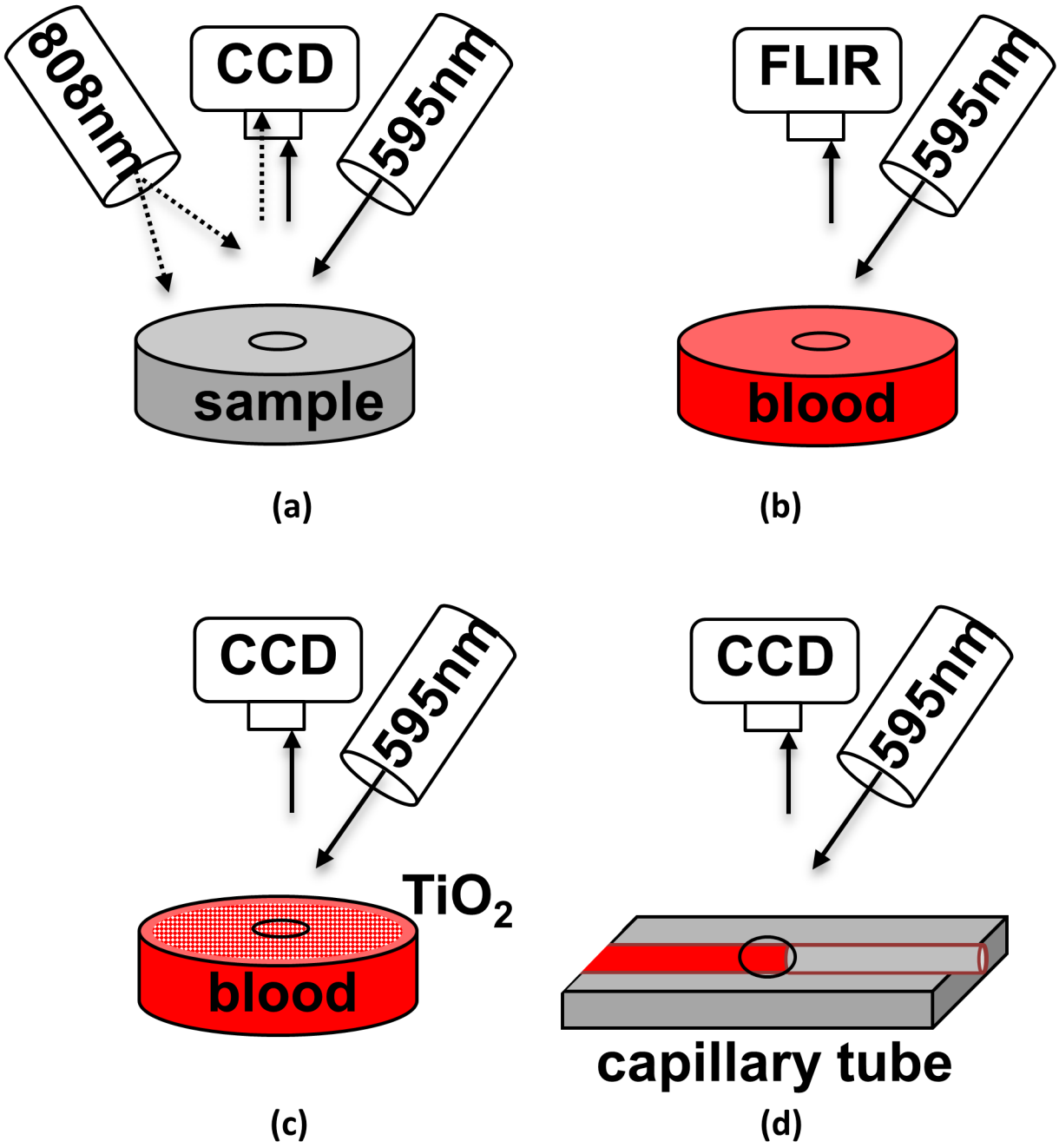

Figure 3.4: (a) Photothermal LSI setup. I performed laser speckle imaging on blood and solid silicone phantoms with a CCD camera and an 808nm laser. I used a 595nm pulsed laser to excite the 10mm region indicated at the center of each sample. (b) A mid-infrared focal plane array (FLIR) was used to detect infrared emission generated in blood as a result of a 595nm photothermal excitation pulse. (c) A CCD camera was used to acquire high-speed images of the radial movement of TiO_2 particles on the surface of a blood sample during the 595nm photothermal excitation pulse. (d) A CCD camera was used to visualize the expansion of blood in a microcapillary tube upon irradiation by the 595nm pulsed laser.

3.2.3.5 Volume expansion in a capillary tube

I infused whole blood into a 650μm diameter glass microchannel embedded at the surface of a scattering PDMS phantom (reduced scattering coefficient $\mu_s' \sim 1mm^{-1}$) (Fig 3.4.d). I collected both raw speckle images and brightfield images of the phantom during photothermal excitation. I calculated speckle contrast versus time in three regions of interest within the microchannel (Fig 3.7.c).

3.2.4 Results and Discussion

3.2.4.1 Photothermal LSI of liquid and solid phantoms

To assess the degree of correlation between local temperature and local speckle contrast, I measured speckle contrast during photothermal LSI in both the region directly irradiated by the pulsed laser and in a surrounding non-irradiated region ~10mm away (Figs 3.4.a, 3.5). Figure 3.5.a shows speckle contrast versus time, with photothermal excitation beginning at time = 0s. The contrast in each ROI was the same before the pulse. Immediately after the onset of pulsed laser excitation, the contrast values in both ROIs decreased simultaneously, suggesting a similar change in motion occurring throughout the entire sample, not just in the irradiated spot. I did not observe bubble formation or cavitation in the blood at this radiant exposure.

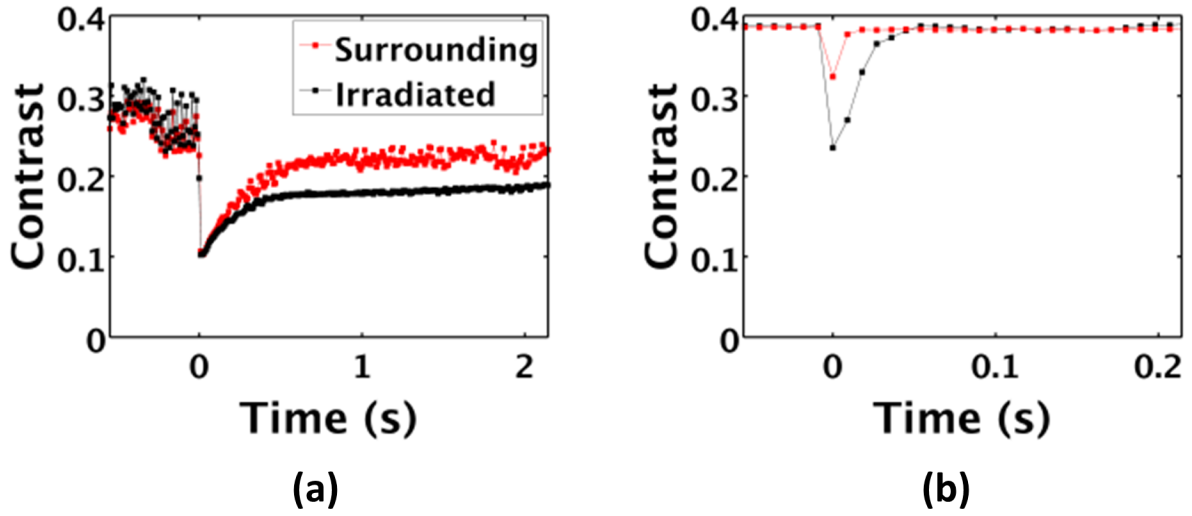

Figure 3.5: Photothermal excitation induces changes in speckle contrast in both the directly irradiated and the surrounding regions of a sample. The dynamics of speckle contrast may depend on the mechanical properties of the sample. (a) Immediately following excitation of a 0.83mm thick layer of blood with the pulsed dye laser, speckle contrast within and 10mm away from the laser spot decreased, suggesting that photothermal excitation causes effects throughout the entire sample. (b) Speckle contrast dynamics during the 0.2s immediately following photothermal excitation of a solid tissue-simulating phantom, contrast decreased and recovered ~10x more quickly than the irradiated blood sample in (a).

I performed a similar experiment on a solid silicone phantom to determine how the mechanical properties of the sample affect the photothermal LSI response. When the excitation pulse was applied to the solid phantom, the contrast decreased immediately and simultaneously in both ROIs (Fig 3.5.b), similar to my observations with photothermal excitation of blood (Fig 3.5.a). However, the contrast in the surrounding region only decreased to ~40% of the change measured in the directly irradiated spot. Due to the higher stiffness of the silicone, the contrast throughout the solid phantom returned to its baseline value within ~50ms, which is ten times faster than the associated recovery time for blood (Fig 3.5.a).

Collectively, these data (Fig 3.5) suggest that photothermal excitation induces motion throughout the entire sample, and not just in the directly irradiated spot; and that

the dynamics of this motion are affected by the mechanical properties of the sample (i.e.: compare Figs 3.5.a and 3.5.b).

3.2.4.2 Thermal response to photothermal excitation

I next measured the spatiotemporal temperature dynamics in response to photothermal excitation of blood (Figs 3.4.b, 3.6). With photothermal excitation (beginning at time = 0s in Fig 3.6.a), I observed an instantaneous increase in radiometric temperature of ~50°C in the directly irradiated spot. The temperature rise caused by the excitation pulse was localized to the directly irradiated region (Fig 3.6.b). Following the rapid increase in radiometric temperature, I observed a relatively slow decrease towards room temperature.

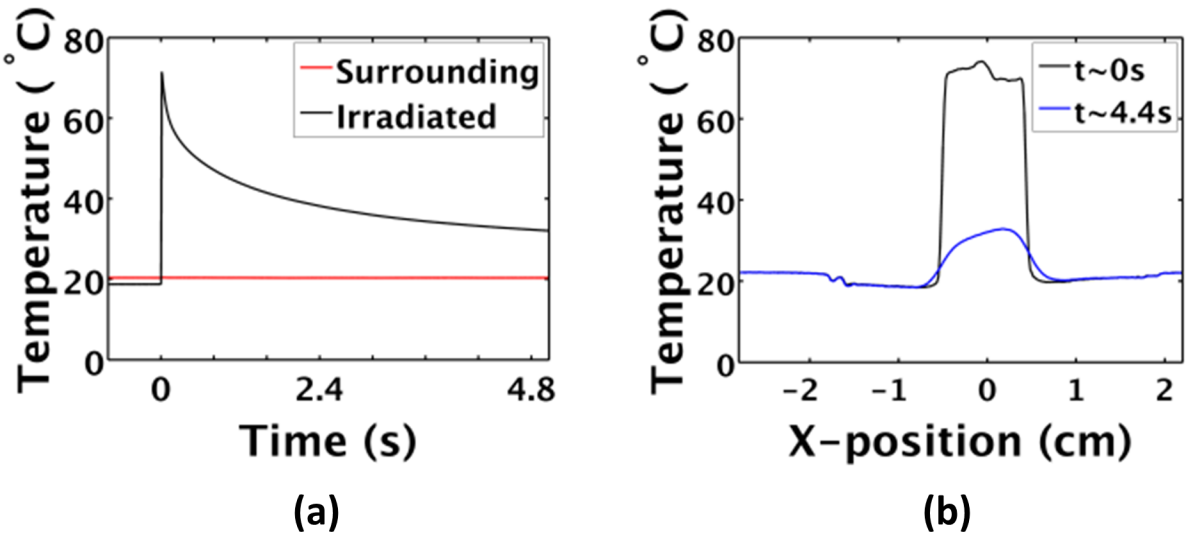

Figure 3.6: Photothermal excitation induces a change in temperature that is localized to the directly irradiated region. (a) With pulsed dye laser excitation of a layer of blood, the radiometric temperature increased ~50°C, followed by a relatively slow decay over a period of seconds. Outside the directly excited region, the temperature did not appreciably change. (b) Line profile of radiometric temperature immediately following the excitation pulse (black), and ~4.4s following the pulse (blue). The temperature rise caused by the excitation pulse is localized to the irradiated region and remained laterally confined to the diameter of the laser pulse throughout the measurement period (~4.4s).

After 4.4s, the peak temperature decreased by ~78%, but the elevated temperature remained confined primarily to the directly irradiated spot. The temperature in the region surrounding this spot changed minimally during the 5s imaging duration (Fig 3.6.b). These data demonstrate that the temperature increased appreciably only in the directly irradiated site.

My data demonstrate that photothermal excitation of whole blood induces changes in speckle contrast throughout the entire sample that recover to near-baseline values in <1s (Fig 3.5), whereas temperature changes over the same period of time are restricted only to the directly irradiated spot (Fig 3.6). These results strongly suggest that local changes alone cannot explain the relatively widespread decrease in speckle contrast observed with photothermal LSI. Hence, based on my findings, I rejected hypothesis 2 as a primary mechanism.

3.2.4.3 Thermally driven convective motion (volume expansion)

I next used suspended TiO_2 particles (Figs 3.4.c, 3.7.a, 3.7.b) to test hypothesis 3: thermally driven convection induced by photothermal excitation leads to bulk motion of blood away from the directly irradiated spot, causing an increase in motion throughout the entire sample. Convective motion is a bulk flow of fluid due to both diffusive and advective transport. In my experiments, I believe the driving force is the temperature difference between the irradiated region and the surroundings. In particular, the Marangoni effect causes convective motion of liquids due to gradients in surface tension[105]. The surface tension of the heated blood is lower than the surroundings[106], providing a driving force for the liquid to move outward from the irradiated region. I imaged over an 87.5ms period during photothermal excitation. Immediately following the excitation pulse, I observed a

rapid bulk motion of the particles away from the irradiated spot throughout the entire imaging field of view (Fig 3.7.a).

I used particle image velocimetry (PIV) concepts[104] to map vectors associated with the motion of the TiO_2 particles between the initial frame and the frame in which the particles are in their final displaced position. The map of the velocity field of the particles (Fig 3.7.b) illustrates the bulk motion of the TiO_2 particles away from the center of the directly irradiated spot.

To determine whether this bulk motion also occurs in a vessel-like structure, I next performed photothermal LSI and brightfield imaging on whole blood inside a glass capillary tube (Figs 3.4d, 3.7.c, 3.7.d). With photothermal LSI, I observed an instantaneous decrease in contrast within the irradiated region (black), as well as the regions to the right (blue) and left (red) of the laser pulse, with subsequent recovery to baseline values (Fig 3.7.c). With brightfield images of the blood-air interface, I observed immediate motion of blood to ~70μm beyond the initial position after photothermal excitation.

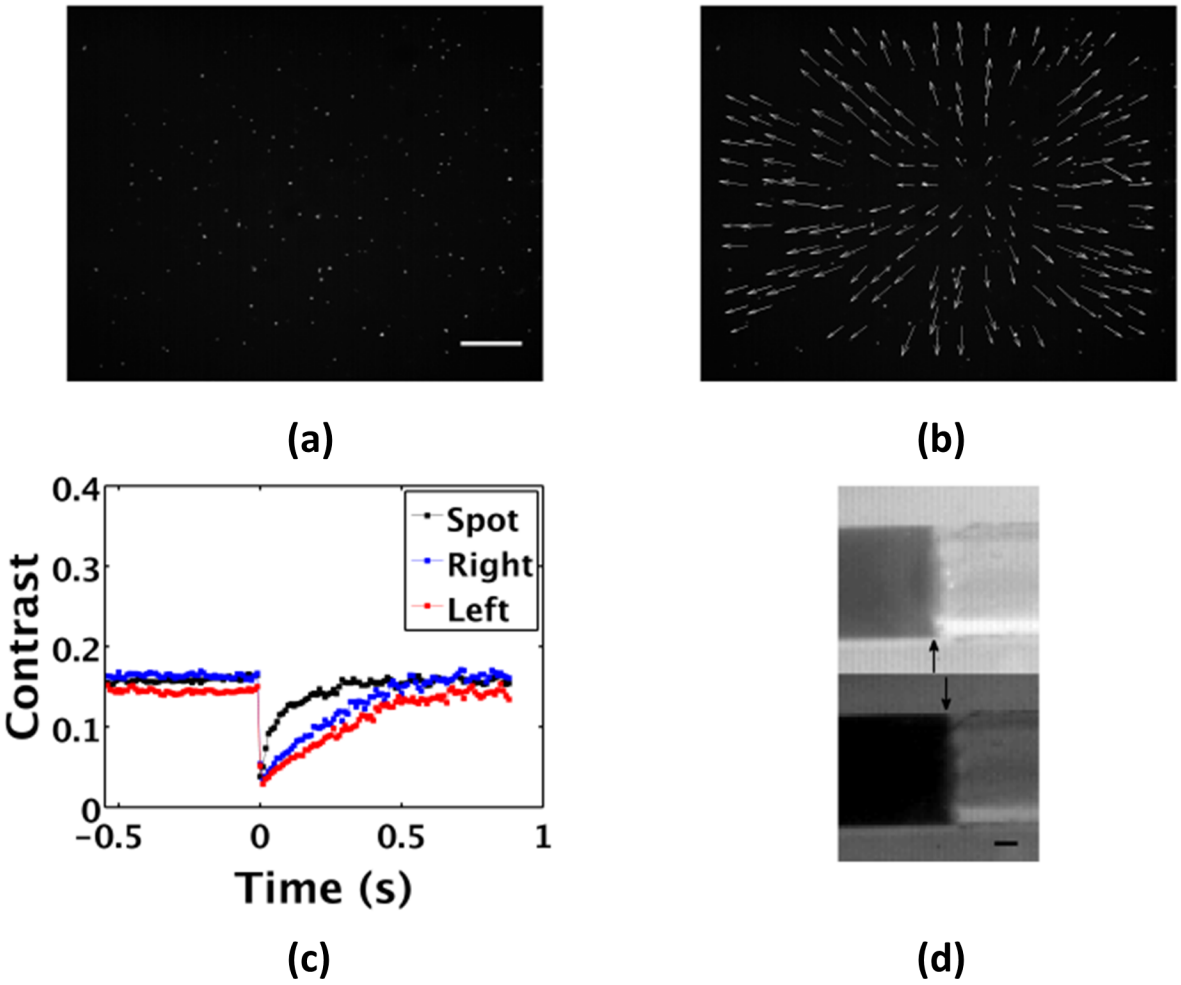

Figure 3.7: Following pulsed laser excitation, bulk motion of blood occurs due to thermally driven volume expansion. (a) Brightfield image of a 2mm thick layer of blood (scale bar = 1mm) with TiO_2 particles suspended on the surface. Video was acquired showing the lateral movement of these particles. (b) Particle image velocimetry (PIV) image showing the vector field associated with particle displacement. The vectors demonstrate that the motion in the sample radiates outward from the center of the excitation pulse. (c) Speckle contrast versus time of blood in a glass capillary tube. Contrast is shown for regions of interest both inside the irradiated region (black) and in regions adjacent to the directly irradiated region. When the photothermal excitation pulse is applied (time = 0s), the contrast immediately drops in all three regions, not just the irradiated spot. (d) Brightfield image of blood (dark) in a capillary tube before (above) and immediately after (below) photothermal excitation (scale bar = 100μm) showing the expansion that occurred. I postulate that the decrease in intensity in the lower frame is associated with saturation of the CCD sensor during photothermal excitation, as in subsequent frames there is no change in intensity of the blood or background.

The 4 J/cm^2 radiant exposure of the photothermal excitation pulse that we used in this study is above the ANSI safety limit of 0.26 J/cm^2 for skin[89]. To investigate this further, I performed preliminary calculations with a Monte Carlo layered model to investigate the fluence distribution $\Phi(z)$ and maximum temperature rise expected in human skin. With use of thermal properties from a previous publication, I estimated that the maximum temperature rise (assuming no heat diffusion during the pulse) $\Delta T = \Phi(z)\,\mu_a(z)/(\rho c)$ in the epidermis[96] to be 42°C. Although the calculated epidermal temperature rise is high, published clinical data using pulsed laser excitation at 577nm and 585nm of both normal and port-wine stain skin demonstrate that higher radiant exposures (>6.5J/cm^2) can be used without any observable epidermal injury[107,108]. Further research is warranted to investigate the sensitivity and safety of photothermal LSI to radiant exposure and to different sets of optical properties.

In conclusion, my collective data (Figs 3.5-3.7) strongly support hypothesis 3, that photothermal LSI achieves a transient reduction in speckle contrast due to bulk motion associated with thermally driven convection, and not due to pressure wave generation (hypothesis 1) or local effects driven by temperature dynamics (hypothesis 2).

Due to the relative simplicity of photothermal LSI, further work is warranted to study its potential applications for fluid characterization, biological and biomedical research. In this and my previous work[31], I focused on photothermal excitation of hemoglobin; I postulate that this approach can be extended to excitation of other endogenous and exogenous chromophores. The ability of photothermal LSI to image structures below a scattering medium may have important preclinical and clinical applications in future studies of theranostic contrast agent development, epithelial cancer, and angiogenesis.

3.2.5 Acknowledgements

I would like to acknowledge support from the Arnold and Mabel Beckman Foundation, the Air Force Office of Scientific Research (FA9550-14-1-0034), the National Institute of Health (R01 DE022831, R01 HD065536), the National Institute of Health Laser Microbeam and Medical Program (P41 EB015890), and the National Science Foundation BEST IGERT Program (DGE 1144901).

CHAPTER 4: Momentum transfer Monte Carlo for the simulation of laser speckle contrast imaging and its application in the skin

4.1 Abstract

To systematically study the effects of parameters such as optical properties and imaging geometry on speckle contrast, I developed a Monte Carlo based simulation of laser speckle imaging (LSI). I applied the model to an in depth exploration of the spectral dependence of speckle contrast signal in the skin, the effects of epidermal melanin content on LSI, and the depth dependent origins of the signal. I found that speckle imaging of transmitted light allows for more homogeneous integration of the signal from the entire bulk of the tissue, where as reflected contrast measurements are limited to a fraction of the light penetration depth. I quantified the spectral depth dependence of the contrast signal in the skin, and observed no statistically significant effect of epidermal melanin on speckle contrast. Finally, I corroborated these simulated results with experimental LSI measurements of flow beneath a thin absorbing layer. The results of this study have promising implications for the use of LSI in the clinic to monitor perfusion in patients with different skin types, or inhomogeneous epidermal melanin distributions.

4.2 Introduction

Laser speckle imaging (LSI) enables visualization and quantitation of blood flow and perfusion in biological tissues[3,2,109,13]. The dynamic intensity interference pattern provides information about the movement of scattering particles within tissue[1]. The pattern fluctuates over time at a rate proportional to the speed of the moving scatterers[7]. With use of a camera with an exposure time longer than the time period between speckle fluctuations, acquired images of dynamic regions of the interference pattern have

diminished speckle visibility[4]. This visibility, or speckle contrast, is quantified with calculation of the local standard deviation of intensity values over the local mean intensity within a sliding structuring element of pixels (typically 5x5 or 7x7 in size)[10]. The contrast is inversely proportional to the speed of the moving scatterers[8].

Research groups have utilized LSI for a variety of medical applications. We reported on LSI as a real-time approach to image perfusion during laser treatment of port-wine stain birthmarks[95,2,10,100]. Other groups reported on the use of LSI during neurosurgery[110,111,112]. In preclinical studies, LSI was used to visualize blood-flow dynamics following ischemic stroke[13] and in response to phototherapies[12,113].

Due to its simplicity and low cost, LSI has achieved widespread use, especially for the field of neurobiology. However, interpretation of the blood-flow maps remains ambiguous. LSI enables only limited visualization of vasculature below scattering layers such as the epidermis and skull[5]. Such layers are oftentimes described as having primarily "static" scattering, to differentiate them from layers with optical scattering events by "dynamic" red blood cells moving within blood vessels. For LSI in general, researchers typically are interested in mapping speckle contrast perturbations associated with these dynamic scatterers, but the static scattering components compromise the ability of LSI to quantify blood flow[6,61,18,19].

In addition, several optical imaging modalities are affected by the presence of absorption, particularly melanin absorption in the skin. For example, techniques such as diffuse optical spectroscopic imaging and spatial frequency domain imaging have difficulty decoupling absorption events from melanin versus hemoglobin[48,49]. This presents challenges for *in vivo* clinical imaging, in which patients have varying skin types and

different concentrations of epidermal melanin[46,47]. Previous work by our group and others demonstrated that absorption affects measurements of speckle contrast[114,115,116]. To study the sensitivity of speckle contrast to melanin-induced changes in absorption, I compared speckle contrast and reflectance values at different wavelengths and melanin contents. In this study, I explored the effects of epidermal melanin concentrations of 3%, 14%, and 30%, which represent fair, tan, and dark skin, respectively[47].

Here, I describe a computational model that enables flexible *in silico* study of the impact of these factors on LSI measurements. The model uses Monte Carlo methods to simulate light and momentum transport in a heterogeneous tissue geometry[37,43,42,44]. With the model, I studied the depth sensitivity of LSI by tracking the precise location of dynamic scattering events. I also applied the model to study the spectral dependence of speckle contrast as well as the impact of epidermal melanin content. Many of these questions would be difficult to address using traditional experimental LSI, but can be easily explored with the model.

4.3 Theory

Wang et al. described the seminal Monte Carlo model that has achieved widespread use to model light transport within multi-layered tissue[37]. Here, I used a modified version of the C# Command Line Monte Carlo model developed by the Virtual Photonics Initiative at Beckman Laser Institute to track photon scattering for an arbitrary tissue geometry using a discrete absorption weighting scheme[39,40,117] (Appendix A). I calculate the momentum transfer that occurs at each scattering event of a simulated photon[43]. All photons have a momentum ($\boldsymbol{\rho}$), described by $\boldsymbol{\rho}=\hbar\mathbf{k}$, where $\hbar$ is the reduced Planck's constant and $\mathbf{k}$ the wavenumber, which has both a magnitude and a direction. Momentum

transfer (**q**) occurs with each scattering event, and is quantified by the change in direction of the wavevector, or $\mathbf{q} = \mathbf{k}_{final}-\mathbf{k}_{initial}$, which has a magnitude ($|\mathbf{q}|$) given by $|\mathbf{q}|=(2k)\sin(\theta/2)$, where k is the wavenumber and θ the scattering angle of the photon.

By tracking momentum transfer, I estimate the field correlation function $g_1(\tau)$ for each simulated photon as:

$$g_1(\tau) = \exp[-\tfrac{1}{6}\Sigma q_i^2 <\Delta r^2(\tau)>] \quad (4.1)$$

I sum q for each scattering event "i" (static or dynamic) associated with a mean-squared displacement ($<\Delta r^2(\tau)>$) described either by Brownian motion ($6D_b\tau$) or directed flow ($v\tau^2$), where D_b is the Brownian diffusion coefficient and v the speed of directed flow. I integrate Eq. (4.1) over all photon paths generated by the Monte Carlo simulation, to obtain the total field correlation:

$$g_1(\tau) = \int_0^\infty P(Y)\exp\left[\frac{-Yk^2<\Delta r^2(\tau)>}{3}\right]dY \quad (4.2)$$

where Y is the dimensionless momentum transfer ($Y=1-\cos\theta$) and P(Y) the normalized probability distribution of momentum transfer[43,42]. The simulation computes Y for each scattering event and its corresponding summation along the total photon pathlength. With this information, I generate a histogram of normalized photon weight (P(Y)) versus dimensionless momentum transfer (Y) for each simulated photon.

Equations (4.1) and (4.2) are valid for a sample with a single mean-squared displacement value (i.e., $<\Delta r^2(\tau)>$ is uniform throughout the entire simulated geometry). We previously reported on modification of these equations to properly account for two different flow types or speeds, such as a static top layer overlying a dynamic layer, or a blood vessel within a medium[44]. For a two-flow system, the field correlation function is:

$$g_1(\tau) = \int_0^\infty P(Y) \int_0^1 P(y) \exp\left[\frac{-Yk^2[(y)<\Delta r_1^2(\tau)>+(1-y)<\Delta r_2^2(\tau)>]}{3}\right] dy dY \quad (4.3)$$

where P(Y) is the normalized probability distribution of the total momentum transfer, P(y) is the probability distribution of momentum transfer associated with flow type one, and $<\Delta r_1^2(\tau)>$ and $<\Delta r_2^2(\tau)>$ are the mean-squared displacements associated with each of the two flow types[44]. The equations for a two-flow system are readily adapted to a simulation of blood-flow dynamics in a layered skin model (described below). In this simulation, I use the blood volume fraction of each layer and a random number generator to identify each scattering event as either dynamic or static.

I then use the Siegert relation ($G_1=<I^2>+\beta|G_1(\tau)|^2 d\tau$) to calculate the intensity correlation function $G_2(\tau)$ and subsequently speckle contrast (K) as[118,119,120,121]:

$$K^2=\frac{2\beta}{T}\int_0^T \left(1-\frac{\tau}{T}\right)\left|\frac{G_1(\tau)}{G_1(0)}\right|^2 d\tau \quad (4.4)$$

where T is the exposure time of the camera and β an empirical constant which accounts for experimental factors such as pixel size of the detector and coherence length of the laser[1]. Here, I set β equal to unity to represent the maximum theoretical dynamic range of speckle contrast.

4.4 Virtual Detectors of the Momentum Transfer Monte Carlo (MTMC) Model

The Monte Carlo model uses virtual detectors to track quantities of interest such as the reflectance and transmittance, or the total weight and location of simulated photons exiting the simulated geometry. The absorbance, or weight of absorbed photons, and fluence, or weight of photons passing through each spatial location within the sample geometry, is tracked in all three dimensions.

To calculate speckle contrast, I used data from the reflected or transmitted momentum transfer detectors. These detectors quantify both total momentum transfer and the fraction of momentum transfer that occurred within each region. The latter quantity is further separable into the fraction that occurred from dynamic versus static scatterers. The histogram of the fractional momentum transfer events that occurred in dynamic versus static scatterers was used in the two-region calculation of field correlation (Eq. (4.3)).

Additionally, I created a detector to track momentum transfer as a function of depth within the sample. For each scattering event, the momentum transfer is multiplied by the final reflected or transmitted weight of the photon[122], and tabulated at the z-dimension of the event, enabling study of the depth over which dynamic scattering events affect speckle contrast values.

I used custom-written MATLAB software (The Mathworks, Natick, MA) to perform the numerical integration of Eq. (4.2) – (4.4) (Appendix B).

4.5 Experimental Methods

4.5.1 Validation Experiments

To test the MTMC model, I performed several *in vitro* LSI experiments. The LSI device consisted of a CMOS camera (HotShot 1280, NAC Imaging Technology, Simi Valley, CA) equipped with a macro lens (Nikon, Melville, NY) and a long-coherence 808nm laser diode (Ondax, Monrovia, CA). A ground-glass diffuser (ThorLabs, Newton, NJ) expanded the collimated diode output to achieve uniform illumination of the sample.

For the samples, I used both solid and liquid tissue-simulating phantoms. Solid phantoms consisted of a polydimethylsiloxane (PDMS) base with titanium dioxide added to achieve a reduced scattering coefficient (μ_s') of $\sim$1mm^{-1} at 650nm[74]. To create liquid

phantoms, I diluted Intralipid (Baxter Healthcare, Deerfield, IL) to a concentration of 1% or 1.7%, resulting in μ_s'=1mm^{-1} or 1.7mm^{-1}, respectively. To vary solution viscosity and hence the Brownian diffusion coefficient, I added 28% and 43% solutions of glycerol to the Intralipid dilution, similar to experiments reported by Rice et al[42]. For some experiments, I increased phantom absorption by adding a concentration of 0.005mg/ml (μ_a=0.005mm^{-1}) of Nigrosin. To achieve directed flow, I used a syringe infusion pump (Harvard Apparatus, Holliston, MA) to pump the Intralipid through a glass microchannel (inner diameter of 650μm) embedded within the surface of one of the PDMS phantoms described above (Fig 4.1.a).

4.5.2 Creation/Characterization of Thin, Flexible, Absorbing Phantoms

To mimic absorption due to melanin in the epidermis, I created thin, flexible, absorbing static phantoms using gelatin and Nigrosin. I dissolved 10g of powdered gelatin (Type A, 300g bloom, G1890) (Sigma-Aldrich, St Louis, MO) in 100ml of water while stirring continuously on a hot plate. I made a 10mg/ml solution of Nigrosin (Sigma-Aldrich, St Louis, MO) by dissolving 500mg Nigrosin in 50ml of water and sonicating for two hours. I created phantoms with five different final concentrations of Nigrosin; each phantom consisted of 0.4ml glycerol (Sigma-Aldrich, St Louis, MO), 10ml of the dissolved gelatin mixture, and 4.5ml of a Nigrosin dilution (total mg Nigrosin in Table 4.1). I spread 3.5ml of the gelatin-Nigrosin solution into a 6cm diameter Petri dish and let it set overnight. The resulting phantoms were measured with calipers in five random locations, and were found to be ~80μm thick. To characterize the absorption coefficient (μ_a) of each phantom I measured the transmittance using an integrating sphere (4P-GPS-033-SL, Labsphere, North Sutton, NH), and computed μ_a using Beer's law (Table 4.1).

Table 4.1: Absorption properties of thin flexible phantoms. Experimental and simulated contrast values are given for a 10ms exposure time. The percent difference between contrast for a given top layer and contrast with no top layer (A0) or the lightest phantom (A1) was computed for both *in vitro* and *in silico* results.

Phantom	Nigrosin (mg)	μ_a (mm^{-1})	$K_{measured}$ (T=10ms)	% Difference vs A_0	% Difference vs A_1	$K_{simulated}$ (T=10ms)	% Difference vs A_0 Simulated	% Difference vs A_1 Simulated
A_0	0	0	.1079	-	4.51%	.2216	-	0.2%
A_1	0.25	1.5	.1130	4.73%	-	.2541	0.2%	-
A_2	2.5	5.3	.1184	9.73%	4.78%	.2663	6.14%	5.93%
A_3	5.0	9.5	.1165	7.97%	3.1%	.2748	9.53%	9.31%
A_4	7.5	13.5	.1203	11.54%	6.5%	.2680	6.82%	6.6%
A_5	12.5	20.6	.1224	13.44%	8.32%	.2749	9.57%	9.35%

4.5.3 LSI of Absorbing Phantoms

In vitro experiments were conducted using the LSI setup described above. I imaged 20% Intralipid (Baxter Healthcare, Deerfield, IL) in the PDMS phantom containing a microchannel as described above. The thin, flexible, absorbing phantoms were placed over the microchannel (Fig 4.1.a). A sequence of 30 images was collected with the aperture set at f/8, acquisition rate at 30fps, and exposure time at either 10 or 30ms. To prevent pixel saturation when imaging samples with low absorption, neutral density filters (ThorLabs, Newton, NJ) were placed in front of the laser. Spatial contrast was computed using a 7x7 sliding window algorithm for each image, and contrast values in a region of interest were averaged over the 30 images. The region of interest was chosen as a 25x480 pixel area centered on the microchannel.

4.6 Validation of the MTMC Model

I compared data calculated with single layer model with results from Rice et al, who developed and worked with a similar model for spatial frequency domain laser speckle imaging[42]. I imaged mixtures of Intralipid, water, Nigrosin dye, and glycerol to test the sensitivity of LSI to samples with different diffusion coefficients (Table 4.2). To decrease

the diffusion coefficient, I added glycerol, and observed the expected, and previously demonstrated, trend of increasing contrast with increasing viscosity. The percent difference in contrast arising from measurements of 28% and 43% glycerol solutions, and simulations using the same glycerol solutions, was higher than expected, potentially due to use of a previously reported value of β in Eq. (4.4)[42]. This reduces the dynamic range of the simulated results to be similar to the experimental range, but this value can vary due to differences in the imaging hardware.

I also modified the diffusion coefficient using 0.3% weight per volume of 800nm polystyrene microspheres, and found the simulated contrast value of 0.200 matched the simulated value used by Rice et al[42].

To compare measurements from samples with different optical properties to the simulated results, I collected LSI data from samples with different quantities of Intralipid and Nigrosin and obtained less than 6% error between the simulated and experimental results (Table 4.2).

Table 4.2: Simulated contrast for model validation in homogenous samples with varying optical properties (μ_s' and μ_a) and diffusion coefficients (D_b). Experimental contrast is also listed, along with the percent error between the experimental and simulated contrast values.

Sample	μ_a (mm^{-1})	μ_s' (mm^{-1})	D_b (mm^2/s)	$K_{simulated}$	$K_{experimental}$	Percent Error
0% glycerol	$5x10^{-3}$	1	$2x10^{-6}$	0.121	0.118	2.5%
28% glycerol	$5x10^{-3}$	1	$0.86x10^{-6}$	0.172	0.148	16.5%
43% glycerol	$5x10^{-3}$	1	$0.5x10^{-6}$	0.223	0.182	22.3%
800nm microspheres	$5x10^{-3}$	1	$6.1x10^{-7}$	0.200	-	-
1% Intralipid	$3.3x10^{-4}$	1	$2x10^{-6}$	0.103	0.100	2.8%
1.7% Intralipid	$3.3x10^{-4}$	1.7	$2x10^{-6}$	0.097	0.103	5.6%

Additionally, I compared results from our two-region model with results from Rice et al[44]. I compared both a geometry consisting of a variable-thickness dynamic top layer above a 5cm thick static bottom layer, as well as a variable-thickness static top layer above a dynamic second layer (Table 4.3). I observe a trend of decreasing contrast with increasing thickness of the dynamic top layer, and conversely increasing contrast with increasing thickness of the static top layer. These trends agree with theoretical expectations, because the thicker the dynamic top layer, the more dynamic scattering events will occur, resulting in increased momentum transfer. Similarly, as the thickness of the static top layer increases, the number of detected photons that reach the dynamic second layer decreases, resulting in a decrease in momentum transfer from moving scatterers and a corresponding increase in contrast. My values follow the same trend reported by Rice et al[44], although they do not span the same range. I believe this discrepancy is due to a difference in approaches used to categorize the fraction of dynamic scatterers experienced by each photon.

Table 4.3: Simulated contrast for model validation in the two-layer geometry. The top layer was either static or dynamic with a thickness between 0.1mm and 4.0mm; the corresponding bottom layer was either dynamic or static respectively and 5cm thick.

Top Layer	Thickness of Top Layer (mm)	$K_{simulated}$
Dynamic	0.75	0.463
Dynamic	1.5	0.381
Dynamic	2.25	0.335
Dynamic	3.0	0.312
Dynamic	3.75	0.295
Static	0.4	0.301
Static	1.3	0.452
Static	2.2	0.580
Static	3.1	0.684
Static	4.0	0.769

I also used the two-region model to compare simulated flow in a vessel-like inclusion placed below the surface of a liquid phantom (Fig 4.1.a). I varied the simulated flow speed and computed contrast for different exposure times (Fig 4.1.b). As expected, the contrast decreased as exposure time increased because a longer integration time allows for more blurring of the speckle pattern. The contrast also decreased as flow speed increased, which is consistent with the fact that faster flow results in greater decorrelation of the speckle pattern. The scatter plot for flow at 0.375mm/s was in close agreement with simulation data by Rice et al[44].

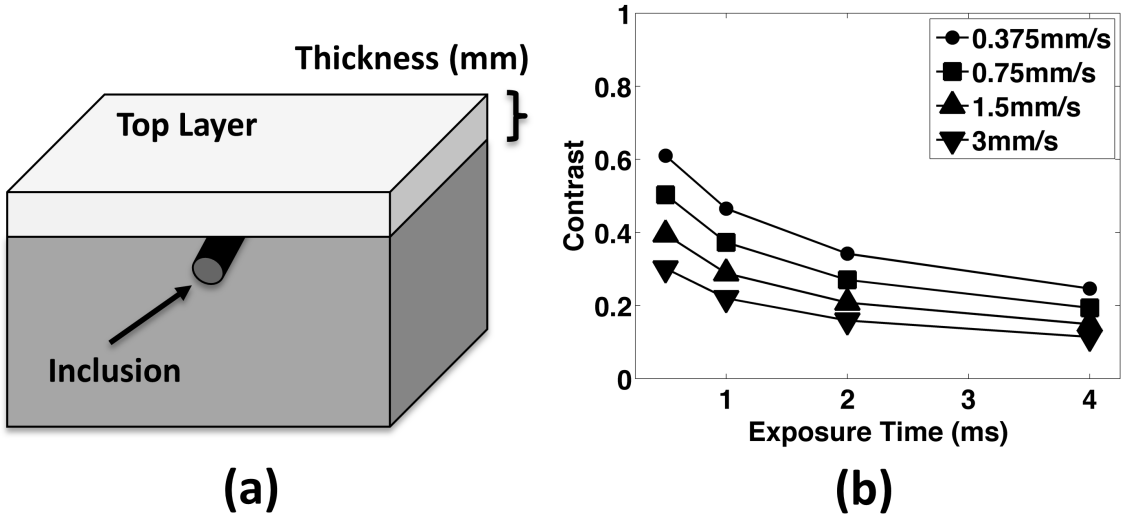

Figure 4.1: (a) Sample geometry for validation experiments. The sample consisted of a variable thickness (0.75-4.0mm) top layer above a 5cm bottom layer. For experiments with flow present, a glass microchannel inclusion was placed at the surface of the second layer and Intralipid was infused through the tube. (b) Results from simulated flow in a buried inclusion. I modeled speckle contrast for flow through a buried inclusion at different speeds and exposure times. As expected, speckle contrast decreased with increasing flow speed and exposure time due to the increased decorrelation time of the photons. The results closely matched previous work by Rice et al[44].

4.7 Effect of Optical Properties and Imaging Geometry on Speckle Contrast

With a homogenous, semi-infinite tissue geometry, I assessed the effect of tissue optical properties on reflected speckle contrast (Fig 4.2). I used a uniform square illumination source (30x30mm) to mimic the widefield illumination scheme commonly used with LSI. To compute speckle contrast (Eq, (4.4)), I assigned the homogeneous layer a Brownian diffusion constant of $2x10^{-6}mm^2/s$, which is typical of Intralipid in water[42]. I varied μ_a over five orders of magnitude, from $10^{-3}mm^{-1}$ to $10^{2}mm^{-1}$, covering a range of absorption values associated with different combinations of tissue type (i.e., skin, skull, blood) and illumination wavelength[90]. For these simulations, I kept the reduced scattering coefficient (μ_s') constant at $1mm^{-1}$. I computed the simulated speckle contrast at exposure times (T) of 1 and 10ms, which are frequently used experimentally (Fig 4.2.a).

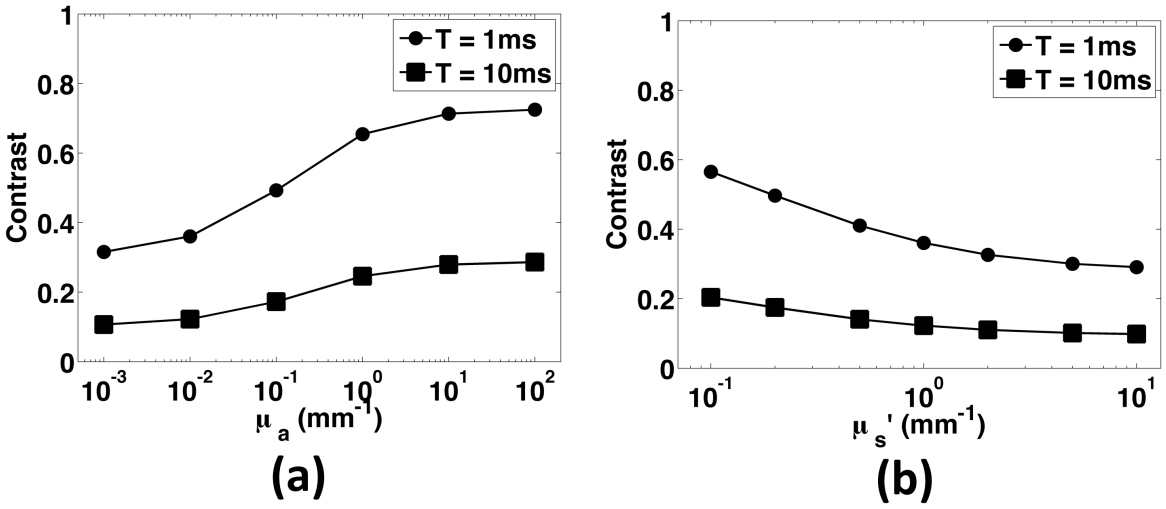

Figure 4.2: Simulated results from samples with varying optical properties, and exposure times. (a) Speckle contrast as a function of absorption coefficient with μ_s' held at $1mm^{-1}$ for two commonly used exposure times, 1ms (circles) and 10ms (squares). Speckle contrast increased with increasing absorption due to a reduction in the number of scattering events. Contrast is higher for shorter exposure times, which is consistent with speckle theory. (b) Speckle contrast as a function of reduced scattering coefficient with absorption held constant at $0.01mm^{-1}$. Contrast decreased as scattering increased due to the increase in momentum transfer associated with longer photon pathlengths.

Overall, speckle contrast increased with an increase in tissue μ_a, in agreement with the trend observed in previous studies[114,115]. As μ_a is increased, the number of scattering events per simulated photon is decreased, resulting in a decrease in momentum transfer and hence a slower decorrelation of the speckle signal.

I next performed a similar set of simulations, but instead held absorption constant at $0.01mm^{-1}$ and the scattering anisotropy (g) at 0.8, and I varied μ_s' over two orders of magnitude, from $0.1mm^{-1}$ to $10mm^{-1}$ (Fig 4.2.b). As μ_s' increased, contrast decreased. With an increase in the number of scattering events for each simulated photon, an increase in the total momentum transfer and hence a more rapid decorrelation of the sampled photons occurred, which led to a decrease in speckle contrast.

4.8 Spectral Dependence of Speckle Contrast in the Skin

To study the spectral dependence of speckle contrast, as well as the depth localization of dynamic momentum transfer events, I used a model of human skin. I simulated skin as a layered geometry consisting of a bloodless epidermis with 3% melanin content, which is representative of fair skin; and four dermal layers with varying blood-volume fractions representative of the papillary and reticular dermis and the upper and lower capillary blood nets (Fig 4.5.a). The blood-volume fraction and thickness of each layer are given in Table 4.4[123].

Table 4.4: Six-layer skin model with corresponding thickness and blood volume fraction of each layer.

Layer	Thickness (μm)	Blood Volume Fraction (%)
Epidermis	75	0.0
Papillary Dermis	150	0.4
Upper Blood Net	150	4.0
Reticular Dermis	800	0.4
Lower Blood Net	400	4.0
Lipid	up to 10mm	0.0

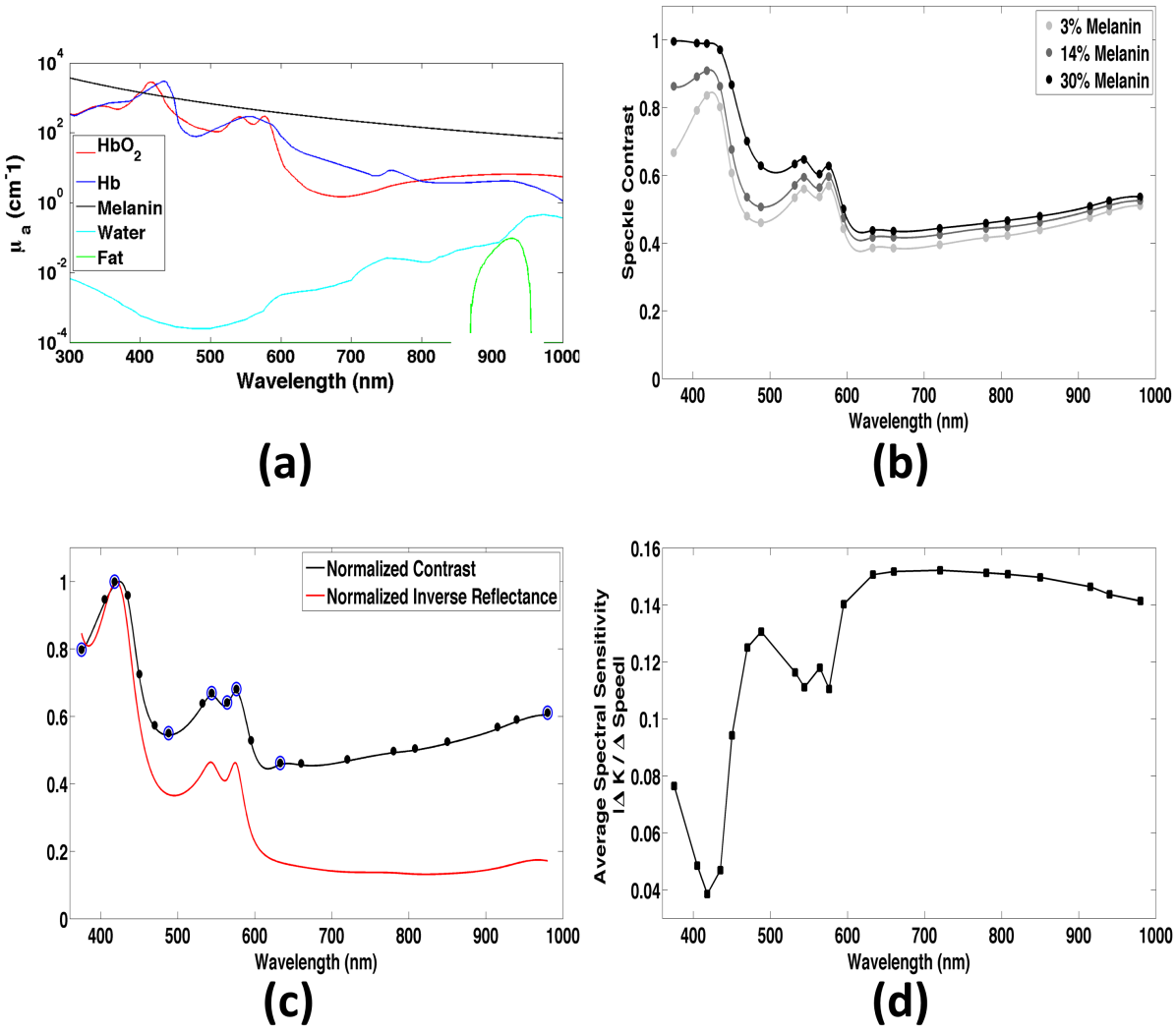

Figure 4.3: (a) Absorption spectra of chromophores in the skin. (b) Speckle contrast as a function of wavelength and epidermal melanin concentration for fair (3% melanin), tan (14% melanin), and dark (30% melanin) skin. Contrast increases slightly with increasing epidermal melanin, especially at lower wavelengths where the combined absorption of melanin and hemoglobin greatly shorten the photon pathlength. However, contrast values between the three cases are very similar in the optical window, and there is no significant difference in average contrast. (c) Normalized speckle contrast as a function of wavelength (black) compared to the normalized inverse reflectance (red). Both curves exhibit features of the hemoglobin absorption spectra, however, contrast is not as flat in the optical window. Blue circles indicate wavelengths where there is an inflection point in the contrast curve, which are used for the spectral analysis of momentum transfer. (d) Spectral sensitivity to changes in flow of contrast in skin with 3% melanin content. Contrast is most sensitive to changes in flow around 650-700nm.

I modeled a semi-infinite geometry with a static-scattering lipid layer below the skin. I used the spectral library and "makeTissue" function by Jacques to estimate optical properties for each layer at 21 wavelengths (375nm to 980nm)[124]. The wavelengths corresponded to features and key inflection points of the absorption spectrum of hemoglobin (Fig 4.3.a), and common wavelengths used for LSI. For each simulation, I used one million simulated photons distributed evenly over a 15x15mm square. To avoid any inconsistencies near the edges of the illuminated region, I calculated an average contrast over a central 7x7mm region of interest. I ran each simulation twice, using different seeds to the random number generator. For each pair of runs, I determined that both reflectance and contrast varied by less than 1%, suggesting that we used a sufficient number of simulated photons to compute speckle contrast. Furthermore, the relative error of the Monte Carlo was less than 5% indicating that the photon transport statistics were valid. I assigned the dynamic scatterers a flow speed of 0.36mm/s, which is representative of healthy tissue perfusion[125]. I simulated LSI with an exposure time of 10ms, which is common for LSI.

The spectral speckle contrast curve (Fig 4.3.b) exhibited many of the features of the absorption spectrum of hemoglobin (Fig 4.3.a). I next studied whether the observed changes in speckle contrast are due solely to the spectral variations in hemoglobin absorption. I calculated the normalized inverse reflectance values resulting from the Monte Carlo simulations. I observed a difference between inverse reflectance and hemoglobin absorption (Fig 4.3.c). In the 380-576nm wavelength region over which hemoglobin absorption is high, the contrast was less than 1.5 times the inverse reflectance. At wavelengths longer than 576nm, the contrast increased to two to four times the inverse

reflectance. These data suggest that the spectral speckle contrast curve does not replicate the spectral absorption curve.

To study the spectral sensitivity of speckle contrast to changes in flow speed, I calculated contrast for speeds from 0.01-5.1mm/s, in 0.175mm/s increments, for each of the 21 wavelengths. I calculated spectral sensitivity for each wavelength as the average of the absolute value of the change in contrast (ΔK) divided by the change in speed (ΔSpeed). The sensitivity of contrast was inversely proportional to the hemoglobin absorption. The sensitivity peaks around 700nm (Fig 4.3.d), suggesting that this wavelength achieves the best sensitivity to flow changes in the simulated skin geometry.

4.9 Depth Dependence of Momentum Transfer in the Skin as a Function of Wavelength

To study the origins of speckle contrast, I developed a virtual detector to track the weighted reflected momentum transfer as a function of depth. The detector tracks the dynamic momentum transfer events that occur at each depth. These events are then weighted by the final reflectance or transmittance value associated with each simulated photon[122].

I tested this detector by varying the μ_a (0.001, 0.01, 0.1 and 1.0mm^{-1}) in a 10mm thick homogeneous block of tissue with a reduced scattering of 1mm^{-1}. For each simulation, I estimated a characteristic penetration depth of light and a characteristic speckle origination depth. I set these characteristic depths to equal the depth over which 95% of the fluence and reflected momentum transfer occurred, respectively (Table 4.5). As the absorption increased over three orders of magnitude, the average penetration depth of the light decreased by a factor of 5.6. Over the same range of μ_a values, the speckle

characterization depth increased by a factor of 8.4 (Fig 4.4.a). For a given μ_a value, the penetration depth of light was greater than the speckle origination depth. Therefore, even if light reached a certain depth in a tissue, we do not necessarily obtain information from these regions in the reflected speckle contrast.

Table 4.5: Characteristic depth over which 95% of the fluence or reflected momentum transfer occurred for homogeneous samples with $\mu_s' = 1mm^{-1}$ and μ_a values varied over three orders of magnitude.

Absorption Coefficient (mm^{-1})	95% Fluence Depth (mm)	95% Reflected Momentum Transfer Depth (mm)
1.0	1.48	0.78
0.1	4.97	2.58
0.01	7.88	5.68
0.001	8.24	6.58

I next compared epi-illumination and trans-illumination LSI configurations. I computed the weighted momentum transfer as a function of depth for transmitted light (Fig 4.4.b). With trans-illumination LSI, I observed a decrease in total momentum transfer due to a decrease in the number of photons exiting the geometry. The depth distribution of momentum transfer also was more uniform, with lower contributions in the tissue regions closer to air. The decreased contributions near the upper surface was due to remittance of photons scattered at superficial depths.

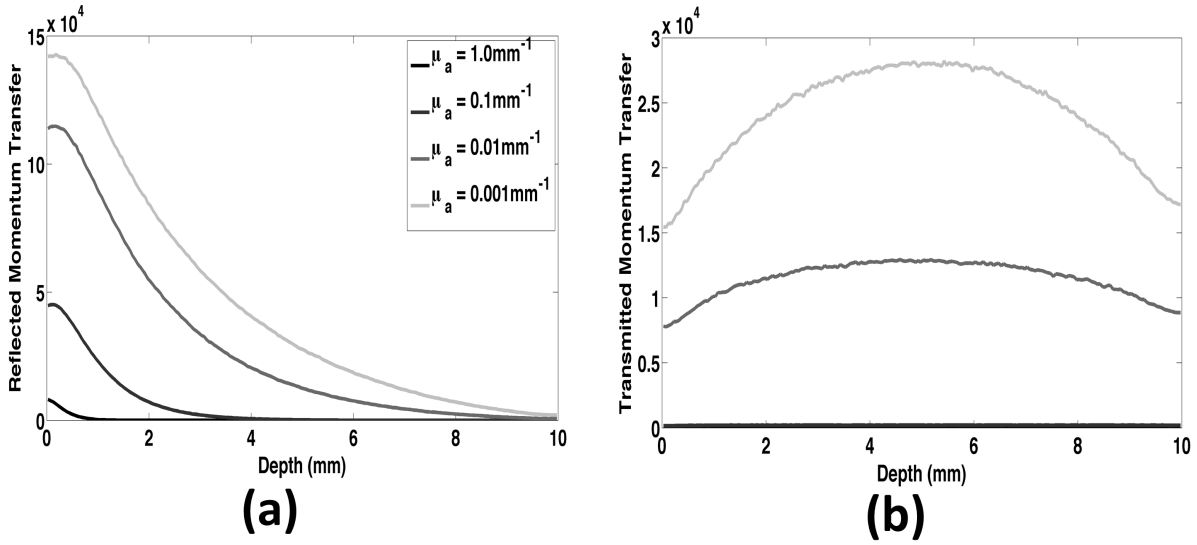

Figure 4.4: (a) Weighted reflected momentum transfer as a function of depth for a homogeneous sample with μ_s' held at $1mm^{-1}$ and absorption varied over three orders of magnitude. The majority of the reflected speckle contrast signal originates near the surface of the sample, however as absorption decreases there is more information contributing to the signal from deeper within the tissue. (d) Weighted transmitted momentum transfer as a function of depth for the same optical properties as (c). The transmitted contrast signal consists of information from throughout the entire depth. At very low absorption, the majority of the transmitted signal comes from the center of the sample.

I next applied this detector to simulations performed on the layered model of skin described above (Fig 4.5.a). I ran simulations at eight wavelengths associated with inflection points of the absorption spectrum in Figure 4.3.c (blue circles). Figure 4.5.b-4.5.d show plots of weighted reflected dynamic momentum transfer as a function of depth for three wavelengths. For each of the wavelengths, I observed an increase in dynamic momentum transfer in the upper blood net (shaded in red). With an increase in wavelength, the dynamic momentum transfer increased at deeper depths and especially in the lower blood net.

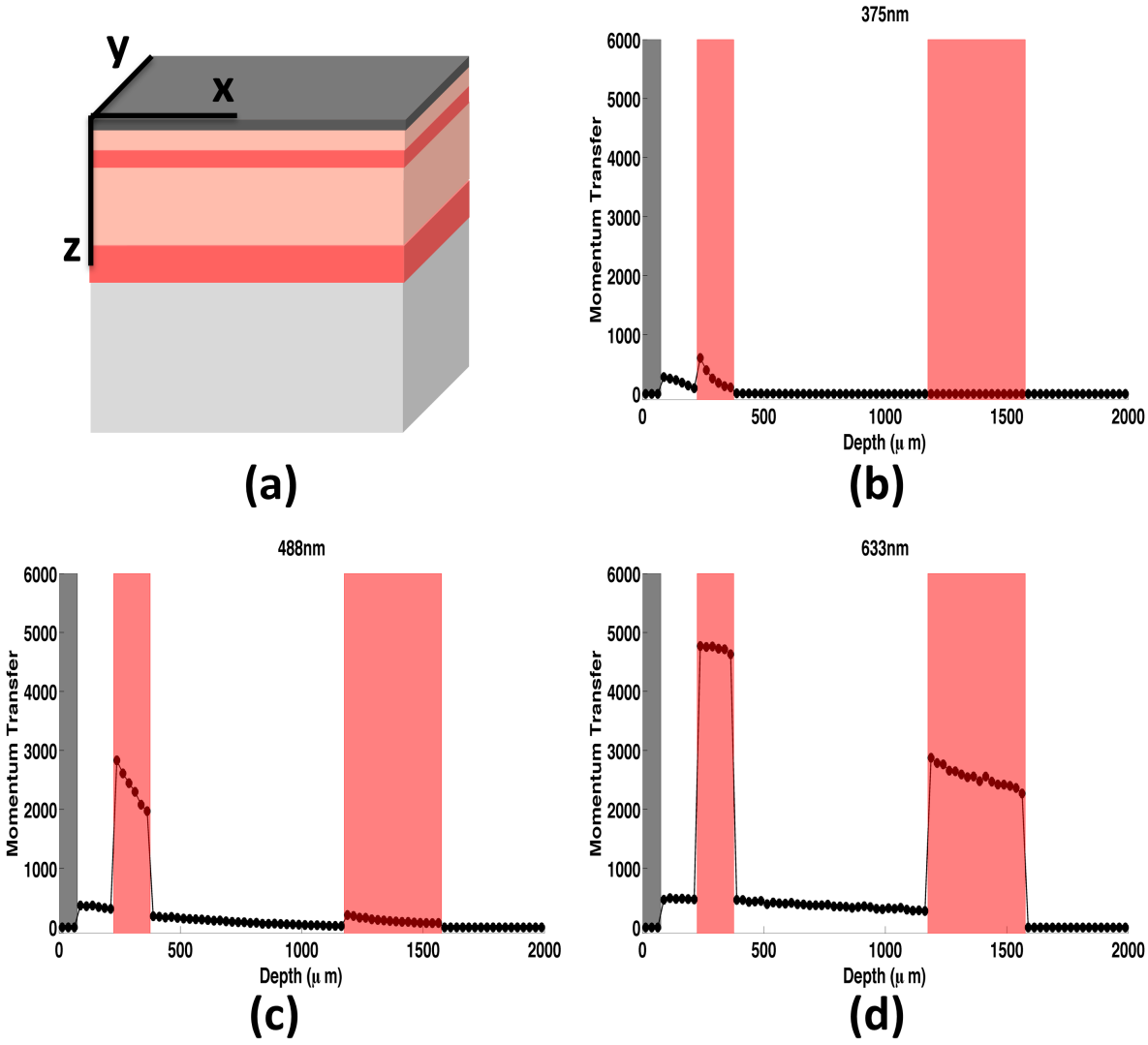

Figure 4.5: (a) 3D layered skin geometry used in simulations. The model of skin consisted of a static epidermis (dark gray), two highly perfused capillary beds (upper and lower blood nets, red), and two dermal layers (papillary and reticular dermis, light pink). There is a semi-infinite lipid layer (light gray) below the skin to backscatter the light. (b)-(d) Dynamic momentum transfer as a function of depth (z) for three different wavelengths: (b) 375nm, (c) 488nm, and (d) 633nm. The upper and lower blood nets (highlighted in red) contribute most to the overall contrast signal because they are 10x more perfused than the rest of the dermis. As wavelength increases, more of the signal is obtained from deeper within the tissue.

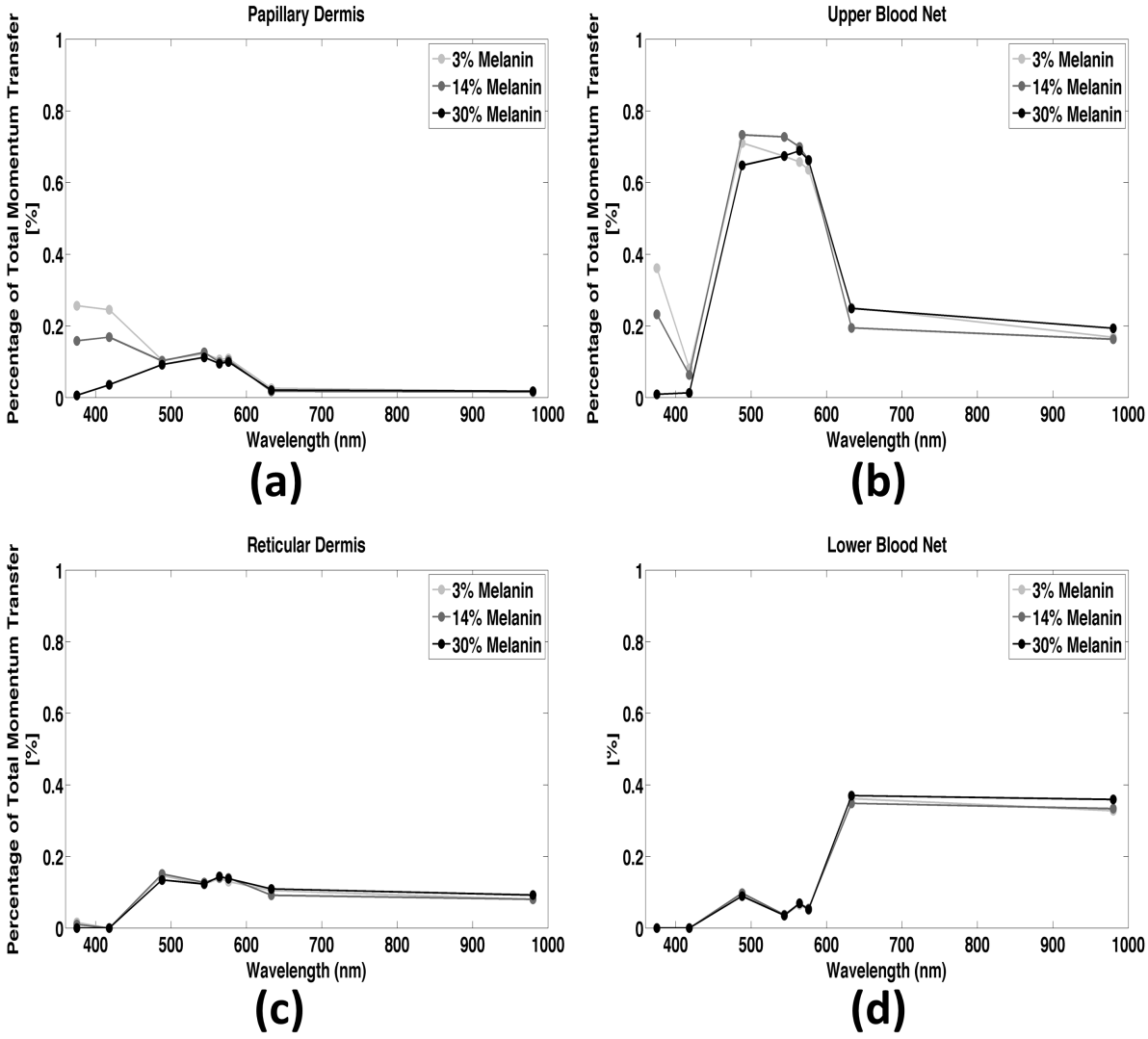

Figure 4.6: Percentage of the total momentum transfer contributing to the speckle contrast signal as a function of wavelength and epidermal melanin content for each dermal layer. There is no significant difference in the percent contribution between tissues with different melanin contents. (a) Very little of the signal comes from the papillary dermis, especially at wavelengths typically used for LSI (above 600nm). (b) Most of the contrast signal originates from the upper blood net at lower wavelengths (below 600nm) (c) The proportion of signal coming from the reticular dermis is relatively uniform across different wavelengths. (d) The majority of the speckle contrast signal originates in the lower blood net for wavelengths typically used in LSI (>600nm) supporting the potential for rough depth sectioning using dual-wavelength LSI.

I studied the relative contribution of momentum transfer at different depths to the speckle contrast signal. I calculated the percentage of the total reflected momentum transfer arising from different layers of the simulated tissue (Fig 4.6, light gray). This percentage represented the dynamic momentum transfer integrated over each dermal

layer, divided by the total momentum transfer in the entire tissue geometry. At wavelengths between 488 and 576nm, the percentage was highest (~0.67%) from the upper blood net (Fig 4.6.b), due to the relatively low penetration depth of those wavelengths. At wavelengths below 600nm, dynamic scattering within the papillary dermis contributed to the signal (~0.10-0.26%) (Fig 4.6.a). At longer wavelengths, the contribution from the papillary dermis was negligible (<0.03%) and the majority (~0.35%) of the speckle contrast signal arose from the lower blood net (Fig 4.6.d). This finding is consistent with the increased penetration depth at these longer wavelengths.

Collectively, these simulated data show the potential of the model to improve understanding of the contribution of tissue architecture to the speckle contrast signal. At red and near infrared wavelengths, which are typically used for LSI, the primary contribution is from the lower blood net. With use of shorter wavelengths, contribution is predominantly from the upper blood net. This result supports the rationale for two-wavelength LSI (i.e., 543nm HeNe and a 785nm laser diode) to perform coarse depth sectioning of blood-flow measurements.

4.10 Impact of Epidermal Melanin Content on Speckle Contrast in Layered Skin Model

In a homogeneous scattering medium, speckle contrast correlates with μ_a (Fig 4.2). This trend is in agreement with previous findings[114]. I next set out to study the effects of a thin, statically scattering, absorbing top layer, such as the epidermis, on speckle contrast. I used the layered skin geometry described above (Fig 4.5.a). The epidermal melanin concentration was set at 3, 14, and 30%, representative of fair, tan, and dark skin respectively. Speckle contrast increased with melanin content, as increasing epidermal μ_a

decreased the number of dermal dynamic scattering events. The difference is greatest at wavelengths shorter than 500nm, at which melanin absorption is very strong (>20mm^{-1} for 30% melanin). However, the mean speckle contrast for each of the three concentrations of melanin is not significantly different (one-way ANOVA, $p>0.05$).

I also determined the normalized reflectance spectrum for each of the three melanin distributions (Fig 4.7.a). As melanin content increased, the spatial features of the hemoglobin absorption spectrum became less prominent. The reflectance values calculated with 3% melanin differed significantly from those at higher melanin contents (one-way ANOVA, $p = 2.6\text{x}10^{-5} < 0.05$).

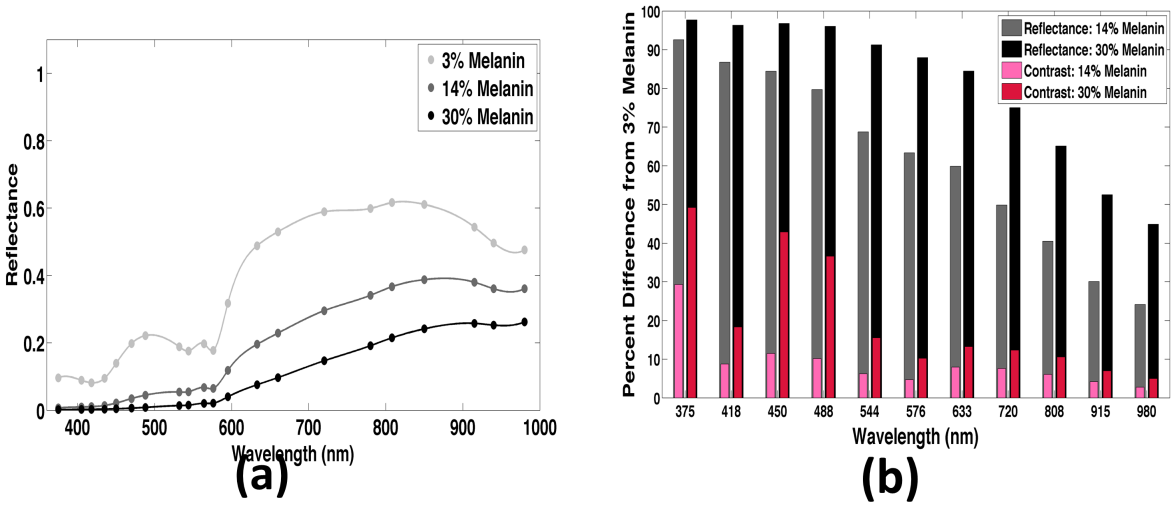

Figure 4.7: (a) Reflectance as a function of wavelength and epidermal melanin content. At 3% melanin content (light gray) the reflectance curve contains features of the hemoglobin absorption curve. However, as epidermal melanin increases (dark gray, black), the reflectance curve flattens out and is dominated by features of the melanin absorption curve. (b) Percent difference in speckle contrast (pink/red) and reflectance (gray/black) values between light skin (3% melanin) and tan/dark skin (14% / 30% melanin). The percent difference in contrast is significantly less than the difference in reflectance, indicating the potential for clinical use of LSI over other optical reflectance techniques.

I compared contrast and reflectance values associated with the three epidermal melanin content skin types. Specifically, I calculated the percent difference between the contrast or reflectance value for skin with 14 or 30% melanin and the respective value for skin with 3% melanin (Fig 4.7.b). The percent difference in reflectance ranges from 24-93% for tan skin and 44-98% for dark skin. At each wavelength, the impact of epidermal melanin content is greater for reflectance than for speckle contrast. At 808nm, I observed only a ~6% difference in contrast between tan (14% melanin) and fair (3% melanin) skin. At 633nm, I observed only a 13% difference in contrast between dark (30% melanin) and fair (3% melanin) skin. These percent differences are less than the changes in speckle contrast that were observed in previous *in vivo* studies. For example, a 20-60% change in contrast was reported during laser therapy of port-wine stain birthmarks[2], and a 20-55% change in contrast was associated with burn wounds[126]. With analysis of the depth distribution of dynamic momentum transfer (Fig 4.6), I determined that the average percentage of dynamic momentum transfer did not significantly differ among skin with different epidermal melanin content (ANOVA, $p>0.05$) for any of the four dermal layers ($p=.1747, .9315, .9998, .9972$). Collectively, these data suggest that the impact of epidermal melanin content on speckle contrast values and the depth sensitivity of LSI is unexpectedly small.

To test this *in silico* observation, I next performed experiments involving flow of Intralipid in a 650μm tube beneath thin absorbing phantoms that simulated epidermal melanin absorption. I computed the spatial speckle contrast in a region of interest above the tube. The exposure time was set at 10ms, which matched the time used in the simulated data described above.

I fabricated five thin (~80μm) absorbing phantoms using gelatin for structure and Nigrosin dye for absorption (Table 4.1). I selected gelatin concentrations to ensure fabrication of flexible phantoms that were neither sticky nor brittle. The absorption of phantom A_1 (μ_a =1.5mm^{-1}) matched that of fair skin at wavelengths longer than ~550nm and tan skin at wavelengths longer than ~870nm. The absorption of phantom A_5 (μ_a = 20.6mm^{-1}) matched that of dark skin at 495nm and tan skin at 395nm. Hence, I achieved epidermal μ_a values that spanned the range of values reported in the literature over the visible and near infrared spectral region for melanin concentrations of 3-30% (Fig 4.8.a).

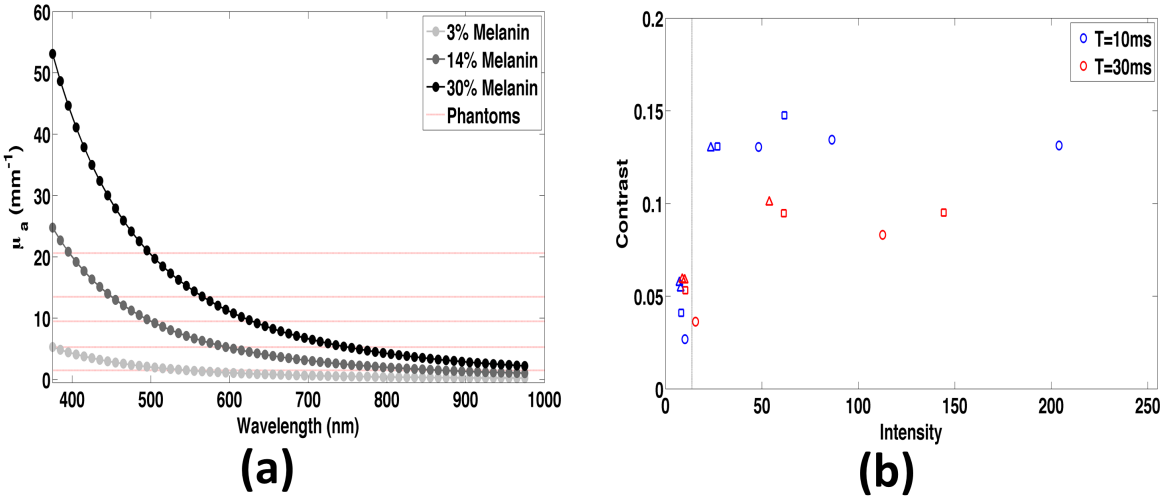

Figure 4.8: (a) Absorption coefficients of epidermis with different melanin content compared to absorption coefficients of five absorbing phantoms at the wavelength used *in vitro* (808nm). Phantoms A_1-A_3 span the range of absorption coefficients found in skin at wavelengths used for LSI (>600nm). (b) *In vitro* speckle contrast as a function of intensity (T = 10ms) (blue) and (T = 30ms) (red). The dotted line represents the dark counts of the camera. Contrast values are significantly different for images with intensity below 23 counts; above that, contrast is insensitive to image intensity.

I calculated the percent difference in contrast among each of the five phantoms and the contrast when no top layer was present. I also calculated the percent difference in contrast measured using phantoms A_2-A_5 and the least absorbing phantom (Phantom A_1, μ_a = 1.5mm^{-1}) (Table 4.1). The percent difference in contrast ranged from ~4 to 13% when compared to the contrast measured with an absorbing layer, and ~3 to 8% compared with Phantom A_1. These measurements support the findings from the layered simulation data (Fig 4.6).

4.11 Impact of Epidermal Melanin Content on Speckle Contrast in Subsurface Inclusion

I next ran simulations in which 20% Intralipid was present in a tube placed beneath a static absorbing top layer. I used a rectangular inclusion geometry, with an 800x800μm cross-section. This inclusion was at the surface of a static scattering layer (μ_s' = 1mm^{-1}), with an 80μm thick static absorbing layer positioned above. I selected the μ_a values of the absorbing layer to match those of our *in vitro* phantoms (Table 4.5). I calculated contrast based on reflected momentum transfer values from a region of interest directly above the inclusion. I used a Brownian diffusion constant of 2x10^{-6}mm^2/s, an exposure time of 10ms, and an excitation wavelength of 808nm.

I computed the corresponding percent difference among contrast values associated with the different absorbing top layers and either a clear, non-absorbing top layer (A_0) or the least absorbing top layer (A_1) (Table 4.5). These values ranged from ~0.2 to 10% when compared to a clear top layer, and ~6 to 9% when compared to top layer A_1. Collectively, these *in silico* and *in vitro* data demonstrate that LSI measurements of subsurface flow are only minimally impacted by large differences in epidermal melanin content.

4.12 Conclusions

In conclusion, I developed a Monte Carlo model to simulate LSI in a heterogeneous tissue geometry. The virtual detectors of the model track several important characteristics of light, including the absorbance, reflectance, transmittance, fluence, and momentum transfer. This model provides a simple method to study aspects of LSI that may be difficult or unwieldy to address in an experimental settings. The model can account for different skin geometries and other tissue types (i.e., brain), to enable detailed study of the fundamental origins of speckle contrast modulation in tissue-specific geometries.

I found that the speckle contrast signal originates more uniformly throughout a tissue in trans-illumination configurations compare to epi-illumination (Fig 4.4). I observed that the speckle contrast spectrum contained similar features to the absorption of hemoglobin (Fig 4.3.b), and that the spectral sensitivity was inversely proportional to hemoglobin absorption (Fig 4.3.d). I determined that shorter wavelengths characterize blood flow primarily within the upper blood net and papillary dermis, and longer ones characterize blood flow primarily from the lower blood net (Fig 4.6). This indicates the potential for segmenting perfusion information from different depths by using multiple wavelengths to perform LSI.

I also demonstrated that epidermal melanin concentration has a smaller effect on speckle contrast than on reflectance (Fig 4.3.b, 4.6). These results have important implications for clinical applications of laser speckle imaging in patients with different skin types, especially for patients with darker skin (Fig 4.7, Table 4.5). Other reflectance based optical imaging technologies have experienced difficulties when imaging patients with darker skin types, therefore if laser speckle imaging is significantly less sensitive to

changes in melanin content, it opens up the opportunity to measure blood flow in any patient regardless of skin type. One such potential clinical application is during skin flap surgery, where doctors need to identify if tissue has been perfused during the surgical operation. Another potential dermatological application is for identifying cancerous skin lesions where there is increased blood flow beneath high melanin containing nevi.

4.13 Acknowledgements

This research would not have been possible without Dr Carole Hayakawa, who created and modified many of the virtual detectors of the Monte Carlo simulation to incorporate the various aspects of momentum transfer tracking. I would also like to thank the entire Virtual Photonics Initiative for use of their Monte Carlo software.

CHAPTER 5: Monte Carlo simulation of multi-exposure speckle imaging to study the depth dependence of contrast signals

5.1 Introduction

In Chapters 1-3 I describe the use of different processing algorithms and imaging techniques to improve the quantitation and visualization of laser speckle contrast imaging[6,31,35]. However, I continue to face limitations, particularly when visualizing vasculature below ~200μm (Fig 5.1.c). Techniques such as multi-exposure speckle imaging (MESI) have been proposed to improve the quantitative accuracy of LSI[19,127].

MESI is a technique developed by Parthasarathy et al to improve the accuracy of laser speckle contrast analysis below static scattering layers[19]. By acquiring LSI images at multiple different exposure times, a theoretical model of contrast can be fit to measured data:

$$K(T,\tau_c) = [\beta\rho^2 \frac{e^{-2x}-1+2x}{2x^2} + 4\beta\rho(1-\rho)\frac{e^{-x}-1+x}{x^2} + \beta\nu_{ne} + \nu_{noise}]^{1/2} \quad (5.1)$$

where T is the exposure time, τ_c the correlation time, ρ the fraction of dynamically scattered light, x is T/ τ_c, and ν the variance due to non-ergodic light and noise. The non-ergodic variance term is the fraction of statically scattered light, or $(1-\rho)^2$. In a non-ergodic system, ensemble averaging of the intensity correlation function is no longer equivalent to temporal averaging[128]. Statically scattering media is non-ergodic, resulting in the breakdown of the traditional contrast model, which does not account for this term[54]. This model purportedly improves estimation of the correlation time, which is proportional to the inverse speed of the moving scatterers. Other parameters including ρ, β, and ν can also be obtained from this fit.

Preliminary *in vitro* measurements using the MESI technique indicated limitations in flow quantification below ~200μm. To further explore this apparent depth limitation from a theoretical perspective, I implemented the Monte Carlo model of light transport and simulation of laser speckle contrast described in Chapter 4. I used the simulation to model LSI and MESI of flowing blood in a microchannel at various depths. I also quantified the momentum transfer, the key factor contributing to the decorrelation of photons that dictates speckle contrast values, as a function of depth and spatial position in both trans-illumination and epi-illumination geometries.

5.2 Materials/Methods:

5.2.1 Single and multi-exposure LSI in a variable-depth tube (in vitro and in silico)

We developed a MESI system similar to the one described by Parthasarathy et al[19]. The system used a 633nm diode laser (Ondax, Monrovia, CA) to illuminate the sample, and an acousto-optic modulator (Gooch and Housego, United Kingdom) to diffract the laser beam incident onto a sample for the given exposure times. Images were collected with a Chameleon2 camera (Point Grey, Richmond, BC, Canada), and the entire system was controlled with custom LabVIEW software (National Instruments, Austin, TX). I performed *in vitro* experiments studying flow in a 650μm inner diameter microchannel buried at different depths below a static scattering layer at speeds from 1-10mm/s. The static scattering layers were composed of polydimethylsiloxane (PDMS) with TiO_2 added to create a reduced scattering (μ_s') of $1mm^{-1}$, and have thicknesses of 200, 500, 700 and 1100μm. The overall thickness of the phantom was ~10mm. I imaged 1% Intralipid (Baxter Healthcare, Deerfield, IL) infused in the microchannel using a syringe pump (Harvard Apparatus, Holliston, MA). Images were collected in an epi-illumination configuration at 16

exposure times between 0.025ms and 80ms. Contrast values were computed for each exposure time and fit to Eq. (5.1) to extract the correlation time (τ_c), and parameters ρ and β.

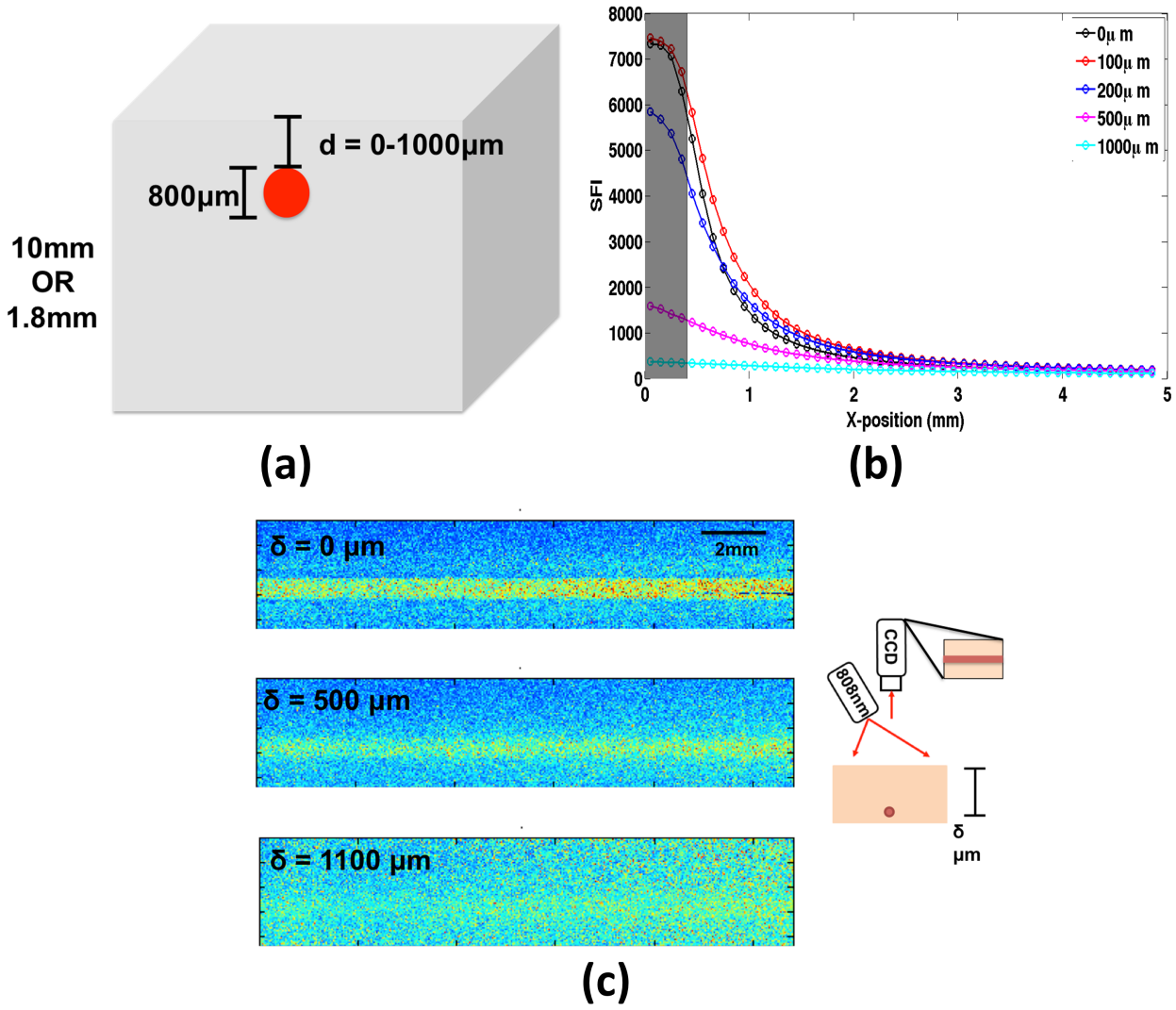

Figure 5.1: (a) Sample geometry for *in silico* experiments. An 800μm blood filled microchannel was placed between 0 and 1000μm below the surface of a homogeneous block with a μ_s' of $1mm^{-1}$. The total thickness of the block was 10mm (thick) or 1.8mm (thin). (b) SFI ($1/(2TK^2)$) of the simulated vessel (gray) at lateral distance (X) away from the center of the tube at varying depths below a static scattering layer. The difference in contrast between the vessel and the surroundings markedly decreases below 200μm. (c) Temporal speckle contrast images of blood in a microchannel at different depths below a static scattering layer. Spatial resolution of deeper vessels is poor.

To compare *in vitro* experimental results to data generated by the Monte Carlo model described in Chapter 4, I simulated blood flow in an 800μm square cross-sectional microchannel embedded at different depths in a static layer with μ_s' of $1mm^{-1}$ (Fig 5.1.a). The total layer thickness was either 10mm or 1.8mm, and the distance from the surface to the top of the inclusion ranged between 0 and 1000μm. I computed the average simulated speckle contrast in a region of interest directly above and below the tube at the same exposure times used *in vitro*, and speeds of 0.25, 0.5, 1, 1.5, 2, 3, 4, and 5mm/s. I fit the data with Eq. (5.1) to obtain the correlation time (τ_c), fraction of dynamically scattered light (ρ), and experimental constant β.

5.2.2 Relationship between blood volume fraction, ρ and τ_c

To study the relationship between the fraction of dynamic scatterers present in a sample (i.e: the blood volume fraction) and the ρ term in Eq. (5.1), I used the Monte Carlo model of speckle contrast described in Chapter 4. The virtual tissue was a 10mm thick homogeneous sample with optical properties of dermal tissue at 633nm ($\mu_a = 0.0182mm^{-1}$, $\mu_s' = 2.296mm^{-1}$)[124] (Fig 5.1.a). I simulated 10^6 photons distributed uniformly over a 15x15mm region. To observe the effect of μ_s' on the ρ term and the correlation time, I also ran a series of simulations with μ_s' decreased to $0.5mm^{-1}$. I varied the blood volume fraction, or the fraction of dynamic scattering events, from 0.01% to 0.1% in increments of 0.01%; 0.5%, 1%, 2%, and 5%; and 10% to 100% in 10% increments. I computed contrast from the reflected momentum transfer of remitted photons averaged over an 11x11mm region of interest for flow at eight speeds (0.01, 0.1, 0.36, 0.5, 1, 2, 5, and 10mm/s), and 16 exposure times between 0.025 and 80ms. To determine the sensitivity of the model to

noise in the data, I added random Gaussian white noise with variance of .0001 (1% noise) to the contrast values, and fit the noisy data to Eq. (5.1).

5.3 Results and Discussion

5.3.1 Modification of the MESI Equation

After experimentation with fitting Eq. (5.1) to data from controlled *in vitro* experiments as well as contrast values generated using Monte Carlo simulations, I modified the equation to remove the ν_{noise} term. The non-ergodic variance (ν_{ne}) term accounts for the DC offset in speckle contrast due to static scattering[19]. The β parameter controls the reduction in dynamic range (ie: limits the highest possible contrast value) that occurs due to factors in the experimental set-up including coherence of the laser, polarization, and speckle size[1]. By including the ν_{noise} term when fitting data taken in controlled or simulated conditions (ie: not *in vivo*) where there was no significant experimental noise, I was overfitting the data. In trying to fit for this term, the model described in Eq. (5.1) forced unnecessary variations in ν_{ne} (and hence ρ) and β. The model was fit using MATLAB's (The Mathworks Inc., Natick, MA) non-linear least squares function. I used lower bounds of 0 for all parameters, and an upper bound of 0.1s for the correlation time, which is limited by the maximum exposure time of the camera. The upper bounds of ρ and β were both set to 1, which is the theoretical maximum value. The search was initialized at the central values 0.05, .5 and .5 for these parameters respectively.

5.3.2 Single exposure LSI in a variable-depth tube

Figure 5.2.a shows simulated speckle contrast as a function of flow speed in a region of interest above the microchannel for the thicker (10mm) sample geometry at an exposure time of 10ms. As flow speed increases, the speckle contrast decreases, in line with

established speckle contrast theory[1]. As the thickness of the static top layer above the tube increases from 0 to 1000μm, the contrast values increase due to the increase in the relative amount of static scattering[6]. These results match those obtained from experimental spatial speckle contrast imaging presented in Chapter 1. The epi-illuminated contrast values for the thin (1.8mm) sample are similar to those from the standard thick (10mm) sample (Fig 5.2.b), indicating that the presence of a static backscattering layer may not be necessary for LSI. The deepest vessel (1000μm below the surface) has slightly higher contrast in the thin geometry. This may be due to the fact that dynamic photons that reach 1000μm deep are more likely to be transmitted than reflected.

The trans-illuminated contrast in the thin sample has a similar dynamic range across flow speeds as the epi-illuminated contrast (Fig 5.2.d). As expected, contrast in the trans-illuminated region of interest at depth 1000μm is now lower than the surface vessel because it is more likely to detect photons that have dynamic scattering. The dynamic range of trans-illuminated contrast in the thicker sample is very low, and the contrast values are relatively high due to the limited number of dynamic photons that make it through the tissue to the region of interest directly below the tube (Fig 5.2.c).

To study the spatial resolution of a buried microchannel, I calculated a simulated speckle flow index (SFI = $1/(2TK^2)$, where T is the exposure time (10ms) and K is the speckle contrast) as a function of lateral position from the tube (Fig 5.1.b). To quantify the ability to resolve the vessel from the surroundings, I computed the full-width-half-max (FWHM), or the lateral position at which the SFI value is half of the maximum value from the center of the microchannel. There is a distinct increase in FWHM between 200μm and 500μm from ~1.1mm to 1.9mm. This corresponds with experimental observations that

spatially visualizing and resolving a microchannel beneath static layers greater than 200μm is difficult (Fig 5.1.c).

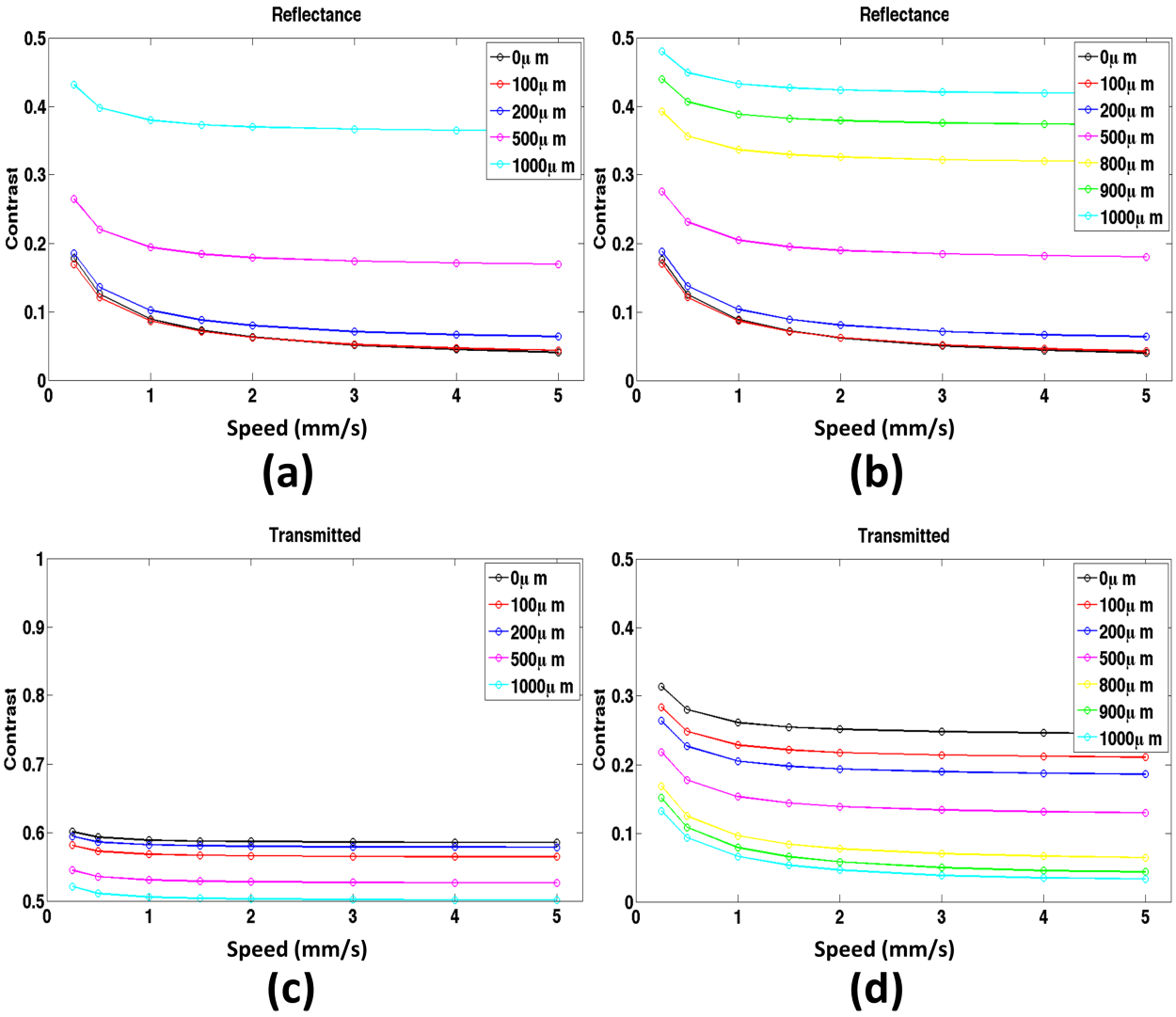

Figure 5.2: (a) Simulated speckle contrast in the thick (10mm) sample as a function of flow speed for blood in a buried microchannel in an epi-illumination / reflected light geometry. Contrast increases with increased static scattering. (b) Reflected speckle contrast versus flow speed in the thin (1.8mm) sample. (c) Simulated speckle contrast in the thick (10mm) sample as a function of flow speed for blood in a buried microchannel in a trans-illumination / transmitted light geometry. Contrast values are relatively high due to the significant amount of static scattering. (d) Transmitted speckle contrast versus flow speed in the thin (1.8mm) sample. Transmitted contrast values are fairly similar to the reflectance contrast values however the curves flipped (ie: lower contrast for deeper microchannel) because a large portion of the light will be dynamically scattered from the deeper vessel before it is transmitted.

To visualize and explain why the resolution of a dynamic microchannel becomes worse as the static top layer thickness increases, I mapped the total dynamic momentum transfer as a function of the reflected position of the simulated photons (Fig 5.3). These maps show how much of the dynamic momentum transfer that occurred in the microchannel is contained by the remitted photons. As the microchannel is buried deeper within a static scattering medium, photons that have accumulated dynamic scattering in the vessel are more likely to scatter and exit laterally compared to when the vessel is directly below the surface. It is qualitatively observed that the edges of the vessel are difficult to distinguish when the vessel is deeper than 200μm (Fig 5.3.d, 5.3.e). There is no spatial structure present in the maps of transmitted momentum transfer from a thick (10mm) sample. The reflected momentum transfer maps from a thin (1.8mm) sample illustrate similar results to the thick geometry (Fig 5.4).

However, the trans-illuminated maps of thin samples do not show clear spatially resolved vessels at these depths although diffuse momentum transfer is present (Fig 5.5.a-5.5.e). If I simulate a geometry similar to a rodent dorsal window chamber (300μm static layer above a 100μm vessel) I can resolve the vessel in a trans-illumination geometry, which confirms a common experimental *in vivo* result (Fig 5.5.f)[14].

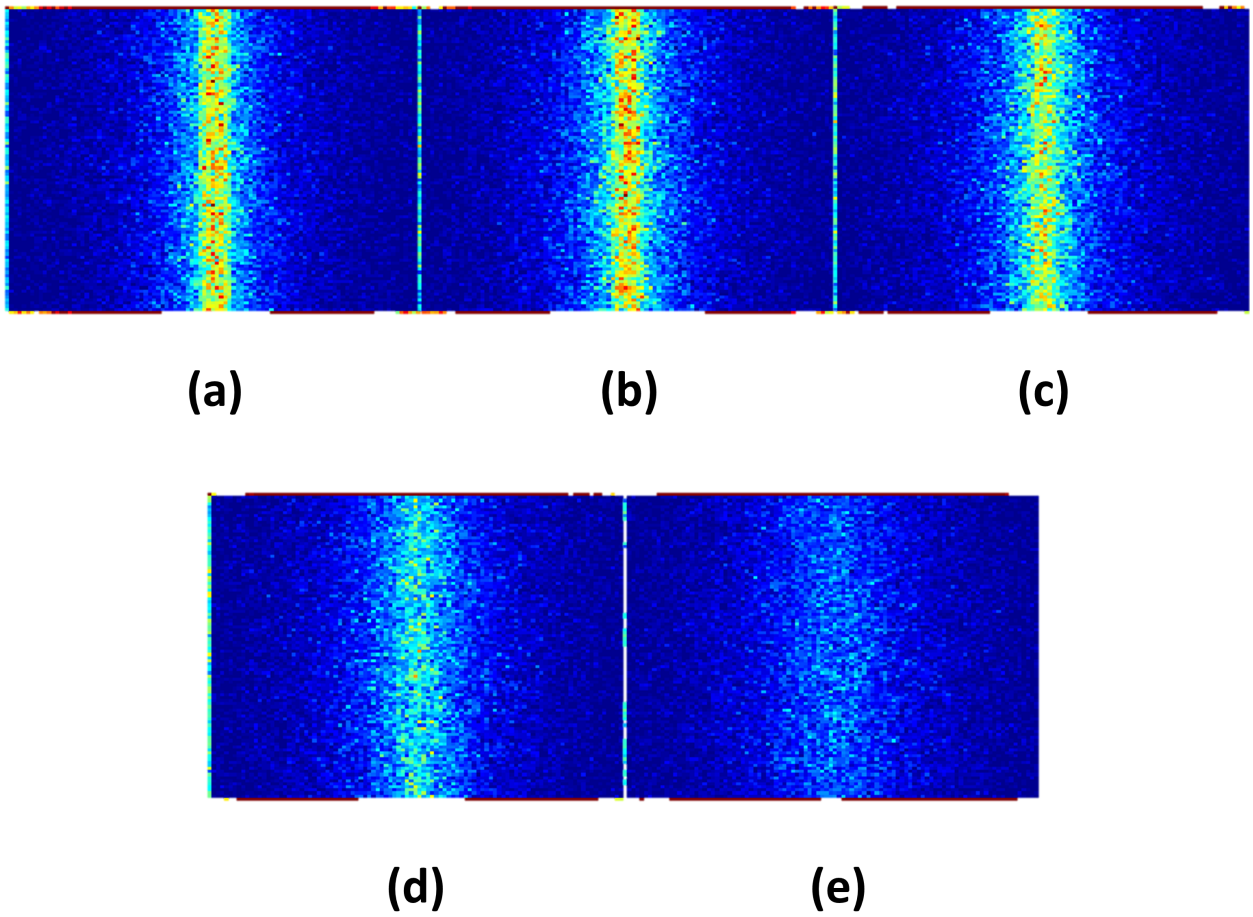

Figure 5.3: Reflected weighted momentum transfer for the thick (10mm) sample with a microchannel buried (a) 0μm, (b) 100μm, (c) 200μm, (d) 500μm, and (e) 1000μm below a static scattering layer. Increased lateral scattering of the photons results in decreased spatial resolution of the deeper vessels.

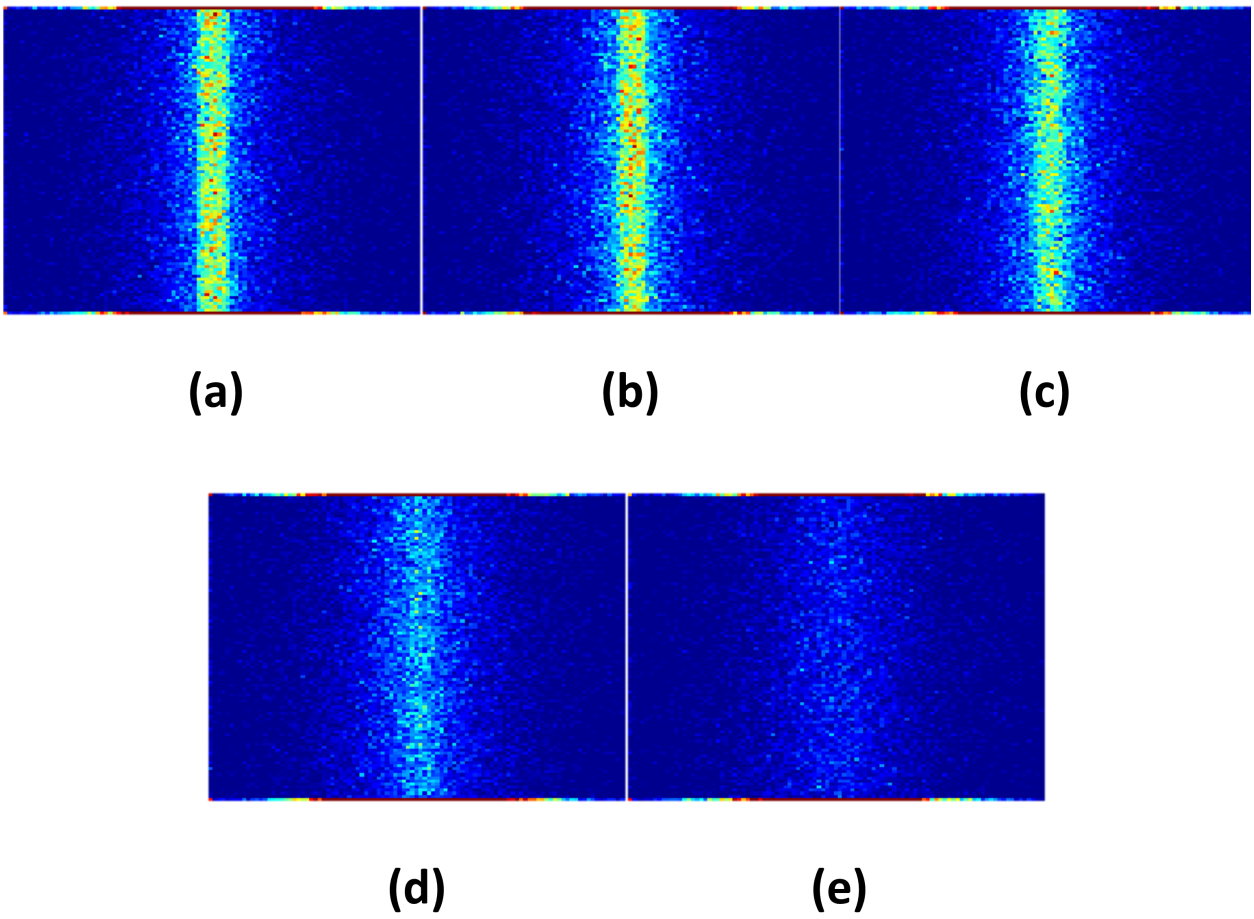

Figure 5.4: Reflected weighted momentum transfer for the thin (1.8mm) sample with a microchannel buried (a) 0μm, (b) 100μm, (c) 200μm, (d) 500μm, and (e) 1000μm below a static scattering layer. The results are similar to the thick sample, indicating that LSI may be performed in thin samples without the need for a thicker back-layer present.

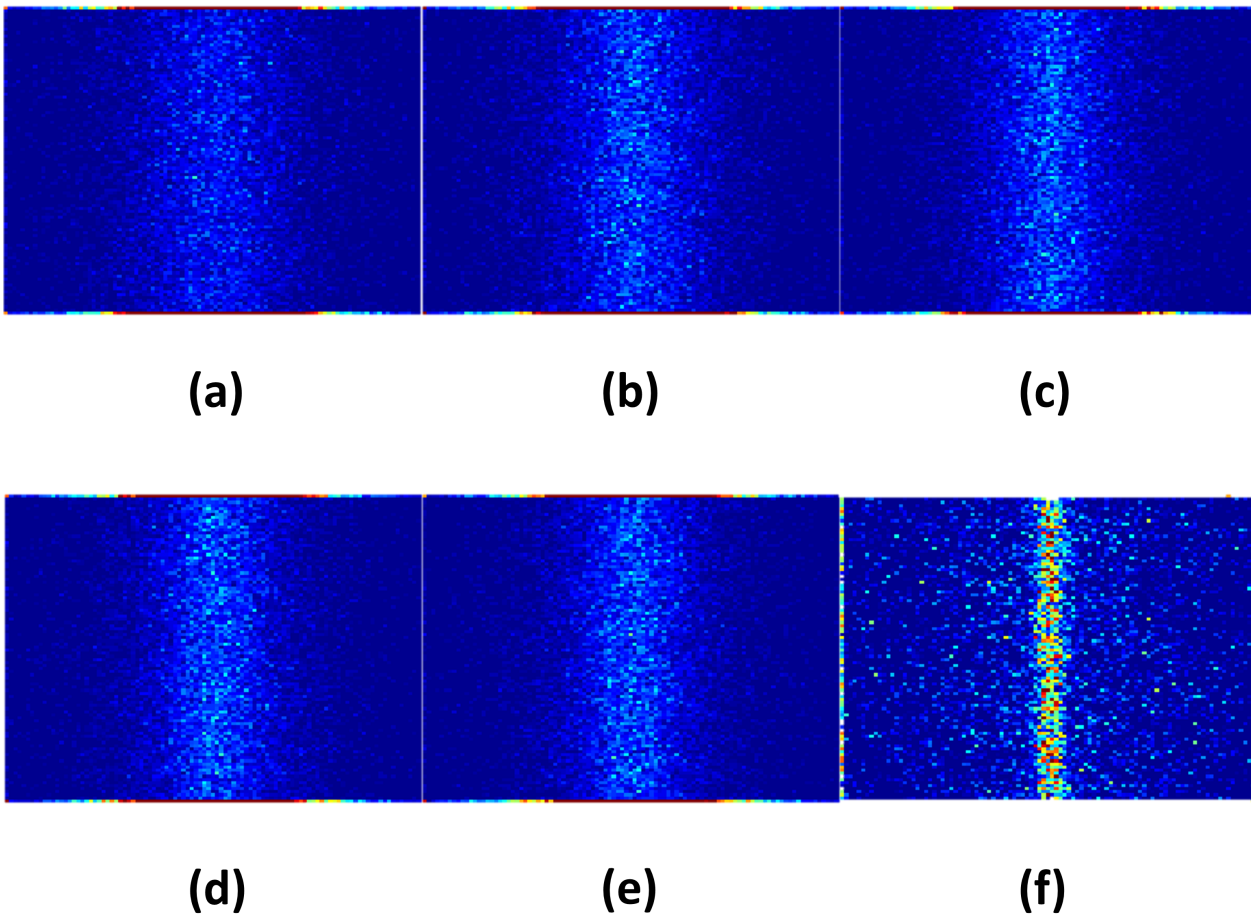

Figure 5.5: Transmitted weighted momentum transfer for the thin (1.8mm) sample with a microchannel buried (a) 0μm, (b) 100μm, (c) 200μm, (d) 500μm, and (e) 1000μm below a static scattering layer. Momentum transfer is reach the detector however most of the spatial information about its origin has been lost. (f) Transmitted weighted momentum transfer for a rodent dorsal window chamber geometry. A 300μm static layer is present above a 100μm diameter blood vessel.

5.3.3 Multi exposure LSI in a variable-depth tube

To simulate MESI, I computed contrast in the microchannel at 16 exposure times for a flow speed of 1mm/s (Fig 5.6). In the thicker sample geometry, the reflected contrast is lower, and has a greater dynamic range than the transmitted contrast (Fig 5.6.a). This is expected due to the increase in static scattering events for transmitted photons. Contrast of the 100μm depth vessel is lower than the surface vessel due to the fact that fluence and

reflected momentum transfer peak slightly below the surface (Fig 4.4.a), therefore more dynamic momentum transfer occurs at this depth than at the surface. The thinner sample geometry has similar reflected contrast curves, however the transmitted contrast is much lower (Fig 5.6.b). The contrast curves for corresponding vessel depths in epi- versus trans-illumination schemes (ie: 0/1000μm, 100/900μm, 200/800μm) are closer, which is expected because the light is traveling through similar relative amounts of static and dynamic regions.

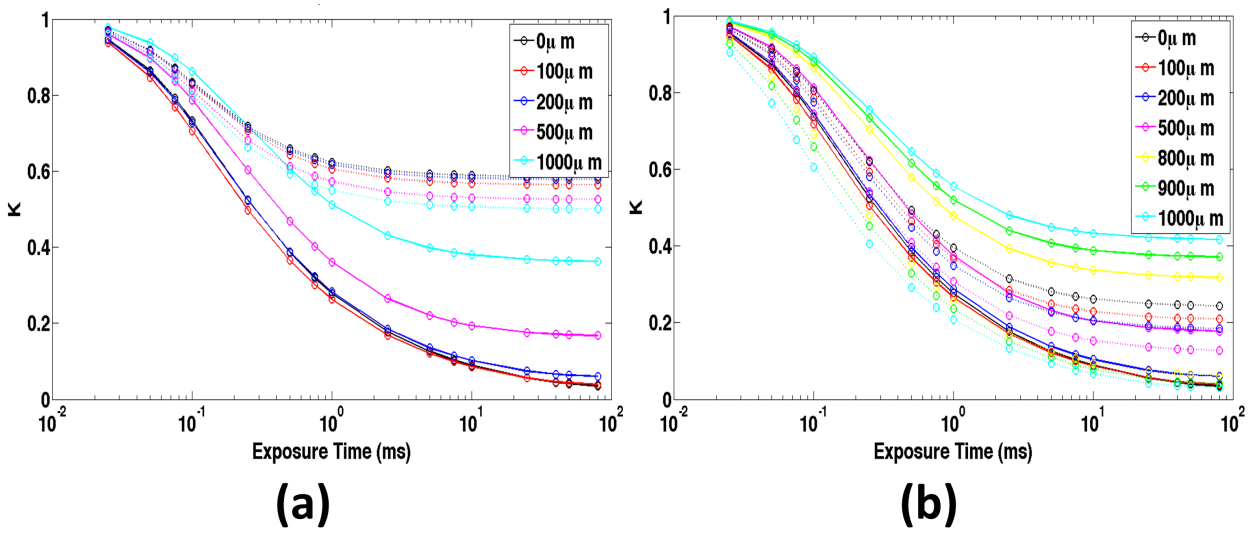

Figure 5.6: Simulated MESI experiment of a microchannel buried at varying depths below a static top layer. (a) Reflected (solid lines) and transmitted (dotted lines) speckle contrast versus exposure time in the thick (10mm) geometry. Transmitted contrast values are higher than reflected and have a greater non-ergodic offset due to the increased contribution from static scattering. (b) Reflected (solid lines) and transmitted (dotted lines) speckle contrast versus exposure time in the thin (1.8mm) geometry. Contrast values in both imaging geometries are similar with the reflectance versus trans-illuminated curves mirroring each other.

I fit the simulated MESI data to Eq. (5.1) (with the ν_{noise} term removed) and extracted the correlation time (τ_c), fraction of dynamically scattered light (ρ), and experimental constant (β) parameters. β is uniformly unity for all simulated results, which is expected because there are no experimental factors to decrease the theoretical dynamic range. Figure 5.7.a shows the inverse correlation time ($1/\tau_c$), which is proportional to

speed, as a function of speed for the buried vessels in a thicker geometry. As expected, $1/\tau_c$ increases linearly with speed, however it also decreases with increasing depth of the tube above 200μm. The 100μm deep tube had a higher inverse correlation time for the same reason it had lower contrast values described above. Previous studies indicated this technique resulted in greater quantitative accuracy of flow measurements in the presence of static scattering[19,127], however these data demonstrate that this does not hold for flow deeper than ~200μm. The values of $1/\tau_c$ in the trans-illumination geometry of thicker tissue are surprisingly consistent regardless of depth (Fig 5.7.c). Both epi- and trans-illumination of the thin tissue results in similar $1/\tau_c$ values as the epi-illuminated thick tissue (Fig 5.7.b, 5.7.d). This indicates potential for implementation of trans-illuminated MESI of thicker tissues to more accurately quantify flow if sufficient light can be collected at the lower exposure times.

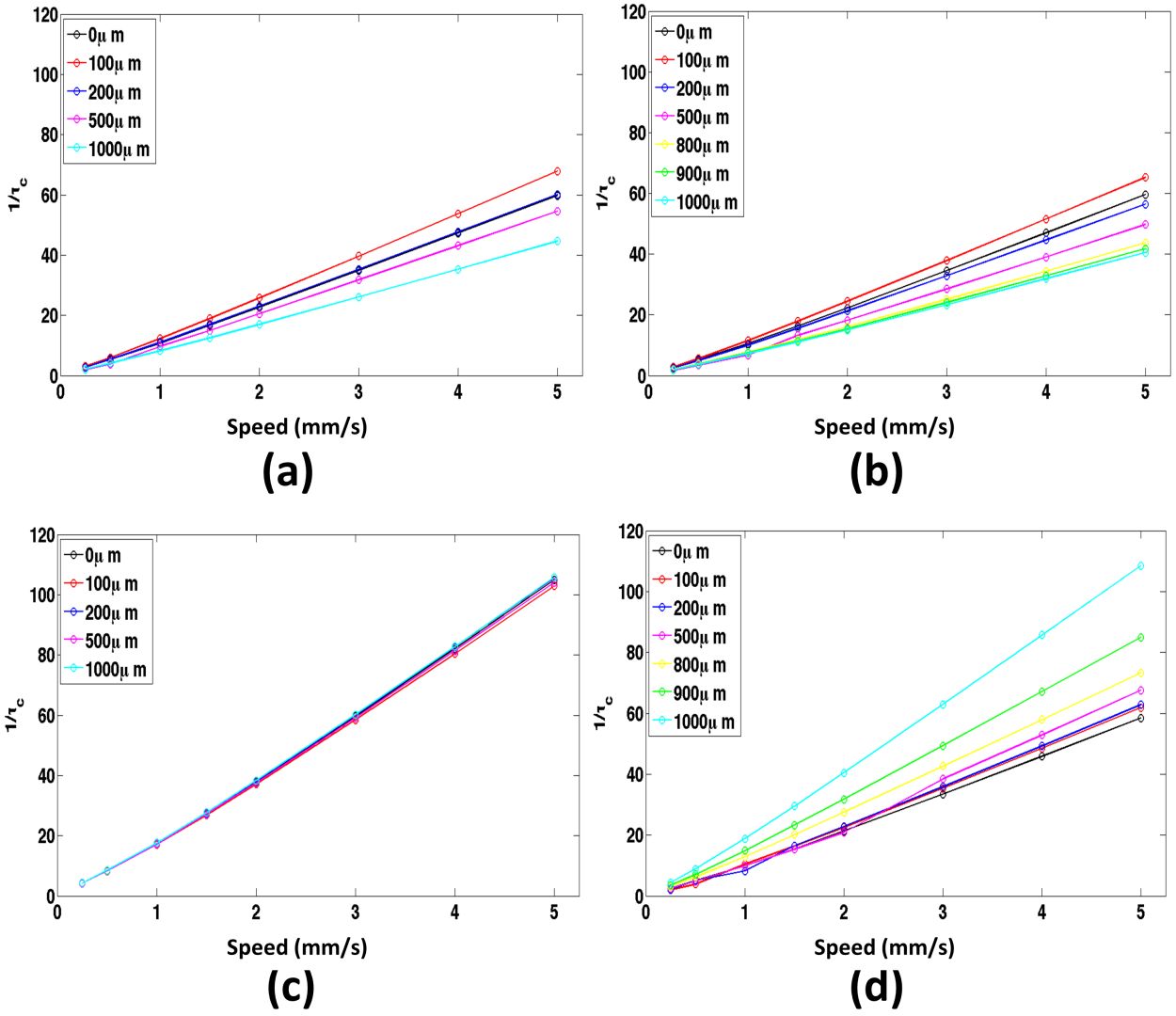

Figure 5.7: Simulated MESI fitting of the inverse correlation time ($1/\tau_c$) for blood flow in a microchannel buried at varying depths below a static top layer. (a) Reflectance MESI of the thick (10mm) sample. The $1/\tau_c$ values decrease with increasing static layer thickness, indicating that standard MESI is not immune to the effects of non-ergodic media. (b) Reflectance MESI of the thin (1.8mm) sample. (c). Trans-illumination MESI of the thick (10mm) sample has overlapping $1/\tau_c$ curves, indicating that this configuration may result in more accurate estimates of correlation time, and hence flow speed for flow in thick static scattering tissues. (d) Trans-illumination MESI of the thin (1.8 mm) sample is not immune to increases in static scattering.

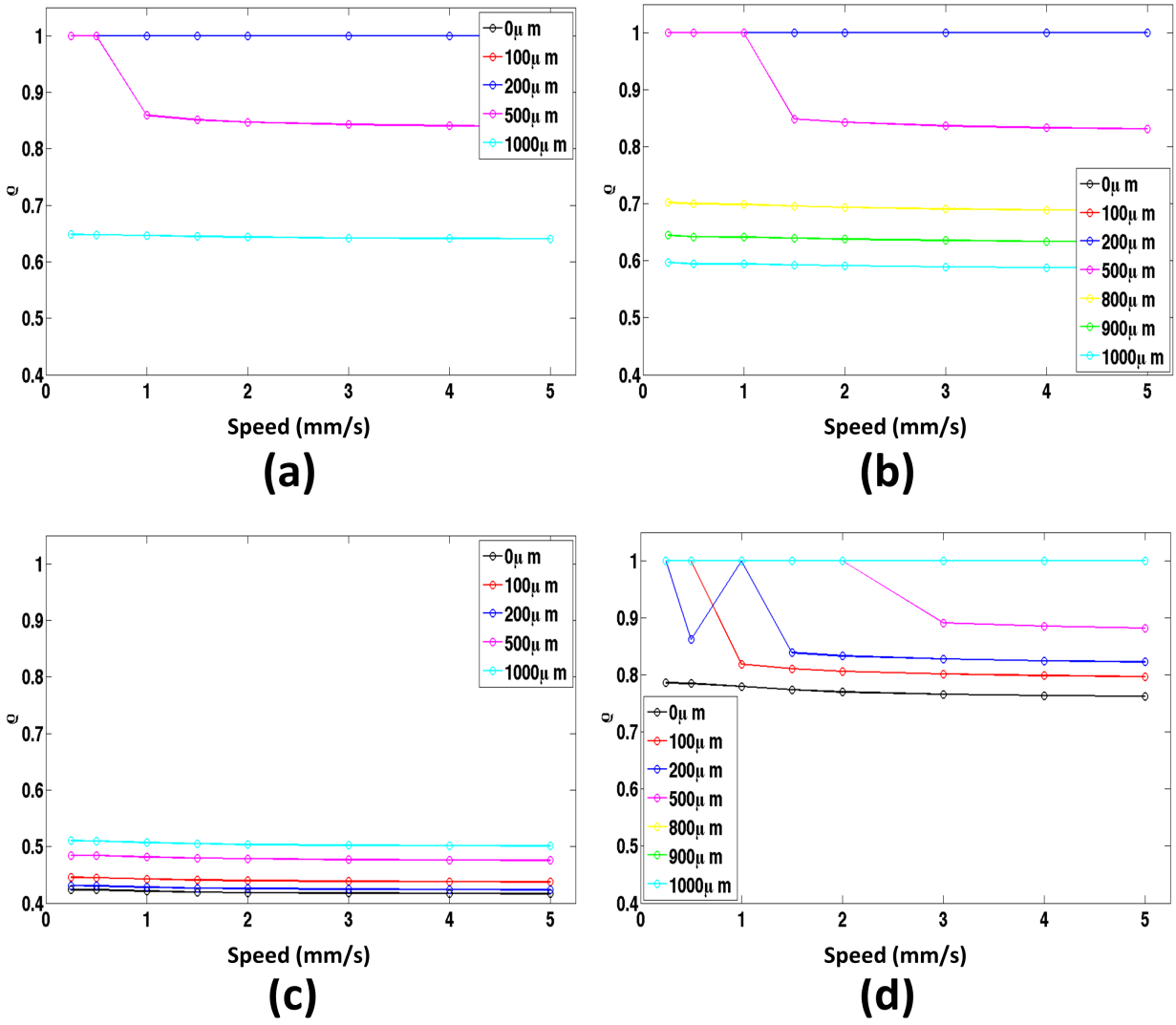

Figure 5.8: Simulated MESI fitting of the fraction of dynamically scattered light (ρ) for blood flow in a microchannel buried at varying depths below a static top layer. (a) Reflectance MESI of the thick (10mm) sample. The ρ values are unity for vessels shallower than 500μm. (b) Reflectance MESI of the thin (1.8mm) sample. (c). Trans-illumination MESI of the thick (10mm) sample has lower ρ values since the light has to travel through ~10mm of static media. (d) Trans-illumination MESI of the thin (1.8 mm) sample has ρ values slightly less than unity.

I also fit the ρ parameter, defined as the fraction of dynamically scattered light, from the simulated MESI data (Fig 5.8). The fit ρ value suggests that all of the light collected from the region of interest above the vessel had at least one dynamic scattering event when the tube was shallower than 200μm, and that even when the tube was at 1000μm, ~65% of the

reflected light interacted with it (Fig 5.8.a). These values decreased to ~40-50% for transmitted light (Fig 5.8.c). The reflected ρ parameter remained similar in the thin geometry, and was closer to unity in the trans-illuminated sample (Fig 5.8.b, 5.8.d).

I also calculated the actual fraction of light that had undergone at least one dynamic scattering event (Table 5.1, 5.2, Fig 5.9.a) using the Monte Carlo simulation. The fraction of dynamically scattered reflected light has a quadratic decrease as the vessel is buried deeper below the static layer. This may explain why the contrast values and inverse correlation times are not consistent for different depth vessels. However, it is interesting to note that the fraction is consistently ~20% for trans-illuminated light in the thicker tissue geometry, which may explain the consistent inverse correlation time measurements (Table 5.1). This data also suggests that the ρ parameter is more complex than simply the fraction of dynamically scattered light.

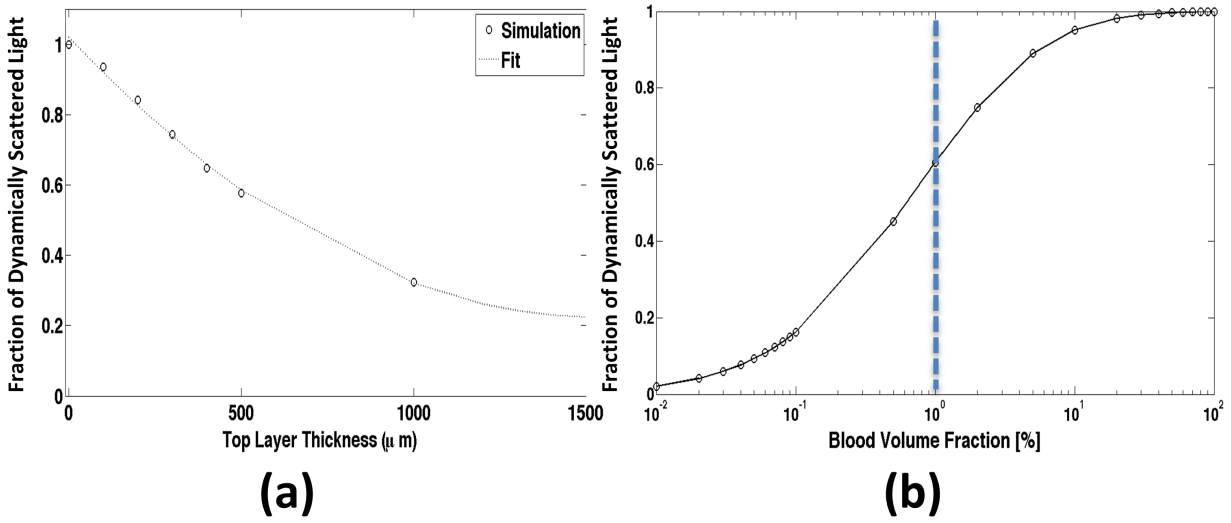

Figure 5.9: (a) True fraction of dynamically scattered reflected photons calculated directly from the Monte Carlo simulation of a vessel below varying thickness static top layers in a 10mm thick sample. Data is fit with a quadratic function, and shows that the true fraction is less than one when any static top layer is present. (b) True fraction of dynamically scattered reflected light in the homogeneous skin geometry. The dotted line at 1% blood volume represents where the ρ value fit from the MESI equation plateaus at one. This indicates that ρ is not actually equal to the of the fraction of dynamically scattered light or the fraction of dynamic scattering.

Table 5.1: True percentage of dynamically scattered reflected and transmitted photons calculated directly from the Monte Carlo simulation of a vessel below varying thickness static top layers in a 10mm thick sample.

Thickness of Top Layer (μm)	% Reflected Dynamic Scattering	% Transmitted Dynamic Scattering
0	100%	17.7%
100	93.6%	19.1%
200	84.2%	18.1%
300	74.4%	20.2%
400	64.7%	21.2%
500	57.6%	21.4%
1000	32.3%	23.1%

Table 5.2: True percentage of dynamically scattered reflected and transmitted photons calculated directly from the Monte Carlo simulation of a vessel below varying thickness static top layers in a 1.8mm sample.

Thickness of Top Layer (μm)	% Reflected Dynamic Scattering	% Transmitted Dynamic Scattering
0	100%	45.5%
100	93.8%	50.4%
200	84.1%	54.5%
500	55.5%	65.2%
800	26.3%	82.4%
900	31.0%	91.0%
1000	27.1%	100%

To compare the trends observed in the simulated data to experimental results, I performed *in vitro* MESI of flow in a vessel at various depths (Fig 5.10). The plot of $1/\tau_c$ versus flow speed showed a linear increase as flow increases, which is expected because the correlation time of the speckle pattern decreases as the movement of scattering particles, and hence the fluctuations in the speckle pattern increase. As the depth of the microchannel increases, the slope of the $1/\tau_c$ decreases (Fig 5.10.a). This is due to the increased presence of static scattering, which cannot be completely decoupled from the contrast signal, even with the MESI method. The experimental data is noisier due to motion artifacts and imperfections in the syringe pump, however the trends closely match those seen in the simulated data. I calculated the percent error in $1/\tau_c$ relative to the surface microchannel with no static scattering above the vessel for each of the buried vessels. Ideally, lower error means that that the estimation of flow in the tube (τ_c) is closer to the

true (no static scattering present) value. I observe less than 10% error when the tube is at a depth of 200μm, however the error increased beyond this. I found the same trend of increasing error as the tube was buried deeper, due to the increase in static scattering. The ρ value remains constant with speed, and decreases with increasing top layer thickness. The values of ρ are lower than the simulated data, which may be due to the fact that the 1% Intralipid solution has negligible absorption, as well as a large fraction of water. Therefore, a lot of the light may pass completely through the vessel and into the static region before being reflected. The β parameter is fairly low, however it is relatively independent of speed and vessel depth, which is expected.

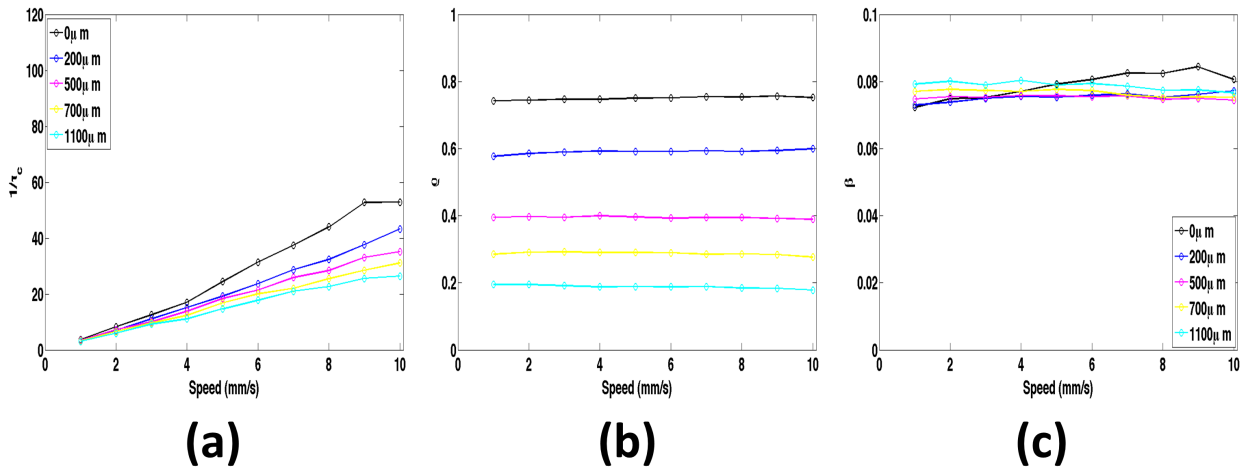

Figure 5.10: *In vitro* MESI data. (a) $1/\tau_c$ fit shows same decrease with increasing static top layer thickness seen in simulated data. (b) ρ parameter decreases with increasing amounts of static scattering which is expected. (c) β values are relatively consistent regardless of top layer, which is expected.

5.3.4 Relationship between blood volume fraction, ρ and τ_c

To further explore the relationship between ρ, τ_c, and the fraction of dynamic scattering present in a sample, I used a homogeneous simulated geometry with optical properties similar to the dermal layer of skin, and various blood volume fractions. The

blood volume fraction (BVF) is equivalent to the fraction of scattering events that are dynamic.

To study the relationship between blood volume fraction, correlation time (τ_c), and the ρ term, defined as the fraction of dynamically scattered light, I fit simulated data to Eq. (5.1) (with the ν_{noise} term removed) at eight different flow speeds. For each blood volume fraction and flow speed, β is unity. This is expected because in the simulation there are no experimental factors that reduce the maximum possible contrast value.

Figure 5.11.a shows the ρ term as a function of blood volume fraction and speed of the dynamic scatterers. Generally, the ρ value is constant across different flow speeds; there is a very slight decrease as speed increases (mean ΔK = .03 between speeds 0.1 and 10mm/s, mean ΔK = 0.25 between speeds 0.01 and 10mm/s). The ρ term plateaus at unity at 1% blood volume (dashed line), except for the slowest and fastest flows speeds (0.01mm/s and 10mm/s) for which the plateau occurs at 0.5% and 2% respectively. According to the definition of ρ, as the fraction of dynamically scattered light, or the fraction of photons where at least one scattering event was dynamic, ρ values of unity should indicate that every photon encountered at least one dynamic scattering event. However, the Monte Carlo simulation tracks the fraction of photons that have undergone at least one dynamic scattering event, and this fraction is only ~60% when ρ plateaus at unity (Fig 5.9.b). Similar to the microchannel simulations described above, this suggests that the relationship between ρ and fraction of dynamic scattering may be more complex.

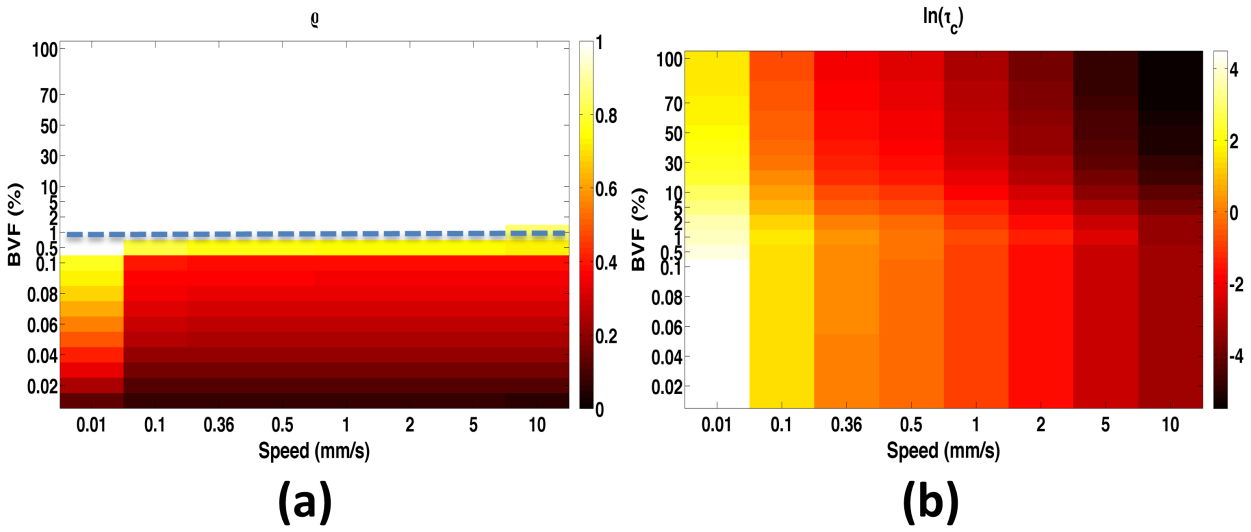

Figure 5.11: *In silico* MESI data of homogeneous skin sample. (a) ρ parameter obtained from MESI fitting plateaus at unity at a blood volume fraction of 1%. (b) I expected the $\ln(\tau_c)$ fit to be constant for a given speed, however it decreases with increasing blood volume fraction above BVF = 1% once ρ plateause at unity.

Figure 5.11.b shows the natural log of the correlation time, τ_c, for each blood volume fraction and flow speed. For a given blood volume fraction, the correlation time decreases as speed increases, which is in agreement with speckle theory. Light that has interacted with particles that are moving quickly will decorrelate more than light scattered from slow moving particles.

The initial hypothesis was that correlation time should be constant with blood volume fraction; however, this is not what was observed. For low blood volume fractions (0.01%-0.1%), the correlation time increased slightly with increasing blood volume fraction (mean $\Delta\tau_c = 0.19$). At blood fractions greater than 0.1%, the correlation time decreased as blood volume fraction increased to 100% (mean $\Delta\tau_c = 1.18$). The inflection point at which τ_c switched from decreasing to increasing occurred at the same point where the ρ term plateaued at unity (dashed line, Fig 5.11.a). Due to this fact, I hypothesize that there maybe be crosstalk between the ρ term and the fit for τ_c. Therefore, once ρ reaches a

plateau at unity, the correlation time begins to decrease as the blood volume fraction increases making it appear as though there is an increased decorrelation of the signal.

To study how robust the MESI model is to experimental noise, I added 1% Gaussian white noise to the contrast values at each flow speed and exposure time, and fit the noisy data with Eq. (5.1) (with the ν_{noise} term removed). The average absolute value of percent error in the fitted correlation time of the noisy data compared to the data with no noise was 5.12%; 54.17% of the data points have error below 5%, and 85.42% have error below 10%. The data points with the greatest error are generally the low blood volume fraction data points (<0.07% blood volume); the 10mm/s data also has higher percent error in the fit compared to the other data, probably because the dynamic range of the correlation time is low at this high speed. The ρ term has an average percent error of 1.52% (3.22% when ignoring ρ = 1 values). The largest error occurs for the data at the lowest speed and blood volume fraction. Overall, this data suggests that the model is fairly robust to noise in the contrast values, although care should be taken when measuring samples with very low blood volume fractions, or extreme speeds.

To study the effect of reduced scattering on terms fit from the MESI model, I ran the same simulations at select blood volume fractions with μ_s' lowered from 2.296mm^{-1} to 0.5mm^{-1}. Figure 5.12 shows the percent difference in these parameters compared to samples with normal scattering. The correlation time is ~20-60% greater for the samples with lower scattering (Fig 5.12.a). This is expected because each photon will undergo less dynamic scattering events, therefore they will have less phase change. The ρ term now plateaus at ~2% instead of 1% blood volume (dashed line, Fig 5.12.b). It is ~23-67% less than samples with the normal scattering coefficient. This data supports the previous claim

that ρ cannot be directly proportional to blood volume fraction, as changing the total scattering without changing the blood volume fraction should not have an effect on ρ.

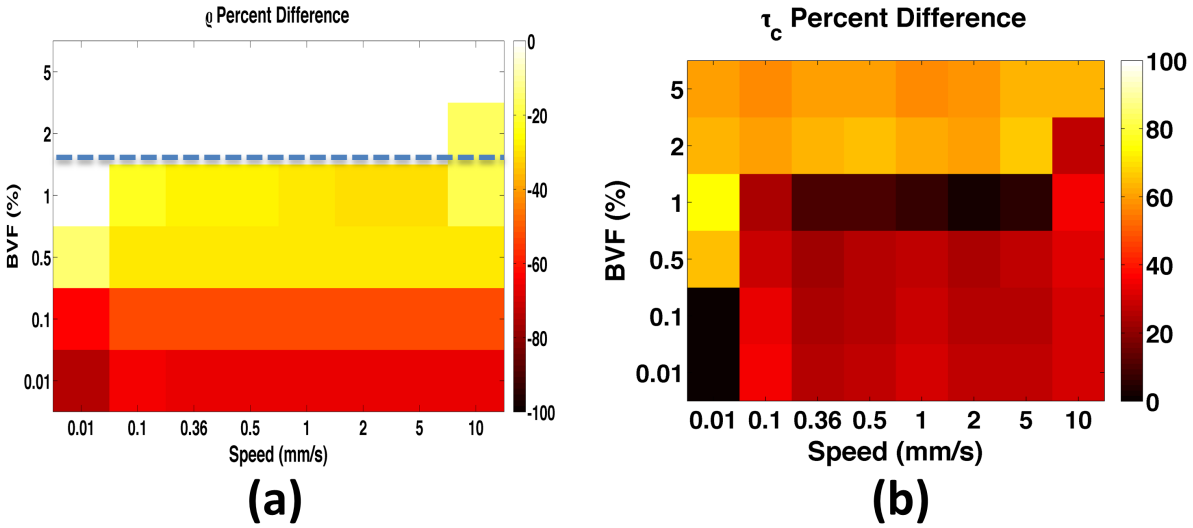

Figure 5.12: *In silico* MESI data of homogeneous skin sample with decreased μ_s'. (a) The percent difference in the fitted ρ parameter between normal and decreased μ_s'. A lower μ_s' raises the BVF where ρ plateaus by ~1%. This indicates that ρ is not directly proportional to the percentage of dynamic scattering events (BVF). (b) The fit of τ_c increased by ~20-60% due to the decrease in total scattering events; this results in less phase change and hence less decorrelation of the photons.

To assess whether the presence of a thin, statically scattering layer, such as the epidermis had an effect on the fitted parameters, I ran simulations with a 75μm static epidermis above the 10mm sample. I found that the correlation times for different speeds and blood volume fractions were similar between samples with and without the epidermal layer (~4-18% difference). Since the epidermal layer is optically thin, I postulate that its presence does not appreciably change the quantity of dynamic scattering undergone by each photon. The ρ value reached a plateau at a slightly higher blood volume fraction (2%) at higher speeds (≥0.5mm/s). This may indicate that using MESI to quantify a ρ value *in vivo* is better suited for tissues such as the brain, for which the flow speeds are faster and static scattering layer (i.e., the skull) thicker than those found in the skin[129].

5.4 Conclusions

In summary, I simulated single and multi-exposure LSI of a buried vessel to study the locations at which the signal originates in depth, and why spatial visualization of vessels is limited to ~200μm in depth. I showed that momentum transfer arising from deeper vasculature is laterally blurred to a large degree before the associated photons exit the tissue, limiting the spatial resolution of vessels using LSI. With application of Monte Carlo modeling to study of MESI, I found that the increase in superficial static scattering affects the quantitative accuracy of MESI. Trans-illumination MESI through a thicker tissue may be resistant to this effect. Furthermore, I showed that the ρ parameter surprisingly does not accurately represent either the fraction of dynamically scattered light, or the fraction of dynamic scatterers in the tissue.

5.5 Acknowledgements

The Monte Carlo simulations in this work would not have been possible without Dr Carole Hayakawa and the Virtual Photonics Initiative. Additionally, I would like to thank Christian Crouzet for building, testing, and gathering *in vitro* data with the experimental MESI system.

REFERENCES

1. Boas DA, Dunn AK. Laser speckle contrast imaging in biomedical optics. *J Biomed Opt*. 2010;15(1):11109. doi:10.1117/1.3285504.

2. Yang B, Yang O, Guzman J, et al. Intraoperative, real-time monitoring of blood flow dynamics associated with laser surgery of port wine stain birthmarks. *Lasers Surg Med*. 2015;47(6):469-475. doi:10.1002/lsm.22369.

3. Dunn AK, Bolay H, Moskowitz MA, Boas DA. Dynamic imaging of cerebral blood flow using laser speckle. *J Cereb Blood Flow Metab*. 2001;21(3):195-201. doi:10.1097/00004647-200103000-00002.

4. Fercher AF, Briers JD. Flow visualization by means of single-exposure speckle photography. *Opt Commun*. 1981;37(5):326-330. doi:10.1016/0030-4018(81)90428-4.

5. Li P, Ni S, Zhang L, Zeng S, Luo Q. Imaging cerebral blood flow through the intact rat skull with temporal laser speckle imaging. *Opt Lett*. 2006;31(12):1824-1826.

6. Ramirez-San-Juan JC, Regan C, Coyotl-Ocelotl B, Choi B. Spatial versus temporal laser speckle contrast analyses in the presence of static optical scatterers. *J Biomed Opt*. 2014;19(10):106009. doi:10.1117/1.JBO.19.10.106009.

7. Briers JD, Duncan DD, Hirst E, et al. Laser speckle contrast imaging: theoretical and practical limitations. *J Biomed Opt*. 2013;18(6):66018. doi:10.1117/1.

8. Briers JD. Time-varying laser speckle for measuring motion and flow. *Proc SPIE*. 2001;4242:25-39. doi:10.1117/12.427758.

9. Sturesson C, Milstein DMJ, Post ICJH, Maas AM, Van Gulik TM. Laser speckle contrast imaging for assessment of liver microcirculation. *Microvasc Res*. 2013;87:34-40. doi:10.1016/j.mvr.2013.01.004.

10. Huang Y-C, Ringold TL, Nelson JS, Choi B. Noninvasive blood flow imaging for real-time feedback during laser therapy of port wine stain birthmarks. *Lasers Surg Med*. 2008;40(3):167-173. doi:10.1002/lsm.20619.

11. Jia W, Tran N, Sun V, et al. Photocoagulation of dermal blood vessels with multiple laser pulses in an in vivo microvascular model. *Lasers Surg Med*. 2012;44(2):144-151. doi:10.1002/lsm.22000.

12. Moy WJ, Patel SJ, Lertsakdadet BS, et al. Preclinical in vivo evaluation of Npe6-mediated photodynamic therapy on normal vasculature. *Lasers Surg Med*. 2012;44(2):158-162. doi:10.1002/lsm.21155.

13. Crouzet C, Wilson RH, Bazrafkan A, et al. Cerebral blood flow is decoupled from blood pressure and linked to EEG bursting after resuscitation from cardiac arrest. *Biomed Opt Express*. 2016;7(11):4660. doi:10.1364/BOE.7.004660.

14. Moy AJ, White SM, Indrawan ES, et al. Wide-field functional imaging of blood flow and hemoglobin oxygen saturation in the rodent dorsal window chamber. *Microvasc Res*. 2011;82(3):199-209. doi:10.1016/j.mvr.2011.07.004.

15. Qiu J, Li P, Luo W, Wang J, Zhang H, Luo Q. Spatiotemporal laser speckle contrast analysis for blood flow imaging with maximized speckle contrast. *J Biomed Opt*. 2010;15(1):16003. doi:10.1117/1.3290804.

16. Liu R, Qin J, Wang RK. Motion-contrast laser speckle imaging of microcirculation within tissue beds in vivo. *J Biomed Opt*. 2013;18(6):60508. doi:10.1117/1.JBO.18.6.060508.

17. Kim J, Oh J, Choi B. Magnetomotive laser speckle imaging. *J Biomed Opt*. 2010;15(1):11110. doi:10.1117/1.3285612.

18. Ramirez-San-Juan JC, Mendez-Aguilar E, Salazar-Hermenegildo N, Fuentes-Garcia a, Ramos-Garcia R, Choi B. Effects of speckle/pixel size ratio on temporal and spatial speckle-contrast analysis of dynamic scattering systems: Implications for measurements of blood-flow dynamics. *Biomed Opt Express*. 2013;4(10):1883-1889. doi:10.1364/BOE.4.001883.

19. Parthasarathy AB, Tom WJ, Gopal A, Zhang X, Dunn AK. Robust flow measurement with multi-exposure speckle imaging. *Opt Express*. 2008;16(3):1975-1989. doi:10.1364/OE.16.001975.

20. Stoianovici C, Wilder-Smith P, Choi B. Assessment of pulpal vitality using laser speckle imaging. *Lasers Surg Med*. 2011;43(8):833-837. doi:10.1002/lsm.21090.

21. Fried D, Glena RE, Featherstone JD, Seka W. Nature of light scattering in dental enamel and dentin at visible and near-infrared wavelengths. *Appl Opt*. 1995;34(7):1278-1285. doi:10.1364/AO.34.001278.

22. Kakino S, Takagi Y, Takatani S. Absolute transmitted light plethysmography for assessment of dental pulp vitality through quantification of pulp chamber hematocrit by a three-layer model. *J Biomed Opt*. 2008;13(5):54023. doi:10.1117/1.2976112.

23. Chen E, Abbott P V. Dental pulp testing: a review. *Int J Dent*. 2009;2009(iii):365785. doi:10.1155/2009/365785.

24. Gopikrishna V, Pradeep G, Venkateshbabu N. Assessment of pulp vitality: A review. *Int J Paediatr Dent*. 2009;19(1):3-15. doi:10.1111/j.1365-263X.2008.00955.x.

25. Jacques SL. Role of tissue optics and pulse duration on tissue effects during high-power laser irradiation. *Appl Opt*. 1993;32(13):2447-2454. doi:10.1364/AO.32.002447.

26. Li B, Majaron B, Viator J a., et al. Accurate measurement of blood vessel depth in port wine stained human skin in vivo using pulsed photothermal radiometry. *J Biomed Opt*. 2004;9(5):961-966. doi:10.1117/1.1784470.

27. Telenkov SA, Tanenbaum BS, Goodman DM, Nelson JS, Milner TE. In vivo infrared

tomographic imaging of laser-heated blood vessels. *IEEE J Sel Top Quantum Electron*. 1999;5(4):1193-1199. doi:10.1109/2944.796346.

28. Choi B, Majaron B, Nelson JS. Computational model to evaluate port wine stain depth profiling using pulsed photothermal radiometry. *J Biomed Opt*. 2004;9(2):299-307. doi:10.1117/1.1646173.

29. Milanic M, Majaron B. Pulsed photothermal depth profiling of tattoos undergoing laser removal treatment. 2012;8207:82070G. doi:10.1117/12.908407.

30. Choi B, Majaron B, Vargasc G, et al. In Vivo Results Using Photothermal Tomography for Imaging Cutaneous Blood Vessels. 5047(2003):350-361.

31. Regan C, Ramirez-San-Juan JC, Choi B. Photothermal laser speckle imaging. *Opt Lett*. 2014;39(17):5006-5009. doi:10.1364/OL.39.005006.

32. Wang L V, Wu H. *Biomedical Optics: Principles and Imaging*. Hoboken: Wiley; 2007.

33. Nilsson A, Lucassen G, Verkruysse W, Andersson-Engels S, van Gemert M. Changes in optical properties of human whole blood in vitro due to slow heating. *Photochem Photobiol*. 1997;65(2):366-373.

34. Randeberg L, Daae Hagen A, Svaasand L. Optical Properties of Human Blood as a Function of Temperature. 2002;4609:20-28.

35. Regan C, Choi B. Laser speckle imaging based on photothermally driven convection. *J Biomed Opt*. 2016;21(2):26011. doi:10.1117/1.JBO.21.2.026011.

36. Prahl SA, Keijzer M, Jacques SL, Welch AJ. Monte-Carlo model of light propagation in tissue. *SPIE Inst Ser*. 1989;IS(5):102-111. doi:10.1.1.132.5731.

37. Wang, L., Jacques, S. L., & Zheng L. MCML - Monte Carlo modeling of light transport in multi-layered tissues. *Comput Methods Programs Biomed*. 1995;47(2):131-146. doi:10.1007/978-1-4757-6092-7_4.

38. Prahl S. Oregon Medical Laser Center: Monte Carlo Simulations. http://omlc.org/software/mc/. Published 2007.

39. Laser Microbeam and Medical Program. Virtual Photonics Technology Initiative. http://www.virtualphotonics.org/. Published 2014.

40. Hayakawa C, Spanier J, Venugopalan V. Computational Engine for a Virtual Tissue Simulator. In: Keller A, Heinrich S, Niederreiter H, eds. *Monte Carlo and Quasi-Monte Carlo Methods 2006*. Heidelberg: Springer, Berlin; 2008.

41. Davis MA, Dunn AK. Dynamic light scattering Monte Carlo: a method for simulating time-varying dynamics for ordered motion in heterogeneous media. *Opt Express*. 2015;23(13):17145-17155. doi:10.1364/OE.23.017145.

42. Rice TB, Konecky SD, Mazhar A, et al. Quantitative determination of dynamical

properties using coherent spatial frequency domain imaging. *J Opt Soc Am A Opt Image Sci Vis*. 2011;28(10):2108-2114. doi:10.1364/JOSAA.28.002108.

43. Boas DA, Yodh AG. Spatially varying dynamical properties of turbid media probed with diffusing temporal light correlation. *J Opt Soc Am A*. 1997;14(1):192-215. doi:10.1364/JOSAA.14.000192.

44. Rice TB, Kwan E, Hayakawa CK, Durkin AJ, Choi B, Tromberg BJ. Quantitative, depth-resolved determination of particle motion using multi-exposure, spatial frequency domain laser speckle imaging. *Biomed Opt Express*. 2013;4(12):2880-2892. doi:10.1364/BOE.4.002880.

45. Brenner M, Hearing VJ. The Protective Role of Melanin Against UV Damage in Human Skin. *Photochem Photobiol*. 2008;84(3):539-549. doi:10.1111/j.1751-1097.2007.00226.x.

46. Lister T, Wright PA, Chappell PH. Optical properties of human skin. *J Biomed Opt*. 2012;17(9):909011. doi:10.1117/1.JBO.17.9.090901.

47. Jacques SL, McAuliffe DJ. the Melanosome: Threshold Temperature for Explosive Vaporization and Internal Absorption Coefficient During Pulsed Laser Irradiation. *Photochem Photobiol*. 1991;53(6):769-775. doi:10.1111/j.1751-1097.1991.tb09891.x.

48. Yudovsky D, Durkin AJ. Spatial frequency domain spectroscopy of two layer media. *J Biomed Opt*. 2011;16(10):107005. doi:10.1117/1.3640814.

49. Lister T, Wright P, Chappell P. Spectrophotometers for the clinical assessment of port-wine stain skin lesions: A review. *Lasers Med Sci*. 2010;25(3):449-457. doi:10.1007/s10103-009-0726-8.

50. Choi B, Kang NM, Nelson JS. Laser speckle imaging for monitoring blood flow dynamics in the in vivo rodent dorsal skin fold model. *Microvasc Res*. 2004;68(2):143-146. doi:10.1016/j.mvr.2004.04.003.

51. Tamaki Y, Araie M, Kawamoto E, Eguchi S, Fujii H. Noncontact, two-dimensional measurement of retinal microcirculation using laser speckle phenomenon. *Investig Ophthalmol Vis Sci*. 1994;35(11):3825-3834. doi:10.1016/0030-4018(81)90428-4.

52. Yaoeda K, Shirakashi M, Funaki S, et al. Measurement of microcirculation in the optic nerve head by laser speckle flowgraphy and scanning laser Doppler flowmetry. *Am J Opthalmology*. 2000;129(6):734-739.

53. Riva C, Ross B, Benedek GB. Laser Doppler measurements of blood flow in capillary tubes and retinal arteries. *Invest Ophthalmol*. 1972;11(11):936-944. http://www.ncbi.nlm.nih.gov/pubmed/4634958%5Cnhttp://www.iovs.org/cgi/pmidlookup?view=long&pmid=4634958%5CnAll Papers/R/Riva et al. 1972 - Laser Doppler measurements of blood flow in capillary tubes and retinal arteries.pdf.

54. Bandyopadhyay R, Gittings AS, Suh SS, Dixon PK, Durian DJ. Speckle-visibility

spectroscopy: A tool to study time-varying dynamics. *Rev Sci Instrum*. 2005;76(9). doi:10.1063/1.2037987.

55. Kirkpatrick SJ, Duncan DD, Wells-Gray EM. Detrimental effects of speckle-pixel size matching in laser speckle contrast imaging. *Opt Lett*. 2008;33(24):2886. doi:10.1364/OL.33.002886.

56. Thompson O, Andrews M, Hirst E. Correction for spatial averaging in laser speckle contrast analysis. *Biomed Opt Express*. 2011;2(4):1021-1029. doi:10.1364/BOE.2.001021.

57. Ramirez-San-Juan JC, Ramos-Garcia R, Martinez-Niconoff G, Choi B. Simple correction factor for laser speckle imaging of flow dynamics. *Opt Lett*. 2014;39(3):678-681. doi:10.1364/OL.39.000678.

58. Draijer M, Hondebrink E, Van Leeuwen T, Steenbergen W. Review of laser speckle contrast techniques for visualizing tissue perfusion. *Lasers Med Sci*. 2009;24(4):639-651. doi:10.1007/s10103-008-0626-3.

59. Briers JD, Webster S. Quasi real-time digital version of single-exposure speckle photography for full-field monitoring of velocity or flow fields. *Opt Commun*. 1995;116(1-3):36-42. doi:10.1016/0030-4018(95)00042-7.

60. Cheng H, Luo Q, Zeng S, Chen S, Cen J, Gong H. Modified laser speckle imaging method with improved spatial resolution. *J Biomed Opt*. 2003;8(3):559-564. doi:10.1117/1.1578089.

61. Cheng H, Yumei Y, Duong TQ. Temporal statistical analysis of laser speckle images and its application to retinal blood-flow imaging. *Opt Express*. 2008;16(14):10214-10219. doi:10.1124/dmd.107.016501.CYP3A4-Mediated.

62. Saager RB, Kondru C, Au K, Sry K, Ayers F, Durkin AJ. Multilayer silicone phantoms for the evaluation of quantitative optical techniques in skin imaging. *SPIE 7567, Des Perform Valid Phantoms Used Conjunction with Opt Meas Tissue II*. 2010;7567:756706-756706-756708. doi:10.1117/12.842249.

63. Nadkarni S, Bouma BE, Yelin D, Gulati A, Tearney GJ. Laser speckle imaging of atherosclerotic plaques through optical fiber bundles. *J Biomed Opt*. 2008;13(5):54016. doi:10.1117/1.2982529.Laser.

64. Dunn JF, Forrester KR, Martin L, Tulip J, Bray RC. A transmissive laser speckle imaging technique for measuring deep tissue blood flow: An example application in finger joints. *Lasers Surg Med*. 2011;43(1):21-28. doi:10.1002/lsm.21018.

65. Mazhar A, Dell S, Cuccia DJ, et al. Wavelength optimization for rapid chromophore mapping using spatial frequency domain imaging. *J Biomed Opt*. 2010;15(6):61716. doi:10.1117/1.3523373.

66. Regan C, Yang BY, Mayzel KC, Ramirez-San-Juan JC, Wilder-Smith P, Choi B. Fiber-based laser speckle imaging for the detection of pulsatile flow. *Lasers Surg Med*.

2015;47(6). doi:10.1002/lsm.22370.

67. Mythri H, Arun A, Chachapan D. Pulp vitality tests - an overview on comparison of sensitivity and vitality. *Indian J Oral Sci*. 2015;6(2):41. doi:10.4103/0976-6944.162622.

68. Chambers IG. The role and methods of pulp testing in oral diagnosis: a review. *Int Endod J*. 1982;15(1):1-15. doi:10.1111/j.1365-2591.1982.tb01331.x.

69. Gazelius B, Olgart L, Edwall B, Edwall L. Non-invasive recording of blood flow in human dental pulp. *Endod Dent Traumatol*. 1986;2(5):219-221.

70. Miwa Z, Ikawa M, Iijima H, Saito M, Takagi Y. Pulpal blood flow in vital and nonvital young permanent teeth measured by transmitted-light photoplethysmography: a pilot study. *Pediatr Dent*. 2002;24(6):594-598.

71. Karayilmaz H, Kirzioğlu Z. Comparison of the reliability of laser Doppler flowmetry, pulse oximetry and electric pulp tester in assessing the pulp vitality of human teeth. *J Oral Rehabil*. 2011;38(5):340-347. doi:10.1111/j.1365-2842.2010.02160.x.

72. Bassi GS, Humphris GM, Longman LP. The etiology and management of gagging: A review of the literature. *J Prosthet Dent*. 2004;91(5):459-467. doi:10.1016/j.prosdent.2004.02.018.

73. Pierce M, Yu D, Richards-Kortum R. High-resolution fiber-optic microendoscopy for in situ cellular imaging. *J Vis Exp*. 2011;(47):e2306. doi:10.3791/2306.

74. Ayers F, Grant A, Kuo D, Cuccia DJ, Durkin AJ. Fabrication and characterization of silicone-based tissue phantoms with tunable optical properties in the visible and near infrared domain. *Proc SPIE*. 2008;6870:7-1-7-9. doi:10.1117/12.764969.

75. Yoon M-J, Kim E, Lee S-J, Bae Y-M, Kim S, Park S-H. Pulpal blood flow measurement with ultrasound Doppler imaging. *J Endod*. 2010;36(3):419-422. doi:10.1016/j.joen.2009.12.031.

76. Kannel WB, Kannel C, Paffenbarger RS, Cupples LA. Heart rate and cardiovascular mortality: The Framingham study. *Am Heart J*. 1987;113(6):1489-1494. doi:10.1016/0002-8703(87)90666-1.

77. Fulling H, Andreasen JO. Influence of maturation status and tooth type of permanei teeth upon electrometric and thermal pulp testing. *Eur J Oral Sci*. 1976;84(5):286-290. doi:10.1111/j.1600-0722.1976.tb00491.x.

78. Regan C, White SM, Yang BY, et al. Design and evaluation of a miniature laser speckle imaging device to assess gingival health. *J Biomed Opt*. 2016;21(10):104002-104002. doi:10.1117/1.JBO.21.10.104002.

79. Newman M, Takei H, Klokkevold P, Carransa F. *Carranza's Clinical Periodontology*. 11th ed. Elsevier/Saunders; 2012.

80. Parfitt GJ. A Five Year Longitudinal Study of the Gingival Condition of a Group of

Children in England. *J Periodontol*. 1957;28(1):26-32. doi:10.1902/jop.1957.28.1.26.

81. Zoellner H, Chapple CC, Hunter N. Microvasculature in gingivitis and chronic periodontitis: Disruption of vascular networks with protracted inflammation. *Microsc Res Tech*. 2002;56(1):15-31. doi:10.1002/jemt.10009.

82. Ciancio SG. Current status of indices of gingivitis. *J Clin Periodontol*. 1986;13(5):375-378. doi:10.1111/j.1600-051X.1986.tb01476.x.

83. Wei SHY, Lang KP. Periodontal epidemiological indices for children and adolescents: I. gingival and periodontal health assessments. *Pediatr Dent*. 1981;3(4):353-360.

84. Syndergaard B, Al-Sabbagh M, Kryscio RJ, et al. Salivary Biomarkers Associated With Gingivitis and Response to Therapy. *J Periodontol*. 2014;85(8):e295-e303. doi:10.1902/jop.2014.130696.Salivary.

85. Barros SP, Williams R, Offenbacher S, Morelli T. Gingival Crevicular as a Source of Biomarkers for Periodontitis. *Periodontology*. 2016;70(1):53-64. doi:10.1111/prd.12107.

86. White SM, Hingorani R, Arora RPS, Hughes CCW, George SC, Choi B. Longitudinal In Vivo Imaging to Assess Blood Flow and Oxygenation in Implantable Engineered Tissues. *Tissue Eng Part C Methods*. 2012;18(9):697-709. doi:10.1089/ten.tec.2011.0744.

87. Farraro R, Fathi O, Choi B. Handheld, point-of-care laser speckle imaging. *J Biomed Opt*. 2016;21(9):94001. doi:10.1117/1.JBO.21.9.094001.

88. Yuan S, Devor A, Boas DA, Dunn AK. Determination of optimal exposure time for imaging of blood flow changes with laser speckle contrast imaging. *Appl Opt*. 2005;44(10):1823-1830. doi:Doi 10.1364/Ao.44.001823.

89. *Laser Safety Handbook*.; 2011. http://www.research.northwestern.edu/ors/forms/laser-safety-handbook.pdf.

90. Jacques SL. Optical Properties of Biological Tissues: A Review. *Phys Med Biol*. 2013;58(11):R37-61. doi:10.1088/0031-9155/58/11/R37.

91. Baab D a, Oberg P a, Holloway G a. Gingival blood flow measured with a laser Doppler flowmeter. *J Periodontal Res*. 1986;21(1):73-85. doi:10.1111/j.1600-0765.1986.tb01440.x.

92. Wilder-Smith P, Hammer-Wilson MJ, Zhang J, et al. In vivo imaging of oral mucositis in an animal model using optical coherence tomography and optical Doppler tomography. *Clin Cancer Res*. 2007;13(8):2449-2454. doi:10.1158/1078-0432.CCR-06-2234.

93. Prahl S, Vitkin I, Bruggemann U, Wilson B, Anderson R. Determination of optical properties of turbid media using pulsed photothermal radiometry. *Phys Med Biol*. 1992;37(6):1203-1217.

94. Kalambur VS, Mahaseth H, Bischof JC, et al. Microvascular blood flow and stasis in transgenic sickle mice: Utility of a dorsal skin fold chamber for intravital microscopy. *Am J*

Hematol. 2004;77(2):117-125. doi:10.1002/ajh.20143.

95. Yang O, Cuccia D, Choi B. Real-time blood flow visualization using the graphics processing unit. *J Biomed Opt*. 2011;16(1):16009. doi:10.1117/1.3528610.

96. Choi B WA. Analysis of thermal relaxation during laser irradiation of tissue. *Lasers Surg Med*. 2001;29(April):351–9.

97. Prahl S. Tabulated Molar Extinction Coefficient for Hemoglobin in Water. http://omlc.ogi.edu/spectra/hemoglobin/summary.html. Published 1998.

98. Hasgall P, Neufeld E, Gosselin M, Klingenbock A, Kuster N. ITIS Database for thermal and electromagnetic parameters of biological tissues. www.itis.ethz.ch/database. Published 2013.

99. Sharif SA, Taydas E, Mazhar A, et al. Noninvasive clinical assessment of port-wine stain birthmarks using current and future optical imaging technology: A review. *Br J Dermatol*. 2012;167(6):1215-1223. doi:10.1111/j.1365-2133.2012.11139.x.

100. Huang YC, Tran N, Shumaker PR, et al. Blood flow dynamics after laser therapy of port wine stain birthmarks. *Lasers Surg Med*. 2009;41(8):563-571. doi:10.1002/lsm.20840.

101. Adler DC, Huang S-W, Huber R, Fujimoto JG. Photothermal detection of gold nanoparticles using phase-sensitive optical coherence tomography. *Opt Express*. 2008;16(7):4376-4393. doi:10.1364/OE.16.004376.

102. Wang X, Pang Y, Ku G, et al. Noninvasive laser-induced photoacoustic tomography for structural and functional in vivo imaging of the brain. *Nat Biotechnol*. 2003;21(7):803-806. doi:10.1038/nbt839.

103. Brilmyer GH, Fujishima A, Santhanam KSV, Bard AJ. Photothermal spectroscopy. *Anal Chem*. 1977;49(13):2057-2062. doi:10.1021/ac50021a042.

104. Sveen JK. *An Introduction to MatPIV v. 1.6.1.*; 2014. http://folk.uio.no/jks/matpiv/.

105. Drezet J-M, Mokadem S. Marangoni convection and fragmentation in Laser treatment. *Mater Sci Forum*. 2006;508(February):257-262. doi:10.4028/www.scientific.net/MSF.508.257.

106. Rosina J, Kvasnák E, Suta D, Kolárová H, Málek J, Krajci L. Temperature dependence of blood surface tension. *Physiol Res*. 2007;56 Suppl 1:S93-8. doi:1306 [pii].

107. Nelson JS, Milner TE, Anvari B, Tanenbaum BS, Svaasand L, Kimel S. Dynamic Epidermal Cooling in Conjunction With Laser-Induced Photothermolysis of Port Wine Stain Blood Vessels. *Lasers Surg Med*. 1996;19:224-229.

108. Tan OT, Sherwood K, Gilchrest BA. Treatment of children with port-wine stains using the flashlamp-pulsed tunable dye laser. *N Engl J Med*. 1989;320(7):416-421. doi:10.1056/NEJM199401273300403.

109. Crouzet C, Nguyen JQ, Ponticorvo A, Bernal NP, Durkin AJ, Choi B. Acute discrimination between superficial-partial and deep-partial thickness burns in a preclinical model with laser speckle imaging. *Burns*. 2015;41(5):1058-1063. doi:10.1016/j.burns.2014.11.018.

110. Davis MA, Gagnon L, Boas DA, Dunn AK. Sensitivity of laser speckle contrast imaging to flow perturbations in the cortex. *Biomed Opt Express*. 2016;7(3):759-775. doi:10.1364/BOE.7.000759.

111. Kazmi SS, Richards LM, Schrandt CJ, Davis MA, Dunn AK. Expanding Applications, Accuracy, and Interpretation of Laser Speckle Contrast Imaging of Cerebral Blood Flow. *J Cereb Blood Flow Metab*. 2015;35(7):1076-1084. doi:10.1038/jcbfm.2015.84.

112. Richards LM, Towle EL, Fox DJ, Dunn AK. Intraoperative laser speckle contrast imaging with retrospective motion correction for quantitative assessment of cerebral blood flow. *Neurophotonics*. 2014;1(1):15006. doi:10.1117/1.NPh.1.1.015006.

113. Kelly KM, Moy WJ, Moy AJ, et al. Talaporfin sodium-mediated photodynamic therapy alone and in combination with pulsed dye laser on cutaneous vasculature. *J Invest Dermatol*. 2015;135(1):302-304. doi:10.1038/jid.2014.304.

114. Mazhar A, Cuccia DJ, Rice TB, et al. Laser speckle imaging in the spatial frequency domain. *Biomed Opt Express*. 2011;2(6):1553-1563. doi:10.1364/BOE.2.001553.

115. Khaksari K, Kirkpatrick SJ. Combined effects of scattering and absorption on laser speckle contrast imaging. *J Biomed Opt*. 2016;21(7):76002. doi:10.1117/1.JBO.21.7.076002.

116. Hajjarian Z, Nadkarni SK. Correction of optical absorption and scattering variations in laser speckle rheology measurements. 2014;22(6):6349-6361. doi:10.1364/OE.22.006349.

117. Hayakawa CK, Spanier J, Venugopalan V. Comparative analysis of discrete and continuous absorption weighting estimators used in Monte Carlo simulations of radiative transport in turbid media. *J Opt Soc Am A Opt Image Sci Vis*. 2014;31(2):301-311.

118. Maret G, Wolf PE. Multiple light scattering from disordered media. The effect of brownian motion of scatterers. *Zeitschrift fur Phys B Condens Matter*. 1987;65(4):409-413. doi:10.1007/BF01303762.

119. Pine DJ, Weitz DA, Chaikin PM, Herbolzheimer E. Diffusing wave spectroscopy. *Phys Rev Lett*. 1988;60(12):1134-1137. doi:10.1103/PhysRevLett.60.1134.

120. Goodman J. *Speckle Phenomena in Optics: Theory and Applications*. Greenwood Village, CO: Roberts and Company; 2007.

121. Bandyopadhyay R, Gittings AS, Suh SS, Dixon PK, Durian DJ. Speckle-visibility spectroscopy: A tool to study time-varying dynamics. *Rev Sci Instrum*. 2005;76(9). doi:10.1063/1.2037987.

122. Davis M a, Kazmi SMS, Dunn AK. Imaging depth and multiple scattering in laser speckle contrast imaging. *J Biomed Opt*. 2014;19(8):86001. doi:10.1117/1.JBO.19.8.086001.

123. Fredriksson I, Larsson M, Strömberg T. Optical microcirculatory skin model: assessed by Monte Carlo simulations paired with in vivo laser Doppler flowmetry. *J Biomed Opt*. 2010;13(1):14015. doi:10.1117/1.2854691.

124. Jacques S. maketissue.m. 2014. omlc.org/software/mc/mcxyz.

125. Fredriksson I, Burdakov O, Larsson M, Strömberg T. Inverse Monte Carlo in a multilayered tissue model : merging diffuse reflectance spectroscopy and laser Doppler flowmetry. *J Biomed Opt*. 2013;18(12):127004. doi:10.1117/1.JBO.18.12.127004.

126. Ponticorvo A, Burmeister DM, Rowland R, et al. Quantitative long-term measurements of burns in a rat model using Spatial Frequency Domain Imaging (SFDI) and Laser Speckle Imaging (LSI). *Lasers Surg Med*. 2017;49(3):293-304. doi:10.1002/lsm.22647.

127. Shams Kazmi SM, Wu RK, Dunn AK. Evaluating multi-exposure speckle imaging estimates of absolute autocorrelation times. *Opt Lett*. 2015;40(15):11-14. doi:10.1364/OL.40.003643.

128. Pusey PN, Van Megen W. Dynamic light scattering by non-ergodic media. *Physica A*. 1989;157:705-741. doi:10.1002/masy.19940790104.

129. Richards LM, Kazmi SS, Olin KE, Waldron JS, Fox DJ, Dunn AK. Intraoperative multi-exposure speckle imaging of cerebral blood flow. *J Cereb Blood Flow Metab*. 2017;0(0):1-13. doi:10.1177/0271678X16686987.

APPENDIX A: Instructions for GUI to create Monte Carlo JSON infiles

Instructions: Create a JSON infile and run a Monte Carlo simulation of light/momentum transport from the command line

Note: This manual was written for the MC_v2.0.2Beta_forMTI_11 software package currently installed on the "amoy" computer in the MTI Lab. Current as of April 20, 2017. It requires the following file:

MTMC_infile_GUI.py: Graphical user interface that takes user input of optical properties and sample geometry and generates a JSON infile used to run the Virtual Photonics MC.2.0.2Beta C# Monte Carlo software.

1. Open a command prompt window (Start menu: type cmd into search bar and hit enter)

2. Use the command prompt to change the directory to the folder containing the software package

```
cd \Users\amoy\Desktop\MC_v2.0.2Beta_forMTI_11
```

3. Use the command prompt to run the Infile Maker GUI in Python

```
python MTMC_infile_GUI.py
```

4. Use the GUI to generate and save an infile with your desired specifications

4.1.a. The "Simulation Name" will be the name of the folder with the results of the simulation in it. (Note: in the MATLAB processing script, this will be the "results_folder" input variable). Do not include spaces in the name

4.1.b. You can choose to set a seed for the random number generator in order to obtain repeatable results or use a random seed.

4.1.c. Number of photons: default is 1,000,000, however this will take multiple hours to run.

4.2.a. Point source: Pencil beam- all photons enter the tissue at the same location and take their first step in the same initial direction. Default: beam centered at (0,0,0) going straight down into the tissue.
Note: The center of the virtual tissue coordinate axis is (0,0,0) with the positive Z-direction going into the tissue. Coordiante system has units of millimeters.

4.2.b. Circular source: Circular light source centered at (0,0,0) with radius specified by user (millimeters). The source may be either uniform or Gaussian. If using a Gaussian beam profile, the full width half max must be listed (millimeters).

4.2.c. Rectangular source: Rectangular light source centered at (0,0,0) with total length and width specified by user (millimeters). (ie: if Width = 10 source will go from -5mm to 5mm in X-direction).

4.2.d. Source Notes: I typically use a rectangular source when working in rectangular coordinates, and a circular source when working in cylindrical coordinates in order average my results over the maximum possible area while avoiding the edges of the illuminated region.

4.3.a. Optical properties of the inclusion must be given in units of mm^{-1}. Blood volume fraction specifies the fraction of scattering events that are dynamic (ie: to mimic a completely dynamic material such as pure blood, use BVF of 1. To mimic a completely static material such as PDMS use a BVF of 0). Note: the index of refraction (N) of the inclusion must be the same as the surrounding layer. Also, an inclusion must be entirely contained within a single layer. The anisotropy (g) must be a number between (0,1), not including 0 or 1.

4.3.b. Ellipsoidal inclusion: This is typically used to create a "vessel" by extending the ellipsoid semi-infinitely in the Y-direction (ie: center at (0,0,0.3) with radii of (0.2, 50, 0.2) to create a 0.4mm diameter vessel buried 0.1mm below the surface).

4.3.c. Rectangular inclusion: This is typically used to create a "vessel" with edges that can line up precisely with the edges of the detector bins.

4.4.a. Number of tissue layers: Number of layers in a given virtual tissue. Note: the current method to compute speckle contrast allows the user to specify up to two flow types. For example: Static vs dynamic: there can be infinitely many layers with different optical properties and blood volume fractions; however, all dynamic events must have the same flow speed. Alternatively, you could also have two dynamic regions, one with flow speed 1 and one with flow speed 2 (the percentage of scatterers with flow speed 2 would be equal to the blood volume fraction).

4.4.b. Enter the start/end depths (millimeters) of each layer. Default is that the 1^{st} layer starts at Z=0. Enter the optical properties (absorption, reduced scattering, anisotropy, and index of refraction) of each layer. Remember, if a layer contains an inclusion it must have the same index of refraction as the inclusion.

4.5.a. Choose a coordinate system (XY or Rho). Note that if cylindrical coordinates are chosen the virtual tissue must have cylindrical symmetry about the z-axis (ie: cannot have a vessel-like inclusion).

4.5.b. Choose which detectors you want. Note: the simulation will throw an "out of memory" error if too many detectors or too many bins are specified. The exact amount is specific to the computer's memory.

4.5.c. Choose the X, Y, and Z range (millimeters) for each detector (note: the source is typically centered at (0,0,0), so choosing a range centered at 0 such as -10.0 to 10.0 in X&Y is a good way to view the entire tissue depending on how large the source was. The tissue typically starts at Z=0 and has air above and below, so choosing a Z range of 0 to the thickness of the tissue is typical.)

4.5.d. Number of Bins: This is the resolution of the detector; the more bins, the more finely the results will be incremented. More bins will provide a finer spatial resolution, however, it will also result in noisier data. For example, if you are recording fluence from -10.0 to 10.0, and you create 40 bins, each bin will be 0.5mm wide.

4.5.e. MT Bins: default is 500 bins with a spacing of 1. Do not change this unless you have good reason.

4.5.f. Fractional MT Bins: Default is 10 bins. If you are using very low blood volume fractions (ie: <5-10%) then increase the # of Bins to 50. For larger blood volume fractions (ie: completely dynamic scattering) 10 bins is sufficient.

4.5.g. Blood volume fraction: fraction of scattering events in each layer that are dynamic (or correspond to "flow speed 2").

4.6.a. Directory: where the infile is saved. The default is which ever directory you are currently in. The infile must be saved in the same directory as the Virtual Photonics Software.

4.6.b. Infile name: must start with "infile_" and should not contain spaces.

5. Run the simulation with the infile you just created.

```
mc infile=infile_FILENAME.txt
```

6. If there is an "out of memory" error, then you likely have tried to create too many bins. This is especially common if you have several tissue layers.

7. The command line will update with a time stamp and the amount of progress. When the simulation is complete, a folder with the results will be saved in your directory.

APPENDIX B: Calculation of simulated speckle contrast

This appendix contains the following m-files.

processMTMCresults.m: script to compute simulated speckle contrast using output from a Monte Carlo simulation. This script requires: compute_K_XY.m, compute_K_Rho.m, load_results_script.m (modified from Virtual Photonics MCv2.0.2Beta), loadMCResults.m (from Virtual Photonics MCv2.0.2Beta), readBinaryData.m (from Virtual Photonics MCv2.0.2Beta) and jsonlab (from Virtual Photonics MCv2.0.2Beta).

compute_K_XY.m: function to compute simulated speckle contrast in rectangular coordinates. This function is called by the processMTMCresults.m script.

compute_K_Rho.m: function to compute simulated speckle contrast in cylindrical coordinates. This function is called by the processMTMCresults.m script.

Instructions: Visualize light transport and calculate contrast using MATLAB

Note: For basic outputs (maps of Fluence/Reflectance/Transmittance/Absorption/MT) and calculation of speckle contrast at a particular speed and exposure time, the "processMTMCresults.m" script will be sufficient. For more detailed analysis, one of the variables created in this script is a structure (MTMC_output) that contains the values of fluence and momentum transfer values at each coordinate. These values are obtained from the "load_results_script.m" provided by Virtual Photonics, which I have converted to a function. To access more detailed results, you will need to modify this script directly.

1. Open MATLAB script "processMTMCresults.m" (note: all m-files must be in the same directory as the results folder output by the MTMC simulation. Therefore, you will need to copy your results folder into the Matlab Processing Scripts folder.)

2. Make any necessary changes in "Input Variables" section and run the script. The output will have a plot of the probability distribution of the total momentum transfer, as well as the probability distribution of the fraction of light that was in flow region 2 (dynamically scattered). The script will also output a speckle contrast value (assuming beta is 1).

2.a. results_folder: This is the name of the folder containing the results from the MTMC simulation. Must be a string.

2.b. wavelength: This is the wavelength of light used to calculate speckle contrast (nanometers)

2.c. exposure_time: This is the exposure time used to calculate speckle contrast (milliseconds)

2.d. motion_type1: This is the type of motion (either Brownian motion ('B') or directed flow ('D')) in flow region 1.

2.e. speed1: This is the speed of scatterers in flow region 1. If your two regions are "static" and "dynamic," region 1 is the static scatterers, therefore they should be assigned a speed of zero.

2.f. motion_type2: This is the type of motion (either Brownian motion ('B') or directed flow ('D')) in flow region 2.

2.g. speed2: If your two regions are “static” and “dynamic,” region 2 is the dynamic scatterers. If you specified Brownian motion, speed should be given as the Brownian diffusion coefficient (with units of mm^2/s). If you specified directed flow, speed should be given in mm/s.
2.h. transmitted/reflected: These values should be set to either “true” or “false” depending on whether you chose a virtual detector to track reflected or transmitted momentum transfer.
2.i. XY_coordinates/Rho_coordinates: These values should be set to either “true” or “false” depending on whether the momentum transfer detectors were binning in rectangular or cylindrical coordinates.
2.j. X_Start/X_Stop/Y_Start/Y_Stop/Rho_Start/Rho_Stop: I typically sum the momentum transfer results over a certain region of my virtual tissue in order to improve the signal to noise. If my virtual tissue is homogeneous (ie: no inclusion or spatial features), I typically sum over the entire area excluding the 1^{st} and last momentum transfer bin (all virtual photons from areas beyond the virtually detector area get put in the 1^{st} and last bins). If my source is smaller than the area I record my detector results over, then I typically avoid bins near the edge of my source to avoid edge effects. If you forgot how many bins were in your detector, or want to know what X&Y values (in mm) they correspond to, this data is available in the MTMC_output structure (ie: MTMC_output.MTr_XY_XBins contains all reflected momentum transfer X bins).

3. Fields in the MTMC_output structure:

3.1.a. F_Rho: fluence as a function of rho and Z in cylindrical coordinates
3.1.b. F_Rho_RhoBins: Rho bins used to store fluence values (F_Rho) in cylindrical coordinates
3.1.c. F_Rho_ZBins: Z bins used to store flunece values (F_Rho) in cylindrical coordinates

3.2.a. F_XY: fluence as a function of X,Y and Z in rectangular coordinates
3.2.b. F_XY_XBins: X bins used to store fluence values (F_XY) in rectangular coordinates
3.2.c. F_XY_YBins: Y bins used to store fluence values (F_XY) in rectangular coordinates
3.2.d. F_XY_ZBins: Z bins used to store flunece values (F_XY) in rectangular coordinates

3.3.a. MTr_Rho: Reflected momentum transfer as a function of rho and Z in cylindrical coordinates
3.3.b. MTr_Rho_RhoBins: Rho bins used to store reflected momentum transfer values (MTr_Rho) in cylindrical coordinates
3.3.c. MTr_Rho_MTBins: Momentum transfer bins used to store reflected momentum transfer values (MTr_Rho) in cylindrical coordinates
3.3.d. MTr_Rho_Z: Weighted reflected momentum transfer as a function of Z in cylindrical coordinates

3.3.e. MTr_Rho_ZBins: Z bins used to store weighted reflected momentum transfer values (MTr_Rho_Z) in cylindrical coordinates

3.4.a. MTr_XY: Reflected momentum transfer as a function of X,Y and Z in rectangular coordinates
3.4.b. MTr_XY_XBins: X bins used to store reflected momentum transfer values (MTr_XY) in rectangular coordinates
3.4.c. MTr_XY_YBins: Y bins used to store reflected momentum transfer values (MTr_XY) in rectangular coordinates
3.4.d. MTr_XY_MTBins: Momentum transfer bins used to store reflected momentum transfer values (MTr_XY) in rectangular coordinates
3.3.e. MTr_XY_Z: Weighted reflected momentum transfer as a function of Z in rectangular coordinates
3.3.f. MTr_XY_ZBins: Z bins used to store weighted reflected momentum transfer values (MTr_XY_Z) in rectangular coordinates

3.5.a. MTt_Rho: Transmitted momentum transfer as a function of rho and Z in cylindrical coordinates
3.5.b. MTt_Rho_RhoBins: Rho bins used to store transmitted momentum transfer values (MTt_Rho) in cylindrical coordinates
3.5.c. MTt_Rho_MTBins: Momentum transfer bins used to store transmitted momentum transfer values (MTt_Rho) in cylindrical coordinates
3.5.d. MTt_Rho_Z: Weighted transmitted momentum transfer as a function of Z in cylindrical coordinates
3.5.e. MTt_Rho_ZBins: Z bins used to store weighted transmitted momentum transfer values (MTt_Rho_Z) in cylindrical coordinates

3.6.a. MTt_XY: Transmitted momentum transfer as a function of X,Y and Z in rectangular coordinates
3.6.b. MTt_XY_XBins: X bins used to store transmitted momentum transfer values (MTt_XY) in rectangular coordinates
3.6.c. MTt_XY_YBins: Y bins used to store transmitted momentum transfer values (MTt_XY) in rectangular coordinates
3.6.d. MTt_XY_MTBins: Momentum transfer bins used to store transmitted momentum transfer values (MTt_XY) in rectangular coordinates
3.6.e. MTt_XY_Z: Weighted transmitted momentum transfer as a function of Z in rectangular coordinates
3.6.f. MTt_XY_ZBins: Z bins used to store weighted transmitted momentum transfer values (MTt_XY_Z) in rectangular coordinates

processMTMCresults.m

```
%% Script to process MTMC Simulations
% by Caitlin Regan: last edit 4-19-2017

clear all; close all;

%% Input Variables
results_folder = 'Experiment_FileName'; % The folder with your results must
      % be in the same folder as the processing m-files
wavelength = 808; % Wavelength of light (nanometers)
exposure_time = 10; % Exposure time (milliseconds)
motion_type1 = 'D'; % type of motion in region 1: 'B' for Brownian motion,
      % 'D' for directed flow
speed1 = 0; % Typically region 1 is the "static" region and should be
      % assigned speed of 0. Brownian diffusion constant (in mm^2/s) or speed
      % of directed flow (in mm/s)
motion_type2 = 'D'; % type of motion in region 2: 'B' for Brownian motion,
      % 'D' for directed flow
speed2 = 0.36; % Typically region 2 is the "dynamic" region and should be
      % assigned a speed corresponding to the speed of dynamic scatterers.
      % Brownian diffusion constant (in mm^2/s) or speed of directed flow (in
      % mm/s)

transmitted = true; % Change this to true if quantifying transmitted speckle
      % contrast
reflected = true; % Change this to true if quantifying reflected speckle
      % contrast

XY_coordinates = true; % Change this to true if using rectangular coordinates
X_Start = 2; % Bin number for x-range to start
X_Stop = 99; % Bin number for x-range to end
Y_Start = 2; % Bin number for y-range to start
Y_Stop = 99; % Bin number for y-range to end

Rho_coordinates = false; % Change this to true if using cylidrical
      % coordinates
Rho_Start = 1; % Bin number for rho-range to start
Rho_Stop = 10; % Bin number for rho-range to end

%% Process light transport simulations

MTMC_output = load_results_script(results_folder);
      % Note: the MTMC_output structure contains many useful outputs from the
      % light transport simulations. Fields are listed in instructions
      % manual.

%% Compute speckle contrast

if XY_coordinates == true
    if reflected == true
        K_XY_reflected = compute_K_XY(MTMC_output.MTr_XY,
            MTMC_output.MTr_XY_MTBins, X_Start, X_Stop, Y_Start, Y_Stop,
            wavelength*(10^-6), exposure_time / 1000, motion_type1, speed1,
            motion_type2, speed2)
    end

    if transmitted == true
        K_XY_transmitted = compute_K_XY(MTMC_output.MTt_XY,
```

```
            MTMC_output.MTt_XY_MTBins, X_Start, X_Stop, Y_Start, Y_Stop,
            wavelength*(10^-6), exposure_time / 1000, motion_type1, speed1,
            motion_type2, speed2)
    end
end

if Rho_coordinates == true
    if reflected == true
        K_Rho_reflected = compute_K_Rho(MTMC_output.MTr_Rho,
            MTMC_output.MTr_Rho_MTBins, Rho_Start, Rho_Stop, wavelength*(10^-
            6), exposure_time / 1000, motion_type1, speed1, motion_type2,
            speed2)
    end

    if transmitted == true
        K_Rho_transmitted = compute_K_Rho(MTMC_output.MTt_Rho,
            MTMC_output.MTt_Rho_MTBins, Rho_Start, Rho_Stop, wavelength*(10^-
            6), exposure_time / 1000, motion_type1, speed1, motion_type2,
            speed2)
    end
end
```

compute_K_XY.m

```
%% Function to compute contrast in rectangular coordinates
% by Caitlin Regan: last edit 4-19-2017

function K_XY = compute_K_XY(MT, MTbins, Xstart, Xstop, Ystart, Ystop,
      wavelength, exposure_time, type1, speed1, type2, speed2)

    Xrange = Xstart:Xstop; % Range of X bins to sum over
    Yrange = Ystart:Ystop; % Range of Y bins to sum over

    %% Reflected Initial Probability Distributions for Dynamic MT Detector

    %%Use for summed results over a range of X&Y bins

    MT_bins_midpoints_RD = MTbins; % Midpoints of X&Y bins
    MT_matrix_original_RD = MT; % Main dynamic momentum transfer results
            % matrix [fraction of dynamic MT, total MT, Y bins, X bins]
    MT_matrix_summedY_RD = sum(MT_matrix_original_RD(:,:,Yrange,Xrange),3);
            % Sum over Y bins
    MT_matrix_summedX_RD = sum(MT_matrix_summedY_RD,4); % Sum over X bins
    MT_matrix_RD = squeeze(MT_matrix_summedX_RD); % Condense results matrix
            % [fraction of dynamic MT, total MT]
    sum_totalMT_bins_RD = sum(MT_matrix_RD); %Sum the fractional dynamic MT
            % bins (columns) to get total MT
    sum_totalMT_RD = sum(sum_totalMT_bins_RD(:)); %Total MT in the system
    totalMT_norm_RD = sum_totalMT_bins_RD / sum_totalMT_RD; %Normalize the
            % photon weights
    figure(); bar(MT_bins_midpoints_RD, totalMT_norm_RD); xlabel('Reflected
            % MT','FontSize',14,'FontWeight','Bold'); ylabel('Normalized
            % Photon Weight','FontSize',14,'FontWeight','Bold');
    title('P(Y)','FontSize',14,'FontWeight','Bold');
    set(gca,'FontSize',14,'FontWeight','Bold'); % Plot of histogram of total
            % momentum transfer
    sum_fracMT_bins_RD = sum(MT_matrix_RD, 2); %Sum MT in each fractional bin
            % (rows) to get fraction of dynamic MT
    fracMT_norm_RD = sum_fracMT_bins_RD / sum_totalMT_RD; %Normalize the
            % fractional photon weights

    % Note that current version of code assumes same # of fractional MT bins
    % in all outputs
    numfracs=size(fracMT_norm_RD,1); % Number of fractional MT bins
    ar{1}='0';ar{numfracs}='1';
    y_space = 1/(length(fracMT_norm_RD)-2); % Spacing of fractional MT bins
    y = y_space/2:y_space:1-y_space/2; % Midpoints of fractional MT bins
    y = [0 y]; % Set 1st and last fractional MT bin to 0 & 1 respectively
    y(end+1) = 1;
    for k=0:numfracs-1
        ar{k+1}=sprintf('%3.2f',y(k+1));
    end
    figure(); bar(1:length(fracMT_norm_RD),fracMT_norm_RD); xlabel('Fraction
            of Reflected Dynamic MT','FontSize',14,'FontWeight','Bold');
            ylabel('Normalized Photon
            Weight','FontSize',14,'FontWeight','Bold');
    title('P(y)','FontSize',14,'FontWeight','Bold');
    set(gca,'XTick',1:numfracs);
    set(gca,'XTickLabel',ar(1:numfracs),'FontSize',14,'FontWeight','Bold')

    %% Autocorrelation G1(tau) for Reflected Dynamic MT
```

```
P_Y_RD = totalMT_norm_RD(1:end-1); % Probability distribution of Y
P_y_RD = fracMT_norm_RD; % Probability distribution of fraction of Y that
        % is dynamic
Y_RD = MT_bins_midpoints_RD(1:end-1); % Momentum transfer

%% Initialize Constants for Integration
y_space = 1/(length(fracMT_norm_RD)-2); % Spacing of fractional MT bins
y = y_space/2:y_space:1-y_space/2; % Midpoints of fractional MT bins
y = [0 y]; % Set 1st and last fractional MT bin to 0 & 1 respectively
y(end+1) = 1;
lambda = wavelength; % Wavelength of light (mm)
k0 = 2 * pi * 1.4 / lambda; % Wavenumber (1.4 is index of refraction of
        % tissue)
T = exposure_time; % Exposure time in seconds
tau = logspace(log10(T/1000),log10(T),150); % Bins for tau integraton
tau = [0 tau]; % First value in tau vector must be zero in order to
        % normalize g1 later

%% Motion for Each Layer
%V1t and V2t depend on whether motion is Brownian or Directed

if type1 == 'B'
    % Brownian
    Db1 = speed1; % Diffusion constant for non-moving regions
    c1 = 6 * Db1;
    n1 = 1;
elseif type1 == 'D'
    % Directed
    v1 = speed1; % Speed in layer 1 (mm/s) [Static scatterers]
    c1 = (v1)^2;
    n1 = 2;
end

if type2 == 'B'
    % Brownian
    Db2 = speed2; % Diffusion constant
    c2 = 6 * Db2;
    n2 = 1;
elseif type2 == 'D'
    % Directed
    v2 = speed2; % Speed in layer 2 (mm/s) [Dynamic scatterers]
    c2 = (v2)^2;
    n2 = 2;
end


%% Calculate Contrast
[TAUm, Y_ym] = meshgrid(tau,y); % Matrix to integrate over fraction of
        % dynamic MT (y) and tau
Y_matrix_RD(1,1,:) = Y_RD; % Matrix of total momentum transfer (Y)
Y_matrix_RD = repmat(Y_matrix_RD,[length(y), length(tau), 1]);
P_Y_matrix_RD(1,1,:) = P_Y_RD; % Matrix of photon weights at each
        % momentum transfer (P(Y))
P_Y_matrix_RD = repmat(P_Y_matrix_RD,[length(y), length(tau), 1]);
P_y_matrix_RD = repmat(P_y_RD,[1, length(tau), length(Y_RD)]); % Matrix
        % of fraction of dynamic MT (P(y))

G1_RD = -1 * k0^2 * (c2 * TAUm.^n2 .* Y_ym + c1 * TAUm.^n1 .* (1-Y_ym)) /
```

```
            3; % Contents of exponent in field autocorrelation calculation
        G1b_RD = repmat(G1_RD, [1,1,length(Y_RD)]);
        G1c_RD = P_Y_matrix_RD .* P_y_matrix_RD .* exp(Y_matrix_RD .* G1b_RD);
            % Matrix of field autocorrelation integral
        G1_tau_RD = trapz(y,G1c_RD); % Integrating over dy to compute field
            % autocorrelation function (G1)
        int_G1_tau_RD = trapz(Y_RD,G1_tau_RD,3); % 2nd Integral (over dY) of
            % field autocorrelation function (G1)
        g1_RD = (1 - tau / T) .* ((abs(int_G1_tau_RD / int_G1_tau_RD(1))).^2);
            % Integral over exposure time to compute normalized field
            % autocorrelation function
        int_g1_RD = trapz(tau, g1_RD); % Integrating over exposure times to
            % compute normalized field autocorrelation function

        K_sq_RD = 2 * int_g1_RD / T; % Contrast squared assumming Beta is 1,
            % actually K^2 = 2 * Beta^2 * int_g1 / T
        K_XY = sqrt(K_sq_RD); % Output contrast value

end
```

compute_K_Rho.m

```
%% Function to compute contrast in cylindrical coordinates
% by Caitlin Regan: last edit 4-19-2017

function K_rho = compute_K_rho(MT, MTbins, RhoStart, RhoStop, wavelength,
      exposure_time, type, speed)

    RhoRange = RhoStart:RhoStop; % Range of rho bins to sum over

    %% Reflected Initial Probability Distributions with Cylindrical Geometry
            % for Dynamic MT Detector
    MT_bins_midpoints_Rho_RD = MTbins;
    MT_matrix_original_Rho_RD = MT;
    MT_matrix_summedRho_RD = sum(MT_matrix_original_Rho_RD(:,:,RhoRange),3);
            % [NumFracMTBins, NumMTBins, NumRhos]
    MT_matrix_Rho_RD = squeeze(MT_matrix_summedRho_RD);
    sum_totalMT_bins_Rho_RD = sum(MT_matrix_Rho_RD); %Sum the fractional MT
            % bins (columns) to get total MT
    sum_totalMT_Rho_RD = sum(sum_totalMT_bins_Rho_RD(:)); %Total MT in the
            % system
    totalMT_norm_Rho_RD = sum_totalMT_bins_Rho_RD / sum_totalMT_Rho_RD;
            % Normalize the photon weight
    figure(); bar(MT_bins_midpoints_Rho_RD, totalMT_norm_Rho_RD);
    xlabel('Reflected MT'); ylabel('Normalized Photon Weight');
    title('P(Y,Rho)');
    set(gca,'FontSize',14,'FontWeight','Bold'); % Plot of histogram of total
            % momentum transfer
    sum_fracMT_bins_Rho_RD = sum(MT_matrix_Rho_RD, 2); %Sum MT in each
            % fractional bin (rows) to get fractional MT
    fracMT_norm_Rho_RD = sum_fracMT_bins_Rho_RD / sum_totalMT_Rho_RD;
            % Normalize the photon weight

    % Note that current version of code assumes same # of fractional MT bins
            % in all outputs
    numfracs=size(fracMT_norm_Rho_RD,1); % Number of fractional MT bins
    ar{1}='0';ar{numfracs}='1';
    y_space = 1/(length(fracMT_norm_Rho_RD)-2); % Spacing of fractional MT
            % bins
    y = y_space/2:y_space:1-y_space/2; % Midpoints of fractional MT bins
    y = [0 y]; % Set 1st and last fractional MT bin to 0 & 1 respectively
    y(end+1) = 1;
    for k=0:numfracs-1
        ar{k+1}=sprintf('%3.2f',y(k+1));
    end
    figure(); bar(1:length(fracMT_norm_Rho_RD),fracMT_norm_Rho_RD);
    xlabel('Fraction of Reflected Dynamic MT');
    ylabel('Normalized Photon Weight');
    title('P(y,Rho)');
    set(gca,'XTick',1:numfracs); set(gca,'XTickLabel',ar(1:numfracs))

    %% Autocorrelation G1(tau) for Reflected Dynamic MT in Cylindrical
            % Coordinates
    P_Y_Rho_RD = totalMT_norm_Rho_RD(1:end-1);
            % Probability distribution of Y
    P_y_Rho_RD = fracMT_norm_Rho_RD; % Probability distribution of fraction
            % of Y in 1st layer
    Y_Rho_RD = MT_bins_midpoints_Rho_RD(1:end-1); % Momentum transfer
```

```
%% Initialize Constants for Integration
y_space = 1/(length(fracMT_norm_Rho_RD)-2);
        % Spacing of fractional MT bins
y = y_space/2:y_space:1-y_space/2; % Midpoints of fractional MT bins
y = [0 y]; % Set 1st and last fractional MT bin to 0 & 1 respectively
y(end+1) = 1;
lambda = wavelength; % Wavelength of light (mm)
k0 = 2 * pi * 1.4 / lambda; % Wavenumber (1.4 is index of refraction of
        % tissue)
T = exposure_time; % Exposure time in seconds
tau = logspace(log10(T/1000),log10(T),150); % Bins for tau integraton
tau = [0 tau]; % First value in tau vector must be zero in order to
        % normalize g1 later

%% Motion for Each Layer
%V1t and V2t depend on whether motion is Brownian or Directed

if type1 == 'B'
    % Brownian
    Db1 = speed1; % Diffusion constant for non-moving regions
    c1 = 6 * Db1;
    n1 = 1;
elseif type1 == 'D'
    % Directed
    v1 = speed1; % Speed in layer 1 (mm/s) [Static scatterers]
    c1 = (v1)^2;
    n1 = 2;
end

if type2 == 'B'
    % Brownian
    Db2 = speed2; % Diffusion constant
    c2 = 6 * Db2;
    n2 = 1;
elseif type2 == 'D'
    % Directed
    v2 = speed2; % Speed in layer 2 (mm/s) [Dynamic scatterers]
    c2 = (v2)^2;
    n2 = 2;
end

%% Reflected G1(tau) in Cylindrical Coordinate for Dynamic MT Detector

[TAUm, Y_ym] = meshgrid(tau,y);
Y_matrix_Rho_RD(1,1,:) = Y_Rho_RD;
Y_matrix_Rho_RD = repmat(Y_matrix_Rho_RD,[length(y), length(tau), 1]);
P_Y_matrix_Rho_RD(1,1,:) = P_Y_Rho_RD;
P_Y_matrix_Rho_RD = repmat(P_Y_matrix_Rho_RD,[length(y), length(tau),
        1]);
P_y_matrix_Rho_RD = repmat(P_y_Rho_RD,[1, length(tau),
        length(Y_Rho_RD)]);

G1_Rho_RD = -1 * k0^2 * (c2 * TAUm.^n2 .* Y_ym + c1 * TAUm.^n1 .*
        (1-Y_ym)) / 3;
G1b_Rho_RD = repmat(G1_Rho_RD, [1,1,length(Y_Rho_RD)]);
G1c_Rho_RD = P_Y_matrix_Rho_RD .* P_y_matrix_Rho_RD .*
        exp(Y_matrix_Rho_RD .* G1b_Rho_RD);
G1_tau_Rho_RD = trapz(y,G1c_Rho_RD);
```

```
    int_G1_tau_Rho_RD = trapz(Y_Rho_RD,G1_tau_Rho_RD,3);
    g1_Rho_RD = (1 - tau / T) .* ((abs(int_G1_tau_Rho_RD /
            int_G1_tau_Rho_RD(1))).^2);
    int_g1_Rho_RD = trapz(tau, g1_Rho_RD);

    K_sq_Rho_RD = 2 * int_g1_Rho_RD / T; % Contrast squared assumming Beta is
            % 1, actually K^2 = 2 * Beta^2 * int_g1 / T
    K_rho = sqrt(K_sq_Rho_RD); % Output contrast value
end
```